A Tour Through Astrophysical Fluid Dynamics

Peter Goldreich

November 10, 2009

Contents

1 Evolution of Gravitationally Bound Bodies 20
1.1 Classification Of Gravitationally Bound Systems 20
1.2 Systems Supported By Thermal Pressure 21
1.2.1 three examples 21
1.3 Systems Supported By Rotation 22
1.3.1 three examples 26
1.4 Systems Supported By Degeneracy Pressure 28

2 Stars 33
2.1 Structure 33
2.1.1 3 well-separated time scales 33
2.1.2 hydrostatics 34
2.1.3 energy transport 35
2.1.4 nuclear fusion 36
2.2 Evolution 36
2.2.1 contraction onto main sequence 36
2.2.2 main sequence 37
2.2.3 post-main sequence evolution 38
2.3 Remants 41

2.3.1 White Dwarfs 41
2.3.2 Neutron Stars 42
2.3.3 Black Holes 44
2.4 Remnants Revealed 44
2.4.1 White Dwarfs 44
2.4.2 Neutron Stars 46
2.4.3 Black Holes 47
2.5 Fluid Phenomena 47
2.5.1 Oscillation Modes of Non-Rotating Stars 47
2.5.2 Stellar Winds 61
2.5.3 Supernova Remnants 70

3 Disks **76**
3.1 Why Disks? 76
3.2 Mechanisms of Angular Momentum Transport 77
3.2.1 Collisional Stresses 77
3.2.2 Turbulent And Magnetic Stresses 77
3.2.3 Spiral Density Waves 80
3.2.4 Tides 89

4 Magnetic Fields **97**
4.1 Dynamos 97
4.1.1 Observational Evidence from Solar System Bodies 97
4.1.2 General Principles 99
4.1.3 Evidence for Dynamos 101
4.1.4 Solar Dynamo 103
4.1.5 Record Of Past Solar Activity 106
4.2 Magnetospheres 110
4.2.1 Definitions 110
4.2.2 Size Of Magnetosphere 111

4.2.3 Particle Motion . . . 112
4.2.4 Jovian Magnetosphere . . . 114
4.3 Force Free Electrodynamics . . . 114
4.3.1 Description . . . 114
4.3.2 Equations . . . 116
4.3.3 Applications . . . 117
4.4 Cosmic Batteries . . . 117
4.4.1 need for batteries . . . 117
4.4.2 equations . . . 121
4.4.3 Biermann Battery . . . 122

5 Odds and Ends **124**
5.1 Growth of Structure: Newtonian Perturbation Theory . . . 124
5.2 Hydrodynamic Turbulence . . . 125
5.2.1 Strong Turbulence . . . 125
5.2.2 Weak Turbulence . . . 129
5.3 Magnetohydrodynamical Turbulence . . . 139
5.3.1 motivation from radio observations of pulsars . . . 139
5.3.2 HD Turbulence . . . 139
5.3.3 MHD Equations . . . 140
5.3.4 Wave Packets . . . 141
5.3.5 Weak MHD Turbulence . . . 142
5.3.6 Strong MHD Turbulence . . . 145
5.3.7 Common Features of Cascades . . . 146
5.3.8 Imbalanced Cascades . . . 146
5.4 Interaction of Sound Waves with Turbulence . . . 148
5.4.1 Setup . . . 148
5.4.2 Emissivity . . . 149
5.4.3 Absorptivity . . . 150
5.4.4 Energy of Acoustic Modes . . . 150

5.4.5 Time to Achieve Equilibrium 151

List of Figures

1.1 Our Sun with numerous large spots from 2003. Credit: SOHO (ESA & NASA) 23
1.2 M80 (NGC 6093) is one of the densest of the 147 known globular star clusters in the Milky Way galaxy. Located about 9 kpc, M80 contains hundreds of thousands of stars bound by their mutual gravitational attraction. All the stars in the cluster have the same age (about 15 billion years), but cover a range of stellar masses. Every star visible in this image is either more highly evolved than, or in a few rare cases more massive than, our own Sun. Especially obvious are the bright red giants that are nearing the ends of their lives. Credit: The Hubble Heritage Team (AURA/ STScI/ NASA) 24
1.3 M87 is the dominant galaxy at the center of the neighboring Virgo cluster of galaxies, which contains some 2,000 galaxies. Amid the smooth, yellow population of older stars, the two features that stand out, the soft blue jet and the myriad of starlike globular clusters. Credit: NASA, ESA, and the Hubble Heritage Team (STScI/AURA) 25
1.4 Earth-Moon system as seen from Mars: credit NASA 27
1.5 This image is an artist's conception of a black hole inside an accretion disk feeding a black hole and giving rise to a spin-aligned jet. credit: ESA 29
1.6 The Sombrero galaxy exhibits a brilliant white, bulbous core encircled by the thick dust lanes comprising its spiral structure. We view it from just six degrees north of its equatorial plane. The Sombrero is one of the most massive objects in Virgo cluster which is at about a distance of 9 Mpc. Credit: NASA and The Hubble Heritage Team (STScI/AURA) 30

1.7 Frosty white water ice clouds and swirling orange dust storms above a vivid rusty landscape reveal Mars as a dynamic planet in this sharpest view ever obtained by an Earth-based telescope. The colors have been carefully balanced to give a realistic view of Mars' hues as they might appear through a telescope.Credit: NASA and the Hubble Heritage Team (STScI/AURA) Acknowledgment: J. Bell (Cornell U.) 31

1.8 A composite made from ultraviolet- and visible-light images of Jupiter. The glowing aurorae near Jupiters North and South Poles were imaged in the UV and the cloudtops are seen through blue and red filters . Aurorae are produced when energetic charged particles precipitate near the planet's magnetic poles and cause hydrogen to fluoresce high in Jupiter's atmosphere. Credit: NASA, ESA, and the Hubble Heritage Team (STScI/AURA) Acknowledgment: H. Weaver (JHU/APL) and A. Simon-Miller (NASA/GSFC) 32

2.1 Hertzsprung-Russell diagram by Richard Powell with permission. 22,000 stars are plotted from the Hipparcos catalog and 1,000 from the Gliese catalog of nearby stars. An examination of the diagram shows that stars tend to fall only into certain regions on the diagram. The most predominant is the diagonal, going from the upper-left (hot and bright) to the lower-right (cooler and less bright), called the Main Sequence. In the lower-left is where white dwarfs are found, and above the main sequence are the subgiants, giants and supergiants. The Sun is found on the main sequence at luminosity 1 (absolute magnitude 4.8) and B-V color index 0.66 (temperature 5780K, spectral type G2). 39

2.2 White Dwarfs are remnant cores of stars with $M < 8M_\odot$. They are supported against gravity by electron degeneracy pressure. Stars with $M < 4M_\odot$ yield C-O white dwarfs & Stars with $4M_\odot < M < 8M_\odot$ yield O-Ne-Mg white dwarfs. Credit: Richard Pogge 43

2.3 Neutron Stars are remnant cores of stars with $M > 12M_\odot$. They are supported against gravity by neutron degeneracy pressure and the strong repulsive force. Credit: Richard Pogge 45

2.4 Pulsars are rapidly spinning, magnetized neutron stars. Spinning magnetic field generates a strong electric field which accelerates electrons and positrons along field lines that pass through the light cylinder. Credit: Richard Pogge 48

2.5 credit I. P. Lopes (2001) 51

2.6 credit I. P. Lopes (2001) 52

2.7 A computer-generated image showing the pattern of a p-mode solar acoustic oscillation both in the interior and on the surface of the sun. (l=20, m=16 and n=14.) Note that the increase in the speed of sound as waves approach the center of the sun causes a corresponding increase in the acoustic wavelength. 54
2.8 MDI Single Dopplergram Minus 45 Image Average Subtracting an average solar velocity image observed over 45 minutes from a single velocity image reveals the surface motions associated with sound waves traveling through the Sun's interior. The smallscale light and dark regions represent the up and down motions of the hot gas near the Sun's surface. The pattern falls off towards the limb because the acoustic waves are primarily radial. 57
2.9 l-nu diagram from MDI high-cadence full disk data. Shows mode frequencies up to 10 milliHz and l=1000. 58
2.10 The broken line represents the route of the centre of mass of the child. When the boy swings to point A, he rises his body. Assuming that he rises his centre of mass by a distance d and the tension of the rope is T_A, he does positive work dT_A. When the boy swings to point B, he lowers his centre of mass and negative work dT_B. When the boy is at point B, his velocity is zero, so T_B is just the vertical component of his weight. But when he is at point A, his velocity is the greatest, T_B is the sum of his weight and the centripetal force. Hence energy is fed to the swing. Source: Prof. Lai Hon-ming. Translation by Sammy Tsui in Physics World 62
2.11 isothermal solar wind 64
2.12 Two tails of comet Hale-Bopp. The blue tail of ionized gas interacts with the solar wind and points radially away from the Sun. The dust in the yellowish tail moves under the combined effects of gravity and radiation pressure. CO^+ is the source of the blue light. When it was the same distance from the Sun as Earth, Hale Bopp produced carbon monoxide (CO) emissions equal to that given off by 5.5 billion cars every day. Credit: E. Kolmhofer, H. Raab; Johannes-Kepler-Observatory, Linz, Austria 67
2.13 The heliosphere is a bubble in space "blown" into the interstellar medium (the hydrogen and helium gas that permeates the galaxy) by the solar wind. Although electrically neutral atoms from interstellar space can penetrate this bubble, virtually all of the material in the heliosphere emanates from the Sun itself. 68

2.14 AGB wind ionized by hot white dwarf at center 71
2.15 The Crab Nebula is a supernova remnant, an expanding cloud of debris from the death explosion of a massive star. Light from that stellar catastrophe was first witnessed by astronomers on planet Earth in the year 1054. Colors in the intricate filaments trace the light emitted from atoms of hydrogen, oxygen, and sulfur in the debris cloud. The erie blue interior glow is emitted by high-energy electrons accelerated by the Crab's central pulsar. One of the most exotic objects known to modern astronomers, the pulsar is a neutron star, the spinning remnant of the collapsed stellar core. 73
2.16 energy conserving blast wave phase & momentum conserving snowplow phase: F. Shu (1992) . 75

3.1 Saturn's rings are confined to a plane many times thinner, in proportion, than a razor blade. A series of plane crossing images from late February was dug out of the vast online Cassini raw image archive by interested Spanish amateur Fernando Garcia Navarro. Pictured above, digitally cropped and set in representative colors, is the striking result. Saturn's thin ring plane appears in blue, bands and clouds in Saturn's upper atmosphere appear in gold, and dark shadows of the rings curve across the top of the gas giant planet. Moons appear as bumps in the rings. Credit: Cassini Imaging Team, SSI, JPL, ESA, NASA 78
3.2 Balbus & Hawley: Rev. Mod. Phys. 70, 1 - 53 (1998) 81
3.3 $D \equiv \kappa^2 - m^2(\Omega - \Omega_p)^2$ 84
3.4 Pan, is an egg shaped body whose long axis points toward Saturn. It has a mean radius of 14 km and maintains the 325 km wide Encke Gap in Saturn's A ring. The image was taken shortly before the time of Saturn's August 2009 equinox and the low Sun angle is responsible for Pan's long shadow on the rings. Pan is named after a satyr (a creature resembling a man with the hind legs and hooves of a goat) who was a Greek god of nature and the forest. Image Credit: NASA/JPL/Space Science Institute 86
3.5 M51: Cosmic Whirlpool. The galaxy, has well defined spiral structure apparently excited by its companion galaxy (right). The pair are at a distance of about 10 million parsecs. Credit: S. Beckwith (STScI) Hubble Heritage Team, (STScI/AURA), ESA, NASA 87
3.6 91

3.7 Diagram showing how Mercury's orbital period and rotational period are locked in a 3:2 resonance. Original author: Worldtraveller 95
3.8 Two sulfurous eruptions are visible on Jupiter's volcanic moon Io in this color composite image from the robotic Galileo spacecraft. At the top, over Io's limb, a bluish plume rises about 140 kilometers above the surface of a volcanic caldera known as Pillan Patera. In the image middle, near the night/day shadow line, the ring shaped Prometheus plume is seen rising about 75 kilometers, or about 46 miles, above Io while casting a shadow below the volcanic vent. Credit: NASA/JPL 96

4.1 102
4.2 Sunspot area within the group spanned is more than 13 times the entire surface of the Earth! It was the source of numerous flares and coronal mass ejections. Caused by intense magnetic fields emerging from the interior, a sunspot appears to be dark only when contrasted against the rest of the solar surface, because it is slightly cooler than the unmarked regions. Credit: NASA/SOHO.ESA 105
4.3 Sunspot Butterfly diagram. Credit: David Hathaway, NASA Marshall Space Flight Center . . 106
4.4 An EIT image in the Fe XV 284 Angstrom wavelength of extreme UV light from each year of nearly an entire solar cycle. Credit: NASA/SOHO.ESA 107
4.5 Bipolar magnetic regions (BMR's) are formed where buoyant flux loops of submerged toroidal field are brought to the surface. The BMR's continue to expand and the flux loops rise higher into the corona: credit Babcock (1961) ApJ 108
4.6 The expanding field lines above the older BMR's reconnect with those of the main dipole field liberating large loops of low intensity field. Continuation of this process results in the formation of a new main dipole field of reversed polarity. Babcock (1961) ApJ 109
4.7 Drawing of Earth's magnetosphere. Notice that the magnetic field is much larger than the planet. credit: Windows to the Universe 113

4.8 Aurora borealis on Jupiter. Three bright dots are created by magnetic flux tubes that connect to the Jovian moons Io (on the left), Ganymede (on the bottom) and Europa (also on the bottom). In addition, the very bright almost circular region, called the main oval, and the fainter polar aurora can be seen. Credit: John T. Clarke (U. Michigan), NASA image in UV, Hubble Space Telescope 115
4.9 credit: Anatoly Spitkovsky's home page 118
4.10 The deep x-ray image gives the first clear view of the convoluted boundaries of the Crab's pulsar wind nebula. The pulsar is the collapsed core of a massive star with more mass than the Sun and the density of an atomic nucleus. It was born in a supernova explosion that was witnessed in the year 1054. This Chandra image spans just under 3 pc at the Crab's estimated distance of 2 kpc. Credit: NASA / CXC / SAO / F. D. Seward, W. H. Tucker, R. A. Fesen . . 119
4.11 False color image of the radio jet and lobes in the hyperluminous radio galaxy Cygnus A. Red shows regions with the brightest radio emission, while blue shows regions of fainter emission. Multiconfiguration VLA observations of Cygnus A at 1.4 and 5 GHz have been used to produce detailed maps of exceptional dynamic range. A radio jet extends from the core into the northwest lobe. The broad radio lobes reveal an unexpected wealth of filamentary structure. Two new hot spots are identified. The pressure of the cluster gas in which Cyg A is embedded appears to be insufficient to confine either the jet or the filaments. From the necessarily high mechanical luminosity of the jet and the high energy densities of the hot spots, it is concluded that the jet is probably relativistic. The surface brightness of the jet is high in absolute terms, but the total radiated power of the jet is only 0.001 of that of the whole source. Investigators: R. Perley, C. Carilli & J. Dreher: Image courtesy of NRAO/AUI 120

5.1 Pulsar dispersion. Uncorrected dispersive delays for a pulsar observation over a bandwidth of 288 MHz centered at 1380 MHz. The delays wrap since the data are folded (i.e. averaged) modulo the pulse period. (From the Handbook of Pulsar Astronomy, by Lorimer and Kramer) 135

5.2 Thin Screen Diffraction/Scattering model. Inhomogeneities in the ISM cause small-angle deviations in the paths of the radio waves. These deviations result in time (and therefore phase) delays that interfere to create a diffraction pattern, broaden the pulses in time, and make a larger image of the pulsar on the sky. (From the Handbook of Pulsar Astronomy, by Lorimer and Kramer) 136
5.3 Pulse broadening caused by scattering. Scattering of the pulsed signal by ISM inhomogeneities results in delays that cause a scattering tail. (From the Handbook of Pulsar Astronomy, by Lorimer and Kramer) 137
5.4 PSR B1133+16, shows multiple scintillation arcs on occasion. The broad, asymmetric power distribution in (a) has numerous arclets at 321 MHz. Panels (b) and (c) are at frequencies above 1 GHz. Panel (b) shows two clear arcs (along with a horizontal line at f_t due to narrowband radio frequency interference and the sidelobe response of power near the origin). Four months later (panel [c]), only the outer of these two arcs, widened by the $a \propto \nu^{-2}$ scaling, is visible. From Cordes et al. in the Astrophysical Journal, 637:346-365, 2006 138
5.5 Wave packet distortion through field-line wander. Left: Sample of field lines perturbed by downward-propagating waves. Right: Distortion of an originally circular bulls-eye pattern as it moves upward following these field lines. Maron & Goldreich (2001) 147

Chapter 1

Evolution of Gravitationally Bound Bodies

1.1 Classification Of Gravitationally Bound Systems

- gravity balanced by thermal pressure
  - protostars, stars, stellar clusters, elliptical galaxies
- gravity balanced by rotation
  - planetary rings, accretion disks, disk galaxies
- gravity balanced by degeneracy pressure
  - planets, brown dwarfs, white dwarfs, neutron stars
- gravity not balanced by anything
  - black holes

1.2 Systems Supported By Thermal Pressure

- energy flows down a temperature gradient
  - consider the transfer of heat between two bodies of fixed volume $dE = TdS$, along with the second law, $dS_1 + dS_2 \geq 0$, implies $(T_2 - T_1)dE_1 \geq 0$
- systems supported by thermal pressure have negative heat capacity
  - $E \sim -GM^2/R$, together with $dp/dr = -g\rho$, yields $C_E \equiv (\partial E/\partial T)_M \sim E/T < 0$
  - applies to bodies supported by either gas pressure or radiation pressure

1.2.1 three examples

star

- stars radiate energy into cold space and become hotter and denser
  - $R \sim GM^2/(-E), \quad kT \sim GMm/R$
  - contraction is temporarily halted each time a new nuclear fuel ignites.

globular cluster

- energetic stars evaporate carrying away mass but almost no energy
  - cluster contracts and random velocities increase
    - ∗ $R \propto M^2$ so $\rho \propto M^{-5}$ and $v^2 \propto M^{-1}$
  - core collapse halted by energy input from binary stars
  - two body scatterings repopulate high energy tail of stellar velocity distribution

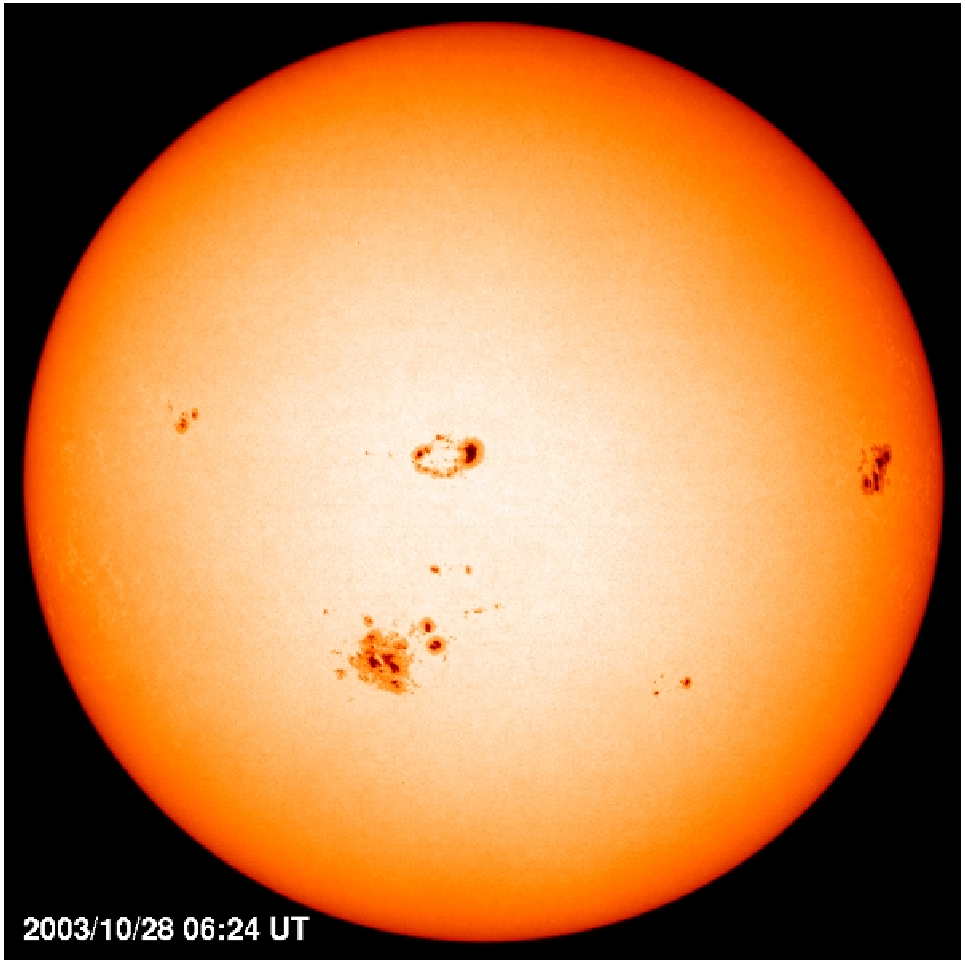

Figure 1.1: Our Sun with numerous large spots from 2003. Credit: SOHO (ESA & NASA)

Figure 1.2: M80 (NGC 6093) is one of the densest of the 147 known globular star clusters in the Milky Way galaxy. Located about 9 kpc, M80 contains hundreds of thousands of stars bound by their mutual gravitational attraction. All the stars in the cluster have the same age (about 15 billion years), but cover a range of stellar masses. Every star visible in this image is either more highly evolved than, or in a few rare cases more massive than, our own Sun. Especially obvious are the bright red giants that are nearing the ends of their lives. Credit: The Hubble Heritage Team (AURA/ STScI/ NASA)

elliptical galaxy

1.3 Systems Supported By Rotation

- angular momentum flows down angular velocity gradients
  - consider angular momentum transfer between two bodies
    $dE = \Omega dH$, along with dissipation of energy, $dE_1 + dE_2 \leq 0$, implies $(\Omega_2 - \Omega_1)dH_1 \geq 0$
  - $\Omega(r)$ decreases with increasing r provided M_r/r^3 does
  - $r^2\Omega$ increases with r under almost all circumstances
  - angular momentum is transported toward larger r
- systems supported by rotation have negative angular momentum capacity
  - $H \sim MR^2\Omega$, together with $\Omega^2 R^3 = GM$, yields $H \sim G^{2/3}M^{5/3}/\Omega^{1/3}$
  - $C_H \equiv \partial H/\partial\Omega \sim -MR^2$.

1.3.1 three examples

Earth-Moon system

- only orbital motion involves gravity supported by rotation
  - Earth and Moon are supported by degeneracy pressure
- tidal torque transfers angular momentum from the Earth's spin to the Moon's orbit
  - Moon's orbit expands by about 3 cm/yr, both the day and the month lengthen
  - effects are readily detected
- mechanical energy is dissipated as heat in the Earth's oceans and interior

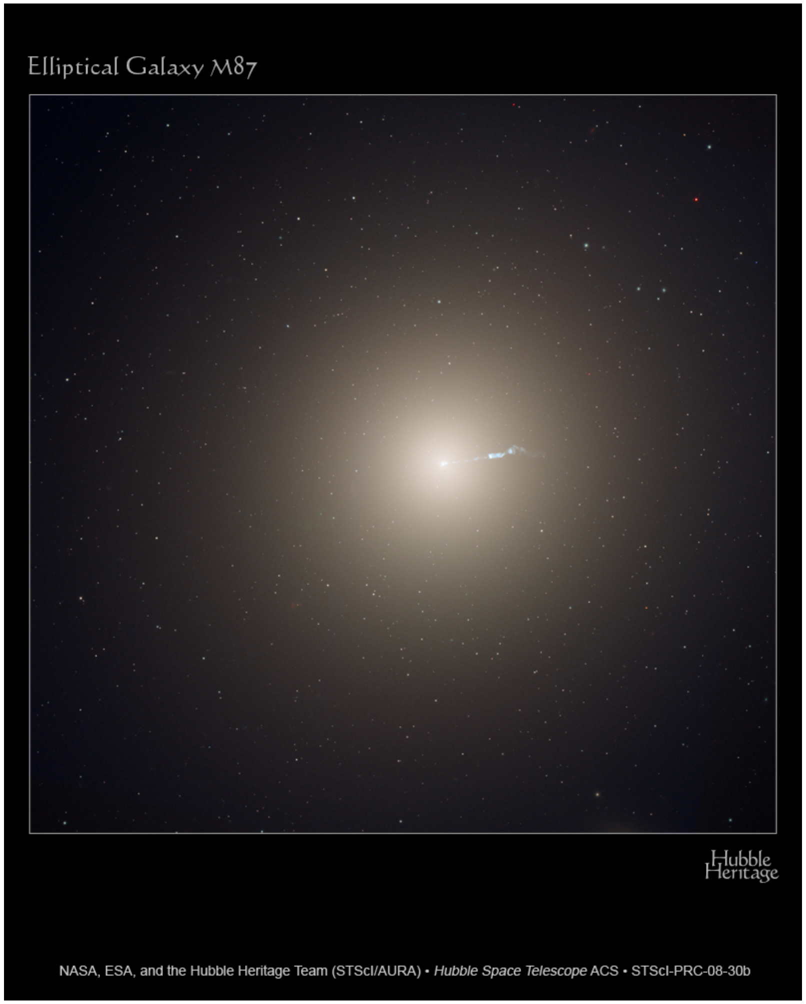

Figure 1.3: M87 is the dominant galaxy at the center of the neighboring Virgo cluster of galaxies, which contains some 2,000 galaxies. Amid the smooth, yellow population of older stars, the two features that stand out, the soft blue jet and the myriad of starlike globular clusters. Credit: NASA, ESA, and the Hubble Heritage Team (STScI/AURA)

Figure 1.4: Earth-Moon system as seen from Mars: credit NASA

accretion disk

- angular momentum flows down angular velocity gradient
  - angular momentum is conserved
  - mechanical energy is dissipated as heat
- inner regions contract and spin faster and outer regions expand and spin more slowly

disk galaxy

1.4 Systems Supported By Degeneracy Pressure

- radiate energy and cool down without much contraction

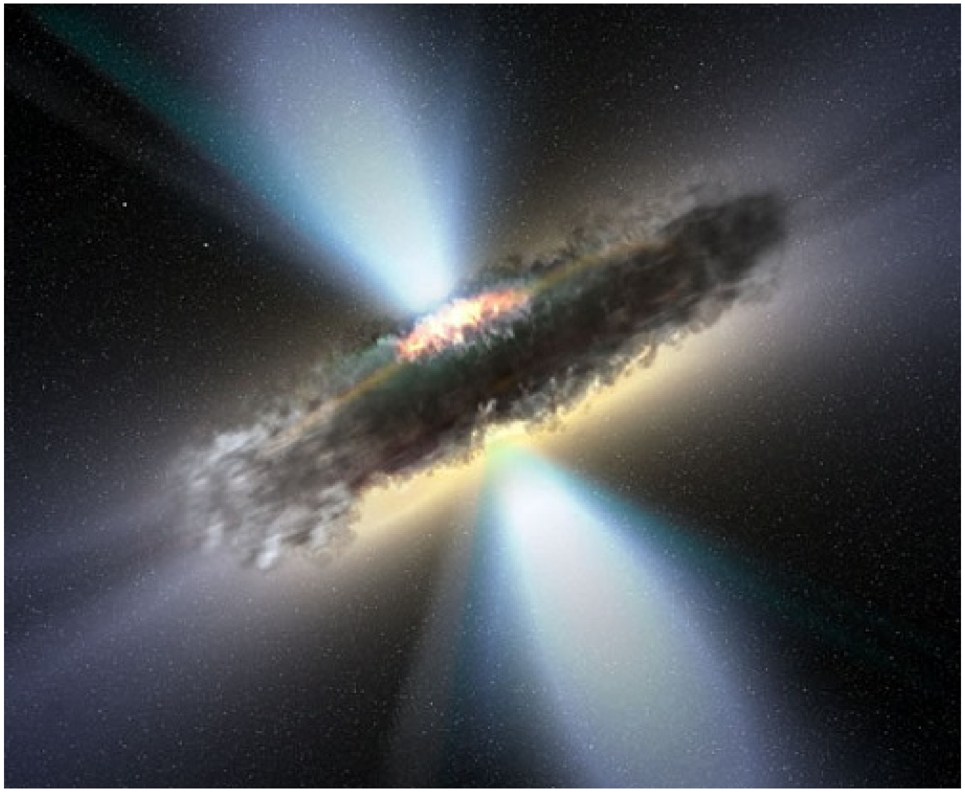

Figure 1.5: This image is an artist's conception of a black hole inside an accretion disk feeding a black hole and giving rise to a spin-aligned jet. credit: ESA

Figure 1.6: The Sombrero galaxy exhibits a brilliant white, bulbous core encircled by the thick dust lanes comprising its spiral structure. We view it from just six degrees north of its equatorial plane. The Sombrero is one of the most massive objects in Virgo cluster which is at about a distance of 9 Mpc. Credit: NASA and The Hubble Heritage Team (STScI/AURA)

Figure 1.7: Frosty white water ice clouds and swirling orange dust storms above a vivid rusty landscape reveal Mars as a dynamic planet in this sharpest view ever obtained by an Earth-based telescope. The colors have been carefully balanced to give a realistic view of Mars' hues as they might appear through a telescope.Credit: NASA and the Hubble Heritage Team (STScI/AURA) Acknowledgment: J. Bell (Cornell U.)

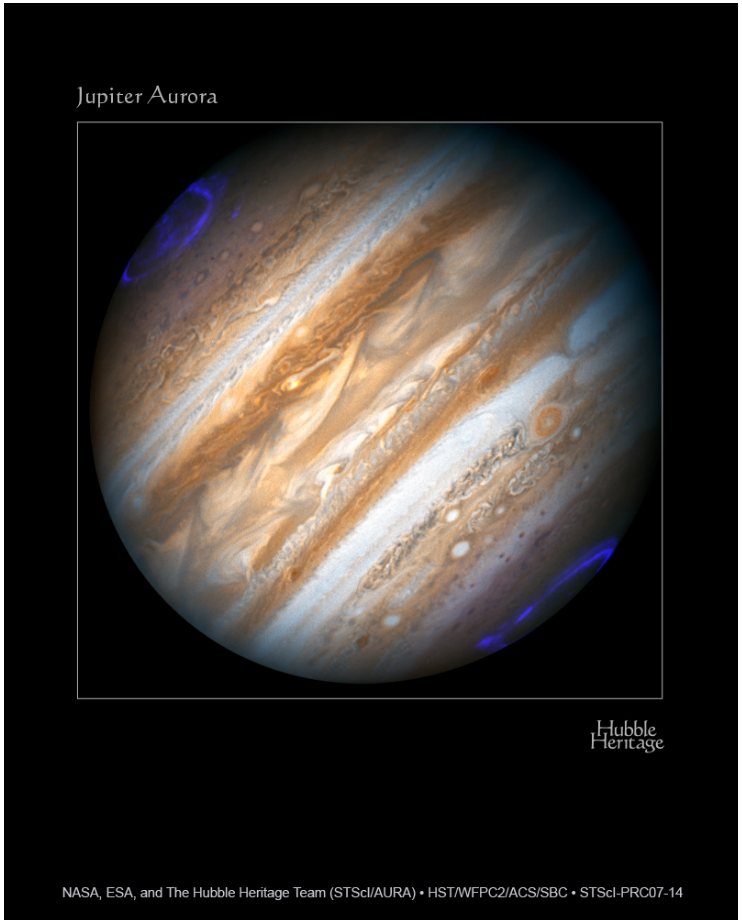

Figure 1.8: A composite made from ultraviolet- and visible-light images of Jupiter. The glowing aurorae near Jupiters North and South Poles were imaged in the UV and the cloudtops are seen through blue and red filters . Aurorae are produced when energetic charged particles precipitate near the planet's magnetic poles and cause hydrogen to fluoresce high in Jupiter's atmosphere. Credit: NASA, ESA, and the Hubble Heritage Team (STScI/AURA) Acknowledgment: H. Weaver (JHU/APL) and A. Simon-Miller (NASA/GSFC)

Chapter 2

Stars

2.1 Structure

2.1.1 3 well-separated time scales

- hydrostatic equilibrium imposed on dynamic timescale, $(G\rho)^{-1/2} \sim R/c_s$
  - oscillation period of breathing mode, period of grazing orbit
- radiative equilibrium reached on Kelvin-Helmholtz cooling time, GM^2/RL
  - luminosity, L, is determined from M, R, and κ without reference to nuclear energy generation
- nuclear equilibrium timescale is set by exhaustion of fuel at luminosity L
  - much longer than radiative timescale

timescales for Sun

- hydrostatic timescale: 3×10^3 seconds

- radiative timescale: 3×10^7 years
- nuclear timescale for hydrogen burning: 10^{10} years

2.1.2 hydrostatics

- stars are bound by gravity and supported by pressure
  - pressure is due to thermal motions of electrons, ions, and photons in nondegenerate stars
- mass radius relation

$$R \sim \frac{GMm_n}{kT} \tag{2.1}$$

- as stars lose energy they contract and get hotter and denser
  - on main sequence T is set by hydrogen burning and is insensitive to mass
  - more massive stars have lower density, $\rho \propto M^{-2}$ at fixed T

2.1.3 energy transport

- radiative diffusion and convection in non-degenerate stars
  - radiative flux

$$F_{rad} = -\frac{4ac}{3\kappa\rho}T^3\frac{dT}{dr} \tag{2.2}$$

  - analogy to thermal conduction, κ is opacity per gm, derivation from gradient of radiation pressure
  - opacity due to photoionization and electron scattering
- convection occurs if $ds/dr < 0$

- entropy gradients in convection zones are given by

$$\frac{H}{c_p}\frac{ds}{dr} \sim \left(\frac{F_{cv}}{\rho c_s^3}\right)^{2/3} \tag{2.3}$$

    - $H \sim c_c^2/g$ is the scale height

- convective velocities satisfy

$$\frac{v_{cv}}{c_s} \sim \left(\frac{F_{cv}}{\rho c_s^3}\right)^{1/3} \tag{2.4}$$

2.1.4 nuclear fusion

- electrostatic repulsion of nuclei impedes nuclear fusion,
  - coulomb barrier $\sim Z^2/A^{1/3}\,\mathrm{MeV}$ determines characteristic temperature, T_n, for nuclear burning
  - reactions aided by energetic nuclei tunneling through barrier
  - $T_n \approx 10^7\,\mathrm{K}$ for hydrogen and $\approx 10^8\,\mathrm{K}$ for helium
- maximum temperature, T_{max}, for a star of mass M limited by electron degeneracy
  - mass-radius relations for electron degeneracy and thermal pressure yield

$$\frac{kT_{max}}{m_e c^2} \sim \left(\frac{Gm_n^2}{\hbar c}\right)^2 \left(\frac{M}{m_n}\right)^{4/3} \tag{2.5}$$

  - $T_{max} \propto M^{4/3}$; only massive stars can burn high Z fuels

2.2 Evolution

2.2.1 contraction onto main sequence

- contraction halted by ignition of hydrogen when $T_c \approx 10^7\,\mathrm{K}$
  - condensations with $M < 0.07 M_\odot$ become degenerate before igniting hydrogen
    - yield brown dwarfs
  - range of initial stellar masses, $0.07 M_\odot < M \approx 100 M_\odot$
  - initial mass function peaks above minimum mass for hydrogen burning
  - upper limit is likely related to dominance of radiation pressure over gas pressure
- aside on stability at fixed M
  - gravitational energy $\propto 1/R$, kinetic energy of monatomic gas $\propto 1/R^2$, energy in radiation $\propto 1/R$

2.2.2 main sequence

- longest stage in stellar lifetime
  - burning hydrogen to helium releases $0.007mc^2$
  - burning helium to iron only releases an additional $0.001mc^2$
  - ^{56}Fe is the most tightly bound nucleus
- Sun is 4.6 billion years old
  - main sequence lifetime of Sun is about $10^{10}\,\mathrm{yr}$
  - Sun is a middle age star
- L, increases $\propto M^4$ around $M_\odot$

  - consequence of $\rho \propto M^{-2}$ for fixed T
  - radiation escapes more easily at lower ρ
  - $L \propto r/\rho \propto M^3$ for fixed T and κ
  - massive stars have shorter lives

2.2.3 post-main sequence evolution

- irrelevant for low mass stars
  - even the oldest stars with $M < 0.8M_\odot$ have yet to evolve off the main sequence
- intermediate mass stars $0.8M_\odot < M < 8M_\odot$ leave white dwarf remnants
  - excess mass lost during red giant and asymptotic branch stages
  - $\dot{M}$ up to $10^{-4} M_\odot\,\mathrm{yr}^{-1}$ in gentle winds
  - evolution is controlled by mass loss, rate of mass loss exceeds that of nuclear burning
  - exposed stellar core ionizes circumstellar material, ionized shell is known as planetary nebula
  - about one planetary nebula is born in our galaxy each year, they have nothing to do with planets
  - $0.8M_\odot < M < 4M_\odot$ burn He but not C
- high mass stars $M > 8M_\odot$ die as supernovae
  - $8M_\odot < M < 12M_\odot$ may not leave a remnant
  - $M > 12M_\odot$ complete burning ends with iron core
    - core is effectively a massive white dwarf
    - core collapses when its mass grows to $1.4M_\odot$
    - core stiffens at nuclear density and an outward propagating shock is launched

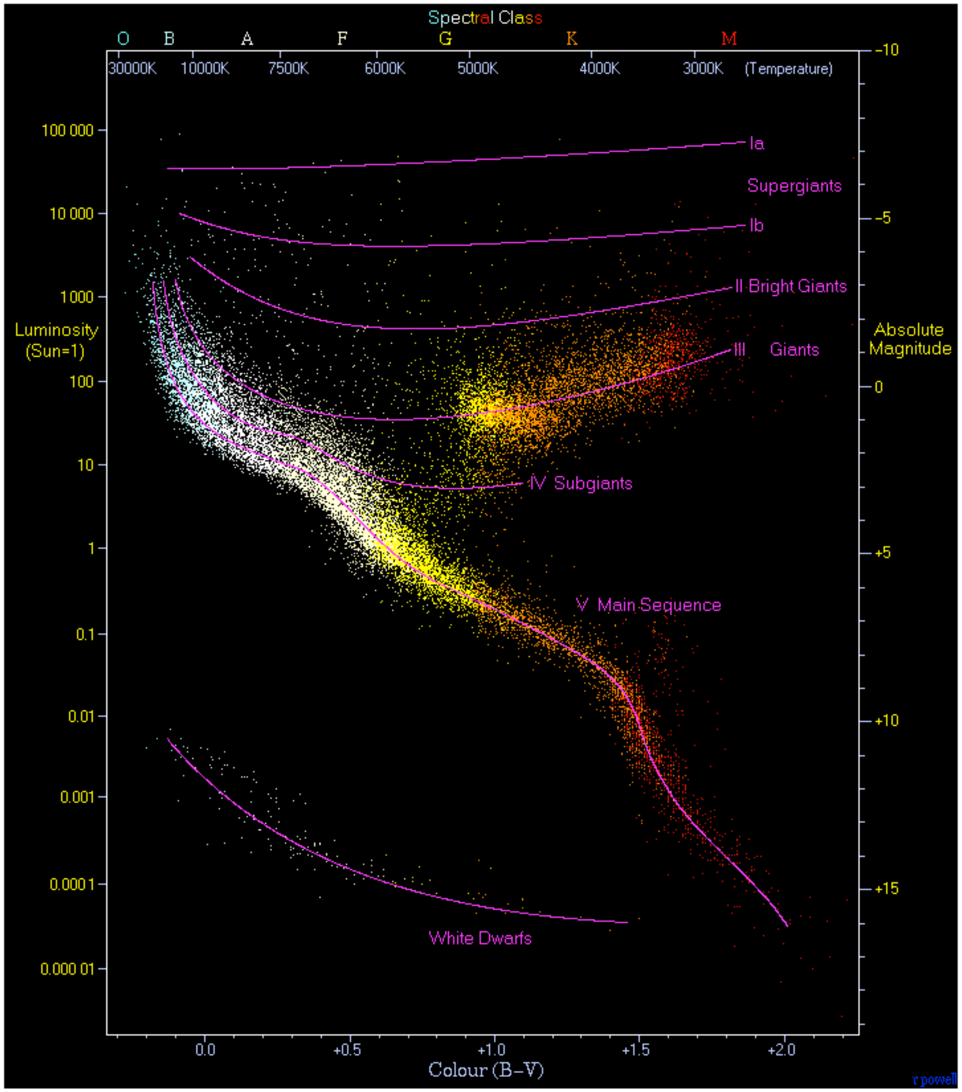

Figure 2.1: Hertzsprung-Russell diagram by Richard Powell with permission. 22,000 stars are plotted from the Hipparcos catalog and 1,000 from the Gliese catalog of nearby stars. An examination of the diagram shows that stars tend to fall only into certain regions on the diagram. The most predominant is the diagonal, going from the upper-left (hot and bright) to the lower-right (cooler and less bright), called the Main Sequence. In the lower-left is where white dwarfs are found, and above the main sequence are the subgiants, giants and supergiants. The Sun is found on the main sequence at luminosity 1 (absolute magnitude 4.8) and B-V color index 0.66 (temperature 5780K, spectral type G2).

  - stellar envelope is ejected giving rise to type II supernova
    - details of ejection remain murky
    - rate is about one per 50 years in our galaxy
    - one percent of binding energy goes into kinetic energy of ejecta
    - sufficient to produce expansion velocity $v/c \approx 0.03$
    - bulk of energy is emitted as neutrinos
  - possible remnants are neutron stars and black holes
  - neutron stars for $12M_\odot < M < 20M_\odot$, this is quite uncertain

2.3 Remants

2.3.1 White Dwarfs

- bound by gravity
- supported by pressure from degenerate electrons
  - solids bound by electrostatic forces
  - solids and liquids resist compression because of degenerate electrons
- mass radius relation

$$R \sim \frac{\hbar^2}{G m_e m_n^{5/3} M^{1/3}} \tag{2.6}$$

- maximum mass $\approx 1.4M_\odot$, minimum radius $\approx R_\oplus$

$$M_{max} \sim \left(\frac{\hbar c}{G m_n^2}\right)^{3/2} m_n \quad \text{and} \quad R_{min} \sim \left(\frac{\hbar c}{G m_n^2}\right)^{1/2} \frac{\hbar}{m_e c} \tag{2.7}$$

  - set by relativistic degeneracy of electrons

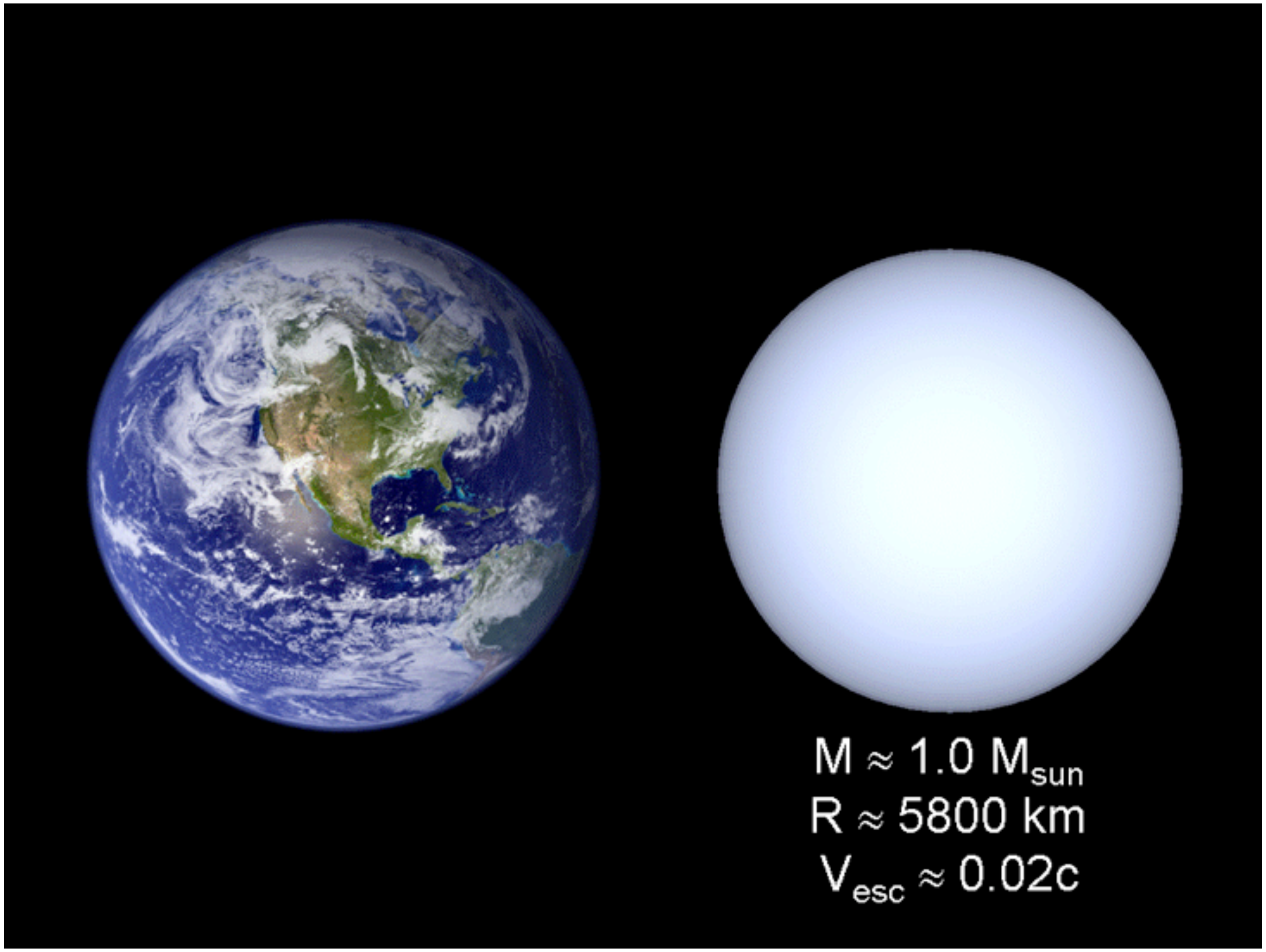

Figure 2.2: White Dwarfs are remnant cores of stars with $M < 8M_\odot$. They are supported against gravity by electron degeneracy pressure. Stars with $M < 4M_\odot$ yield C-O white dwarfs & Stars with $4M_\odot < M < 8M_\odot$ yield O-Ne-Mg white dwarfs. Credit: Richard Pogge

2.3.2 Neutron Stars

- bound by gravity
- supported by pressure from degenerate neutrons and repulsive strong force
  - nuclei bound by attractive strong force
  - resist compression due to nucleon degeneracy, repulsive strong & electrostatic forces
- mass radius relation based on degeneracy pressure

$$R \sim \frac{\hbar^2}{G m_n^{8/3} M^{1/3}} \tag{2.8}$$

$$R_{NS} \approx \frac{m_e}{m_n} R_{WD} \tag{2.9}$$

- maximum mass, $1.4 M_\odot < M_{max} < 3 M_\odot$, and minimum radius, $R_{min} \approx 10\,\mathrm{km}$

$$M_{max} \sim \left(\frac{\hbar c}{G m_n^2}\right)^{3/2} m_n \quad \text{and} \quad R_{min} \sim \left(\frac{\hbar c}{G m_n^2}\right)^{1/2} \frac{\hbar}{m_n c} \tag{2.10}$$

  - set by properties of repulsive strong force and general relativity

2.3.3 Black Holes

- space-time singularity, no restriction on mass
- black holes formed as stellar remnants probably have $M \geq 2 M_\odot$
- event horizon

$$R = \frac{2GM}{c^2} \approx 3 \left(\frac{M}{M_\odot}\right) \mathrm{km} \tag{2.11}$$

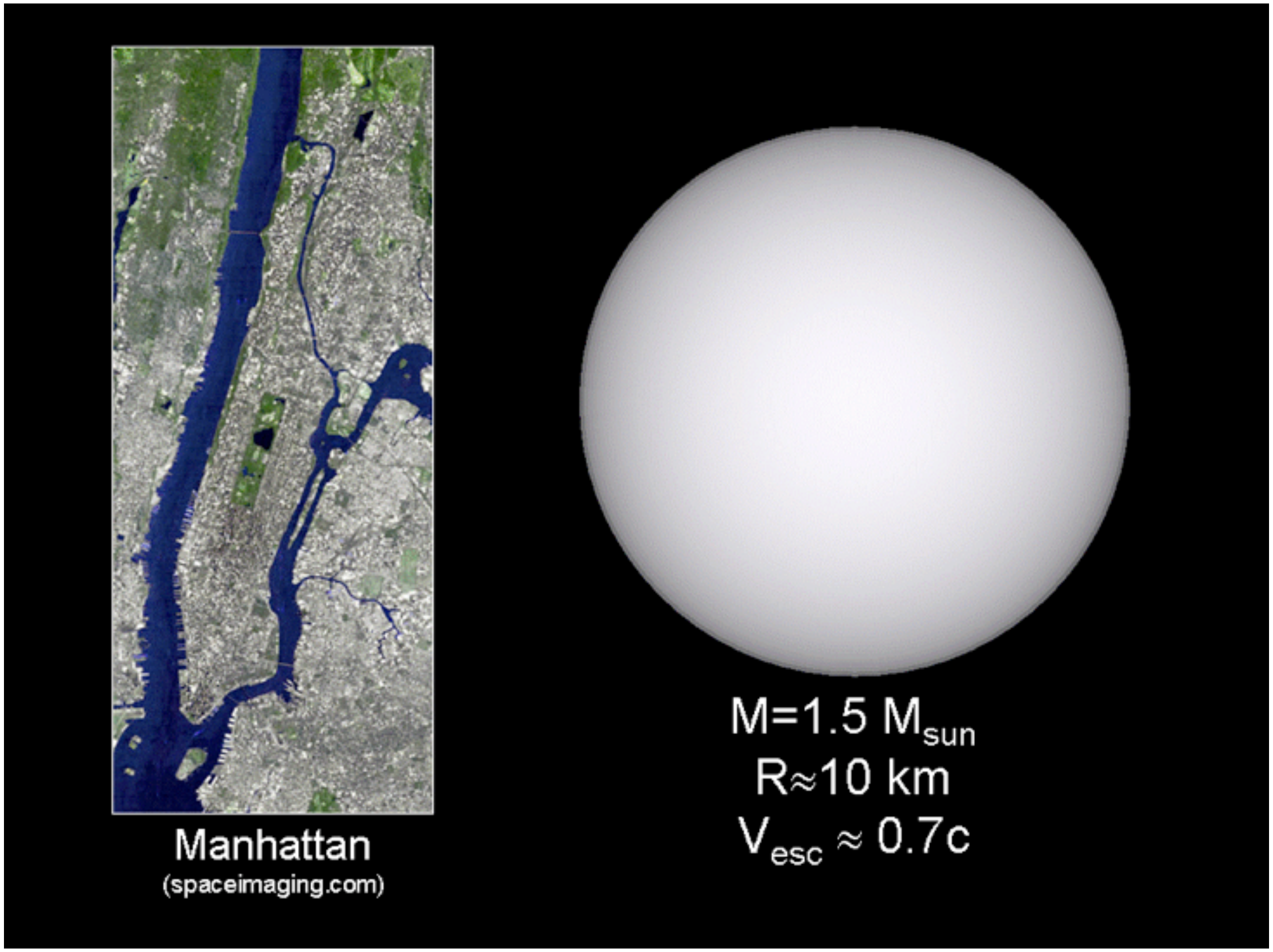

Figure 2.3: Neutron Stars are remnant cores of stars with $M > 12M_{\odot}$. They are supported against gravity by neutron degeneracy pressure and the strong repulsive force. Credit: Richard Pogge

2.4 Remnants Revealed

2.4.1 White Dwarfs

- thermal emission from cooling
- accretion from companions in binaries, cataclysmic variables, novae
- secondary characteristics
  - pulsators provide information about interiors
  - surface magnetic fields up to 7×10^8 G
    - measured from Zeeman splitting of lines and polarization of continuum
  - rotation periods from hours to decades

2.4.2 Neutron Stars

- pulsars
  - rotating neutron stars emitting beams of radiation
    - two broad classes, young and recycled
    - spin periods as short as milliseconds
    - despin rates yield estimates of magnetic fields up to 10^{14} G
- rotation powered pulsars
  - power provided by loss of rotational energy
  - most detected as radio emitters but also some in x-rays and gamma-rays
- accretion-powered pulsars

  - energy source is gravitational potential energy of accreted matter
  - emission is in x-rays

- magnetars
  - powered by energy from decay of an extremely strong magnetic field

2.4.3 Black Holes

- x-ray sources accreting matter from a close companion
  - x-rays are emitted from the surface of an accretion disk
  - companion's motion is determined by optical observations

2.5 Fluid Phenomena

2.5.1 Oscillation Modes of Non-Rotating Stars

classification

- eigenvalues: radial order n, angular degree ℓ, azimuthal separation parameter m
  - n is the number of nodes in the radial displacement eigenfunction
  - fundamental modes have $n = 0$
  - two modes for each $n > 0$ and given ℓ & m
  - acoustic or p-modes: trapped sound waves, high frequency mode with $n > 0$
  - gravity or g-modes: trapped internal gravity waves, low frequency mode with $n > 0$
- critical frequencies

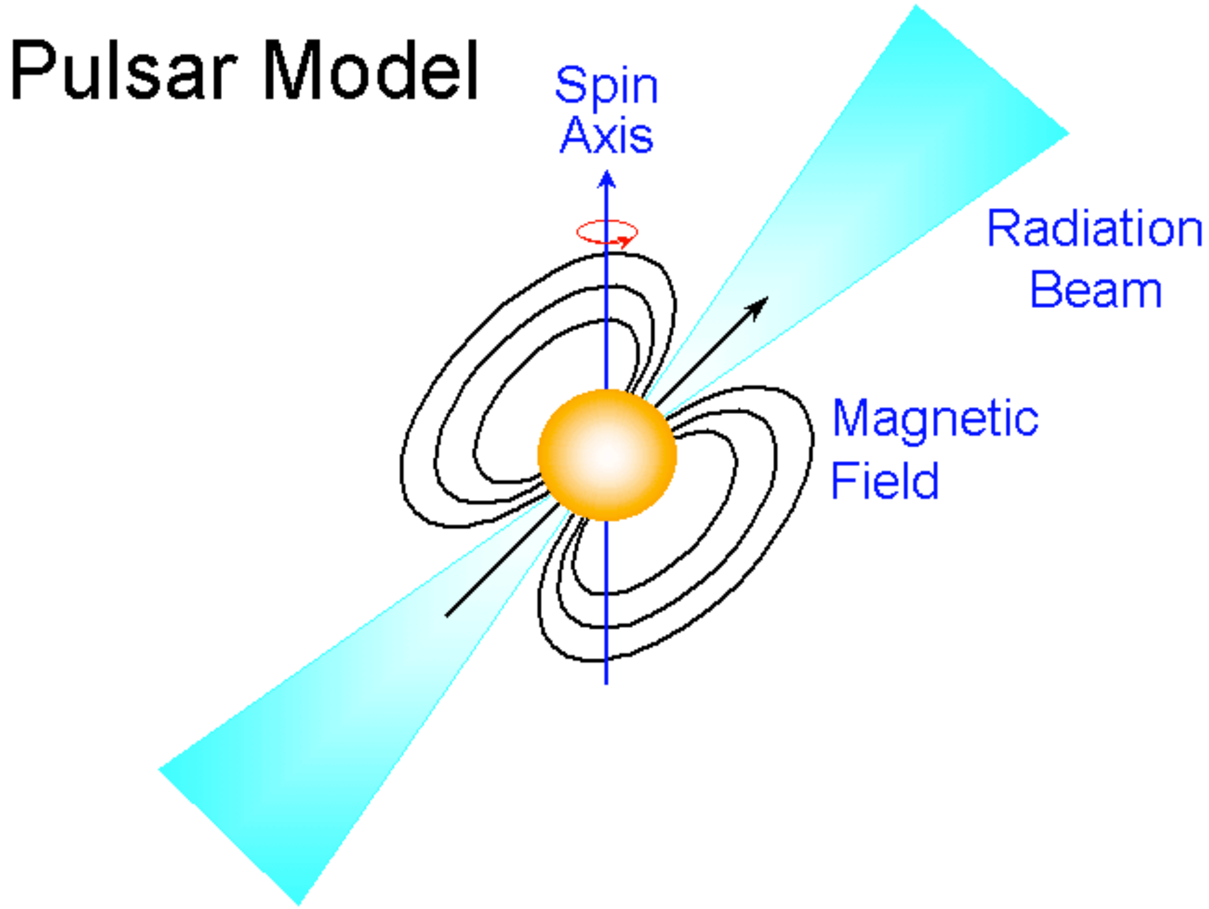

Figure 2.4: Pulsars are rapidly spinning, magnetized neutron stars. Spinning magnetic field generates a strong electric field which accelerates electrons and positrons along field lines that pass through the light cylinder. Credit: Richard Pogge

  - acoustic cutoff or Lamb frequency L_ℓ

$$L_\ell^2 \equiv \frac{\ell(\ell+1)c_s^2}{r^2} \tag{2.12}$$

  - buoyancy or Brunt frequency N

$$N^2 \equiv -\left(\frac{\partial \ln \rho}{\partial s}\right)_p g\frac{ds}{dr} \tag{2.13}$$

- WKB dispersion relation in Cowling approximation

$$k_r^2 = \frac{\left(\omega^2 - L_\ell^2\right)\left(\omega^2 - N^2\right)}{\omega^2 c_s^2} \tag{2.14}$$

- propagation diagram for polytropic star

characterization

f-modes

- analogous to surface gravity waves
  - incompressible in limit $\ell \to \infty$
  - $\omega^2 \approx g\ell(\ell+1)/r^2$
- excited radial f-modes observed in RR Lyraes and Cepheids

p-modes

- trapped sound waves

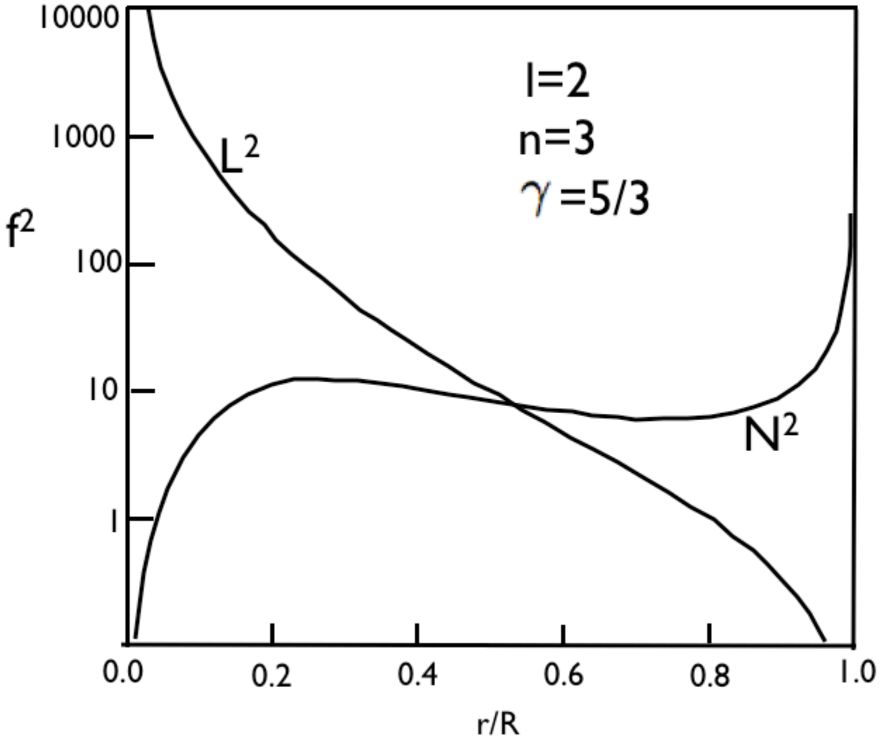

Figure 2.5: credit I. P. Lopes (2001)

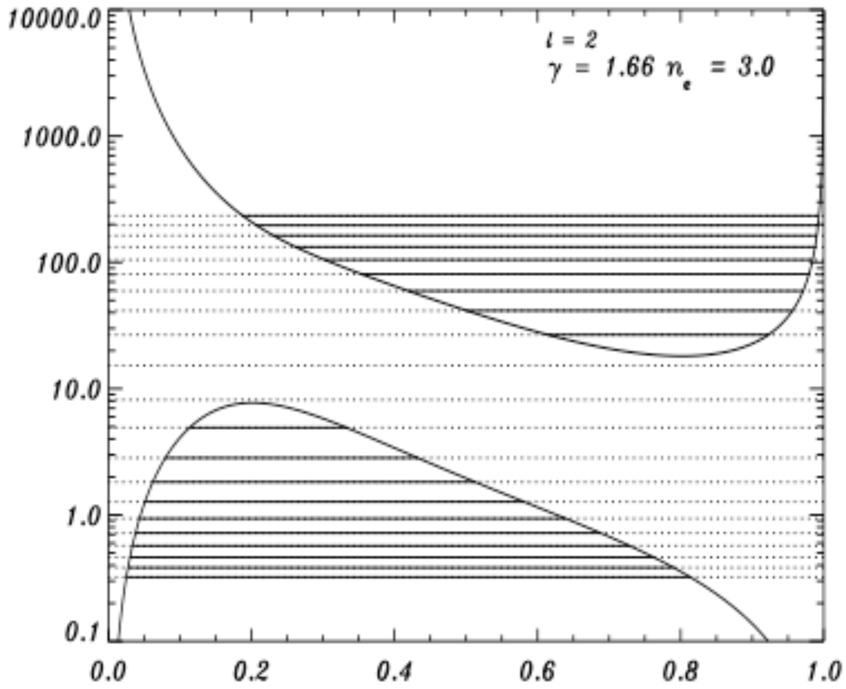

Fig. 3. Propagation diagram for a polytropic model with index $n_e = 3.0$, adiabatic index $\gamma = 5/3$ and modes of degree $l = 2$. The solid curves represent the critical frequencies $\omega_{\pm}$, delimiting the two propagation regions of the stellar oscillations as it is obtained from the first Cowling approximation motion equation (see text). The eigenstates corresponding to the eigenmodes with dimensionless square of the circular frequency, ω^2: 234, 196, 163, 132.4, 104.8, 80.55, 59.42, 41.47, 26.72, 15.26, 8.175, 4.915, 2.828, 1.822, 1.270, 0.9360, 0.7188.

Figure 2.6: credit I. P. Lopes (2001)

  - restoring force is pressure from compression
  - WKB dispersion relation

$$\omega^2 \approx k^2 c_s^2 \tag{2.15}$$

  - propagation cavity bounded by r_b where $k_r = 0$ and r_t where $k_r H \sim 1$
  - predominantly radial displacement and direction of propagation
  - n increases with increasing ω
  - WKB envelope of radial displacement satisfies $\rho c_s r^2 \xi_r^2$=constant
- excited solar p-modes

g-modes

- trapped internal gravity waves
  - restoring force is gravity acting on displacement of surfaces of constant density from equipotentials
  - WKB dispersion relation

$$\omega^2 = \frac{\ell(\ell+1)N^2}{\ell(\ell+1) + (k_r r)^2} \tag{2.16}$$

  - g-modes require $\ell > 0$ and do not propagate in convection zones
  - propagation cavity bounded by r_b where $\omega = N$ and r_t where $k_r H \sim 1$
  - predominantly horizontal displacements and direction of propagation
  - n increases with decreasing ω
  - WKB envelope of horizontal displacement satisfies $\rho r^3 \xi_h^2 / N \approx$constant
- excited g-modes of white dwarfs

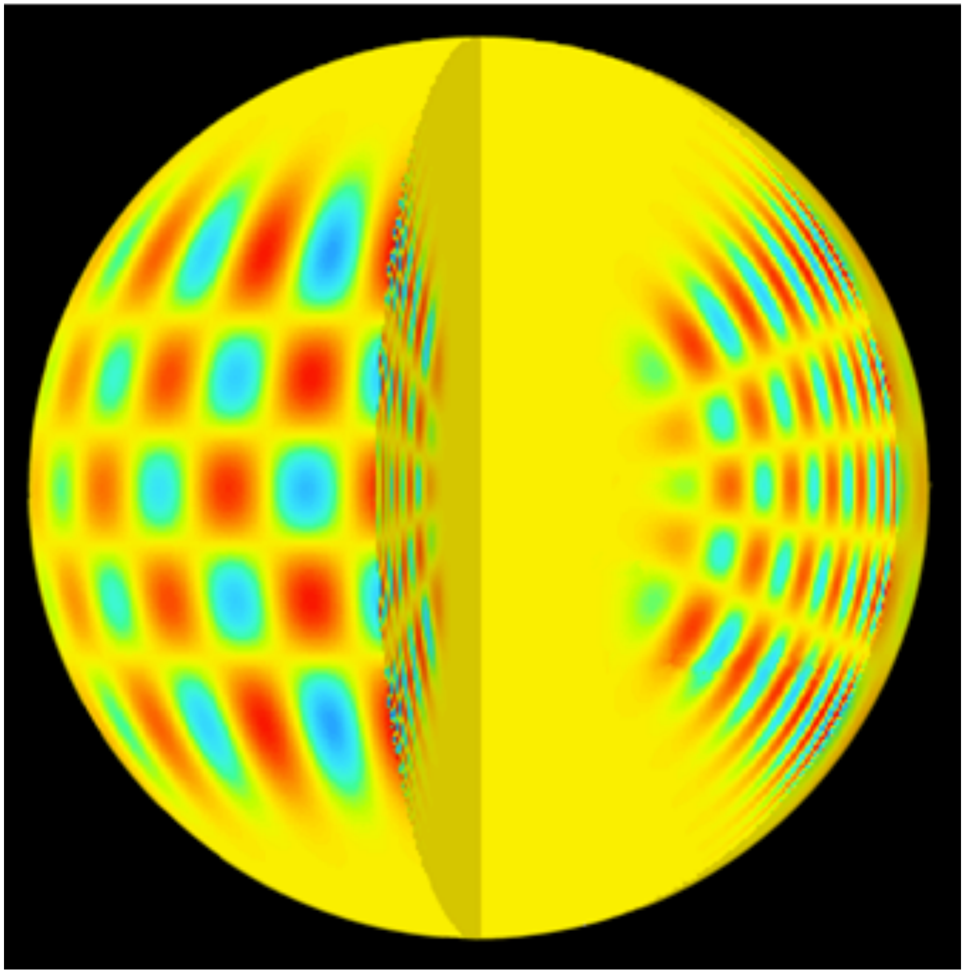

Figure 2.7: A computer-generated image showing the pattern of a p-mode solar acoustic oscillation both in the interior and on the surface of the sun. (l=20, m=16 and n=14.) Note that the increase in the speed of sound as waves approach the center of the sun causes a corresponding increase in the acoustic wavelength.

excitation

overstability due to opacity valve

- thermal engines in stars convert a portion of stellar luminosity to mechanical work
  - requires heat absorption at high T & release at low T
  - opacity mechanism in stellar instability strip works because $\kappa_T > 0$ where $\omega\tau_{th} \sim 1$
  - $\kappa_T > 0$ in regions where H or He is lightly ionized
- show work diagram

stochastic driving by turbulent convection

- emission and reabsorption of acoustic energy by turbulence
  - acoustic emission, far field component of turbulent pressure fluctuations, $\delta p \sim \rho v_{cv}^2$
  - absorption due to turbulent viscosity, $\nu_t \sim v_{cv}H$
  - strongest interactions occur at top of convection zone where v_{cv}/c_s is maximal
  - resonant modes, $\omega \sim v_{cv}/H$
- equipartition of mode energy with that of a resonant turbulent eddy yields

$$E_{mode} \sim \rho H^3 v_{cv}^2 \tag{2.17}$$

  - $F \sim \rho v_{cv}^3$ implies

$$E_{mode} \sim \frac{FH^2}{\omega} \tag{2.18}$$

  - radiative damping comparable to turbulent damping
  - stochastic excitation occurs where modes are evanescent

- application to helioseismology
  - $F \approx 7 \times 10^{10}\,\mathrm{erg\,cm^{-2}\,s^{-1}}$
  - at top of convection zone: $\rho \approx 10^{-6}\,\mathrm{g\,cm^{-3}}$, $v \approx 3\,\mathrm{km\,s^{-1}}$, $H \approx 1.5 \times 10^2\,\mathrm{km}$
  - $\omega \sim v/H \sim 2 \times 10^{-2}\,\mathrm{s^{-1}}$
  - $E \sim 10^{27}\,\mathrm{erg}$

saturation by parametric instability of damped modes

- consider the small amplitude oscillations of a swing hanging from a cord of length ℓ
  - basic equation

$$\frac{d^2\theta}{dt^2} + \left(\frac{2}{\ell}\frac{d\ell}{dt} + \gamma\right)\frac{d\theta}{dt} + \frac{g}{\ell}\theta = 0 \tag{2.19}$$

  - $\ell = \ell_0(1 - h\sin 2\omega t)$ with $h > 0$
  - define $\omega_0^2 = g/\ell_0$ and $\Delta\omega = \omega - \omega_0$
- make the ansatz

$$\theta = A\sin(\omega_0 t + \phi) \tag{2.20}$$

  - two new parameters, A and ϕ, have been defined
  - set $\dot\theta = \omega_0 A\cos(\omega_0 t + \phi)$ which imposes the constraint
  - $\dot A\sin(\omega_0 t + \phi) + \dot\phi A\cos(\omega_0 t + \phi) = 0$
  - first order odes for $\dot A$ and $\dot\phi$ follow from the equation of motion and the constraint
  - dropping high frequency terms, these take the form

$$\dot A \approx \frac{3}{4}\omega_0 h A\cos 2(\Delta\omega\, t - \phi) - \frac{\gamma}{2}A \qquad \text{and} \qquad \dot\phi \approx \frac{3}{4}\omega_0 h\sin 2(\Delta\omega\, t - \phi) \tag{2.21}$$

Figure 2.8: MDI Single Dopplergram Minus 45 Image Average Subtracting an average solar velocity image observed over 45 minutes from a single velocity image reveals the surface motions associated with sound waves traveling through the Sun's interior. The smallscale light and dark regions represent the up and down motions of the hot gas near the Sun's surface. The pattern falls off towards the limb because the acoustic waves are primarily radial.

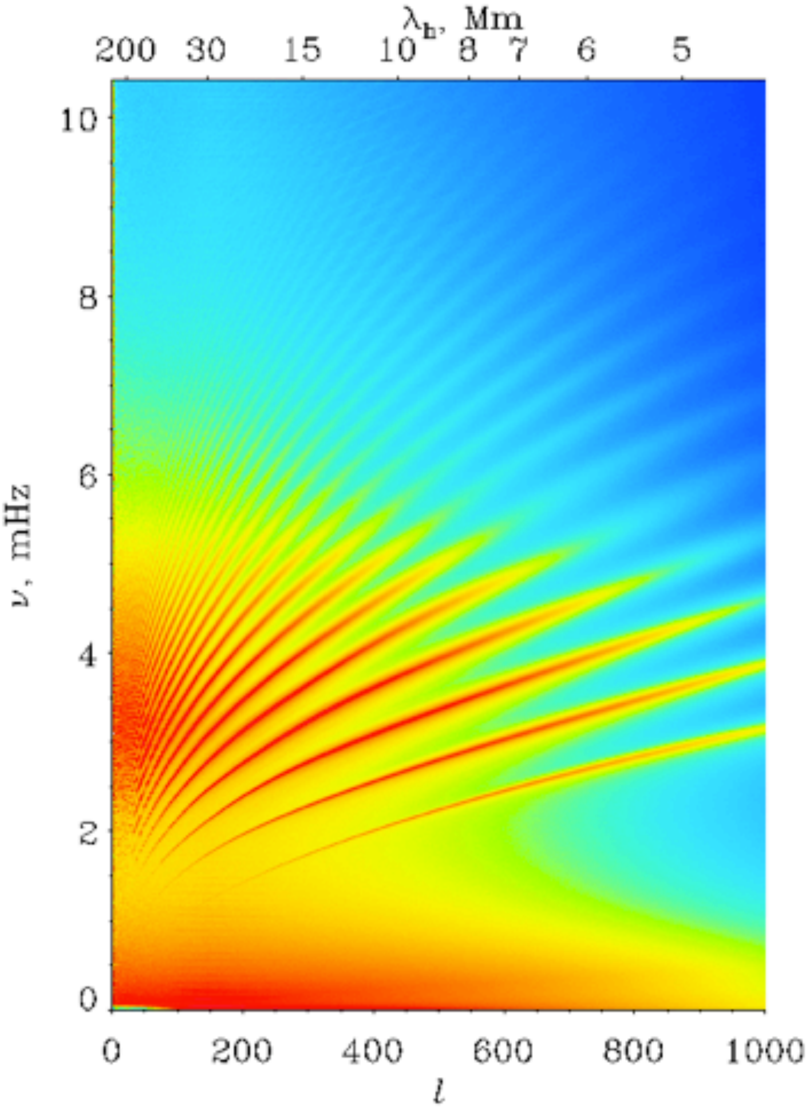

Figure 2.9: l-nu diagram from MDI high-cadence full disk data. Shows mode frequencies up to 10 milliHz and l=1000.

- criterion for parametric instability
  - phase ϕ is stable at $\phi = \phi_0 + \Delta\omega\, t$ for $\phi_0 < \pi/4$ where $\sin 2\phi_0 = -4\Delta\omega/(3\omega_0 h)$
  - amplitude equation may be recast as

$$\frac{1}{A}\frac{dA}{dt} = \frac{3}{4}\omega_0 h \cos 2\phi_0 - \frac{\gamma}{2} = \left[\left(\frac{3}{4}\omega_0 h\right)^2 - \Delta\omega^2\right]^{1/2} - \gamma/2 \tag{2.22}$$

  - condition of parametric instability reads

$$h > \frac{4}{3}\left[\left(\frac{\Delta\omega}{\omega_0}\right)^2 + \left(\frac{\gamma}{2\omega_0}\right)^2\right]^{1/2} \tag{2.23}$$

- criterion for instability at exact resonance can be determined in a more physical way
  - calculate average rate of work $-\dot{\ell}T$ done on swing where the tension

$$T = g\cos\theta + \ell\dot{\theta}^2 - \frac{d^2\ell}{dt^2} \tag{2.24}$$

  - $\phi_0 = 0$ implies that string is shortening most rapidly when it is vertical and tension is greatest
  - average work is positive, instability results if it exceeds average dissipation

2.5.2 Stellar Winds

thermal wind

- steady-state, spherically symmetric, isothermal model
  - conservation of mass

$$4\pi r^2 \rho v = \dot{M} \tag{2.25}$$

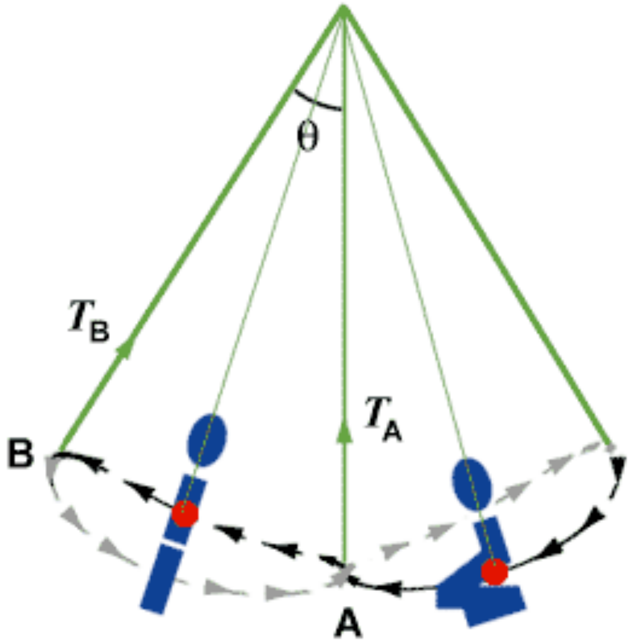

Fig. 2 The change in the position of the centre of mass when swinging with an increasing amplitude.

Figure 2.10: The broken line represents the route of the centre of mass of the child. When the boy swings to point A, he rises his body. Assuming that he rises his centre of mass by a distance d and the tension of the rope is T_A, he does positive work dT_A. When the boy swings to point B, he lowers his centre of mass and negative work dT_B. When the boy is at point B, his velocity is zero, so T_B is just the vertical component of his weight. But when he is at point A, his velocity is the greatest, T_B is the sum of his weight and the centripetal force. Hence energy is fed to the swing. Source: Prof. Lai Hon-ming. Translation by Sammy Tsui in Physics World

  - conservation of momentum

$$v\frac{\partial v}{\partial r} = -c_s^2\frac{\partial \ln \rho}{\partial r} - \frac{GM_\odot}{r^2} \tag{2.26}$$

  - energy equation replaced by isothermal equation of state, $p = c_s^2\rho$
    - ∗ electrons produce high thermal conductivity

- combine continuity and momentum equations to obtain

$$\left(\frac{1}{\mathcal{M}} - \mathcal{M}\right)\frac{\partial \mathcal{M}}{\partial r} = \frac{GM_\odot}{c_s^2 r^2} - \frac{2}{r} \tag{2.27}$$

  - $\mathcal{M} \equiv v/c_s$ is Mach number
  - right-hand side of equation must vanish at critical point, r_c, where Mach number $\mathcal{M} \equiv v/c_s = 1$

$$r_c = \frac{GM_\odot}{2c_s^2} \tag{2.28}$$

  - analogy with de Laval nozzles, transition from subsonic to supersonic flow in wind tunnels

- integrate equation of motion and evaluate constant of integration at r_c

$$\frac{\mathcal{M}^2}{2} - \ln \mathcal{M} = 2\frac{r_c}{r} + 2\ln\frac{r}{r_c} - \frac{3}{2} \tag{2.29}$$

- topology of solution curves
  - stationary upstream waves
  - Parker's argument for critical solution

application to solar wind

- thermally driven wind of plasma of approximately solar composition

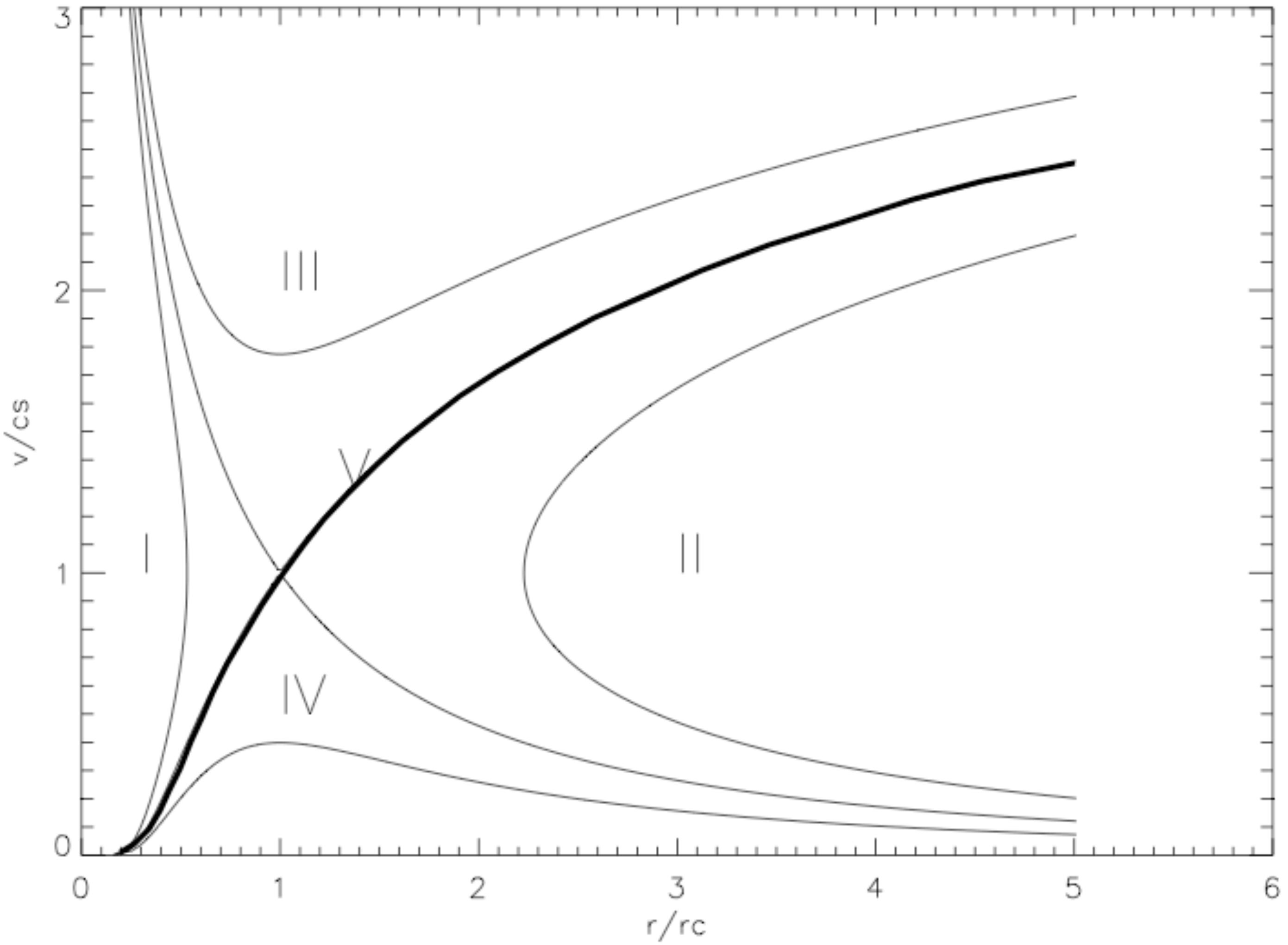

Figure 2.11: isothermal solar wind

- origin in solar atmosphere
  - photosphere, temperature minimum, chromosphere, corona
  - temperature inversion due to mechanical heating
  - role of convection and magnetic fields
- collisional mean free path is long but fluid description is appropriate even for shock waves
- $v \approx 400\,\mathrm{km\,s^{-1}}$ in ecliptic, independent of r, very gusty
- near Earth's orbit: $T \approx 10^5\,\mathrm{K}$, $n \approx 5\,\mathrm{cm^{-3}}$

connection to isothermal model

- estimate $\dot{M}$ at the base of the corona where $\mathcal{M} \ll 1$

$$\dot{M} \approx 4\pi r_c^2 \rho_b c_s \exp\left(\frac{3}{2} - 2\frac{r_c}{R_\odot}\right) \tag{2.30}$$

  - at base of corona $\rho \approx 10^{-15}\,\mathrm{g\,cm^{-3}}$ & $c_s \approx 1.3 \times 10^7\,\mathrm{cm\,s^{-1}}$
- above values yield $\dot{M} \approx 1.4 \times 10^{12}\,\mathrm{g\,s^{-1}} \approx 2 \times 10^{-14} M_\odot\,\mathrm{y^{-1}}$
  - $\mathrm{L}_\odot = 4 \times 10^{33}\,\mathrm{erg\,s^{-1}}$ corresponds to converting $10^{-11} M_\odot\,\mathrm{y^{-1}}$ of hydrogen to helium
- values for v and ρ at 1 AU are obtained by iterating equation for $\mathcal{M}$
  - $v \approx 5 \times 10^2\,\mathrm{km\,s^{-1}}$
  - $\rho \approx 10^{-23}\,\mathrm{g\,cm^{-3}}$

heliosphere, solar wind cavity in interstellar gas, terminal shock, heliopause, bow shock

- size set by balance of ram pressure of solar wind and pressure of interstellar medium

  - stress balance occurs at $r \approx 150\,\mathrm{AU}$
  - motion of SS may make ISM ram pressure greater than static p

- radio emission at $\nu \approx 2 - 3\,$kilohertz from heliopause triggered by interplanetary shock
  - detected by Voyagers 1 and 2, reference: Science, volume 262, p. 199
  - frequency corresponds to plasma frequency with $n_e \approx 5 \times 10^{-2}\,\mathrm{cm}^{-3}$
  - estimated distance to the heliopause $116 - 177\,\mathrm{AU}$, from time lag

magnetic field in solar wind

- radial variation at $r \gg R_\odot$
  - $B_r \propto r^{-2}$ from flux conservation
  - $B_\phi \propto r^{-1}$ for constant angular momentum flux

- particles carry a small fraction of the angular momentum flux

- magnetic field lines trace out an Archimedean spiral
  - solar wind velocity is almost radial but solar cosmic rays follow field lines
  - low-energy, galactic cosmic rays cannot propagate upstream against wind

radiatively driven, ionized winds of O stars

- O star winds are driven by radiation scattered by resonance lines that cover much of UV

- wind velocities are of order a couple of times the escape velocity from the photosphere

- momentum per unit mass is comparable to that in stellar flux, L/c
  - $v \sim 2 \times 10^3\,\mathrm{km\,s}^{-1}$

Figure 2.12: Two tails of comet Hale-Bopp. The blue tail of ionized gas interacts with the solar wind and points radially away from the Sun. The dust in the yellowish tail moves under the combined effects of gravity and radiation pressure. CO^+ is the source of the blue light. When it was the same distance from the Sun as Earth, Hale Bopp produced carbon monoxide (CO) emissions equal to that given off by 5.5 billion cars every day. Credit: E. Kolmhofer, H. Raab; Johannes-Kepler-Observatory, Linz, Austria

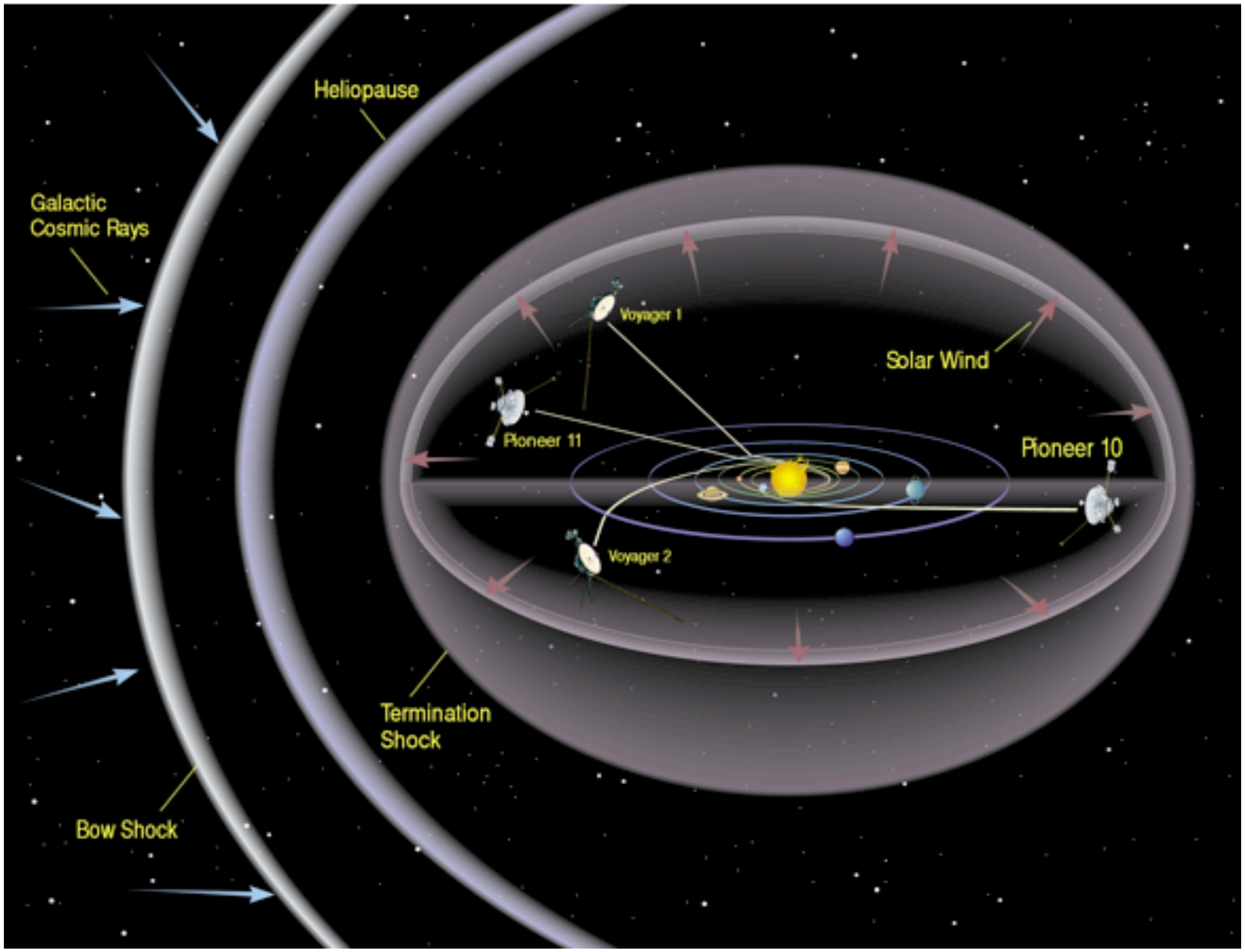

Figure 2.13: The heliosphere is a bubble in space ”blown” into the interstellar medium (the hydrogen and helium gas that permeates the galaxy) by the solar wind. Although electrically neutral atoms from interstellar space can penetrate this bubble, virtually all of the material in the heliosphere emanates from the Sun itself.

  - $\dot{M} \sim 10^{-6} M_\odot\,\mathrm{y}^{-1}$
  - rate at which mass is lost can approach that at which hydrogen is fused to helium

molecular winds of AGB stars

- AGB stars of solar mass have $L \sim 10^4 L_\odot$ and radii up to AU
- mass loss is driven by combination of pulsation and radiation pressure acting on dust grains
  - $\dot{M}$ up to $10^{-4} M_\odot\,\mathrm{y}^{-1}$ in slow winds
- mass is lost more rapidly than it is consumed by nuclear reactions

2.5.3 Supernova Remnants

- 3 phases: 1) free expansion of the ejecta; 2) adiabatic blast wave; 3) snow plow

free expansion phase

- supernovae eject several solar masses at speeds up to $10^4\,\mathrm{km\,s^{-1}}$
- ejecta expand freely until they encounter a mass of interstellar gas comparable to their own
- at the end of free expansion the ejecta has expanded to a radius of order a few parsecs

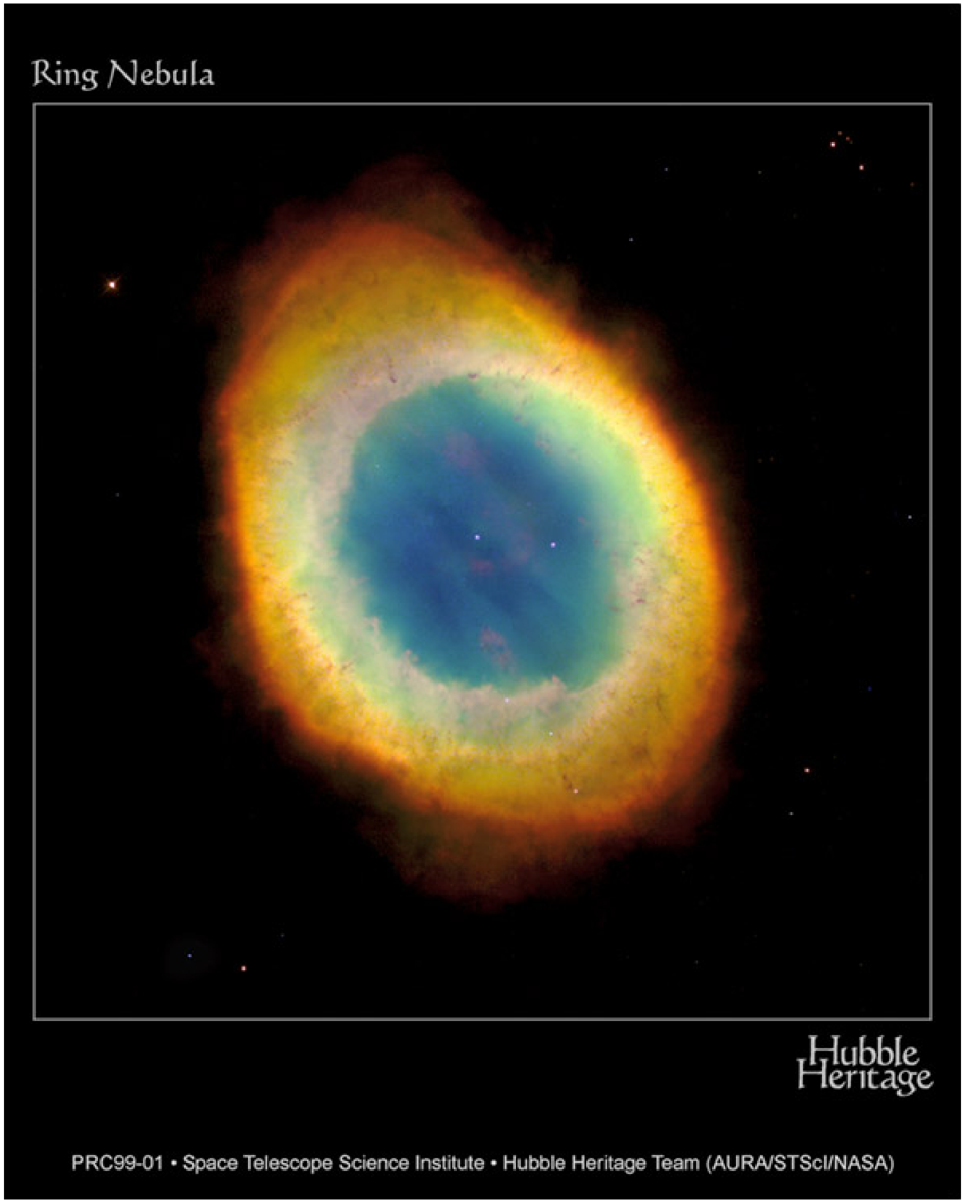

Figure 2.14: AGB wind ionized by hot white dwarf at center

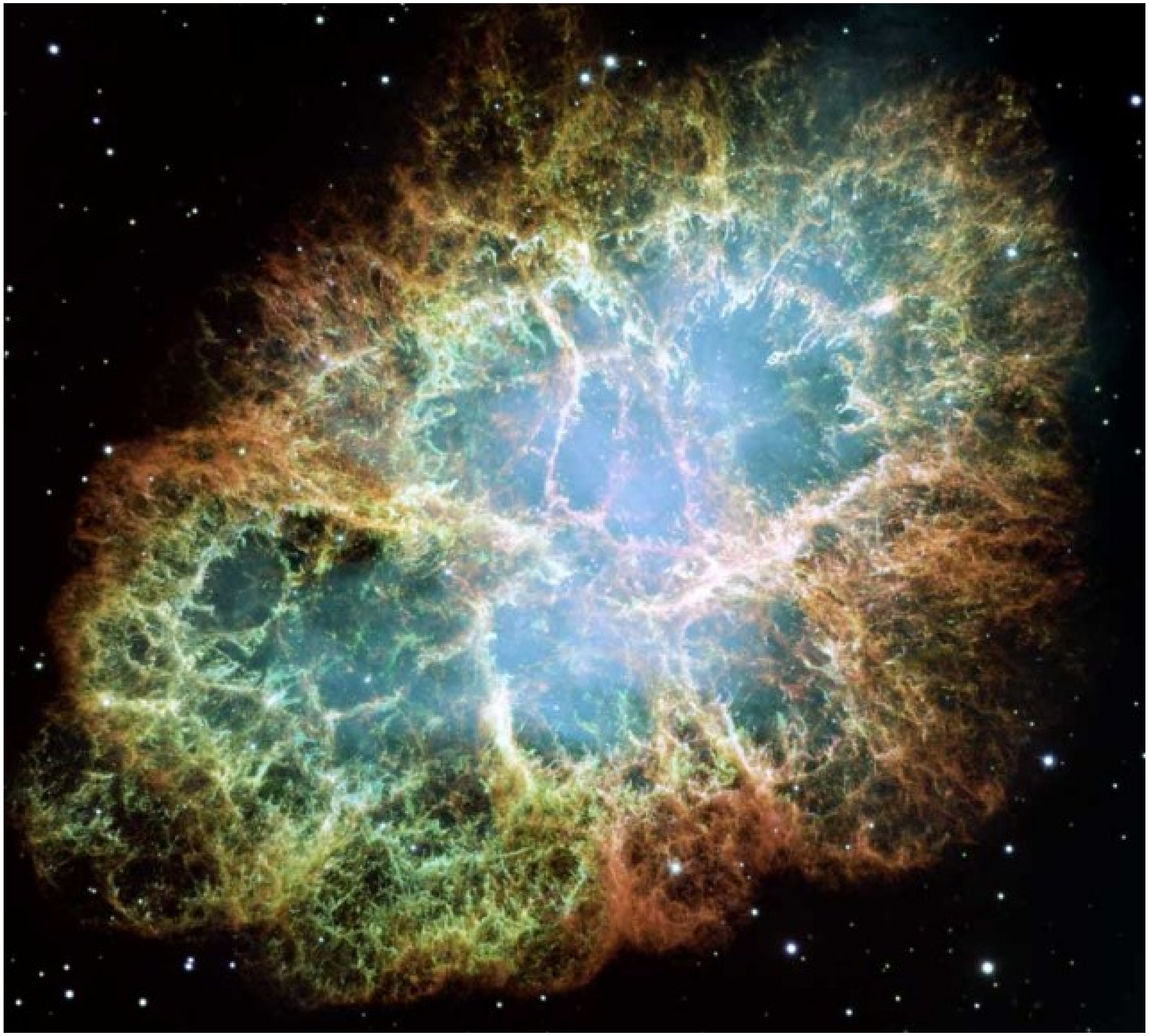

Figure 2.15: The Crab Nebula is a supernova remnant, an expanding cloud of debris from the death explosion of a massive star. Light from that stellar catastrophe was first witnessed by astronomers on planet Earth in the year 1054. Colors in the intricate filaments trace the light emitted from atoms of hydrogen, oxygen, and sulfur in the debris cloud. The erie blue interior glow is emitted by high-energy electrons accelerated by the Crab's central pulsar. One of the most exotic objects known to modern astronomers, the pulsar is a neutron star, the spinning remnant of the collapsed stellar core.

blast wave phase

- blast wave results from the deposition of a large amount of energy in a small volume
  - energy conservation phase before radiative losses become significant
- self-similar Sedov-Taylor solution describes a blast wave in a medium of uniform density

$$R_{sh} \approx \left(\frac{E}{\rho}\right)^{1/5} t^{2/5} \tag{2.31}$$

  - post-shock gas is almost isobaric
  - density drops over small fraction of radius behind the shock
- adiabatic phase ends when the post-shock gas slows sufficiently to cool by radiation

snow plow phase

- momentum per unit solid angle is conserved
- $dR/dt \propto R^{-3}$ in snow plow phase whereas $dR/dt \propto R^{-3/2}$ in blast wave phase
  - mass swept up is concentrated in a thin shell

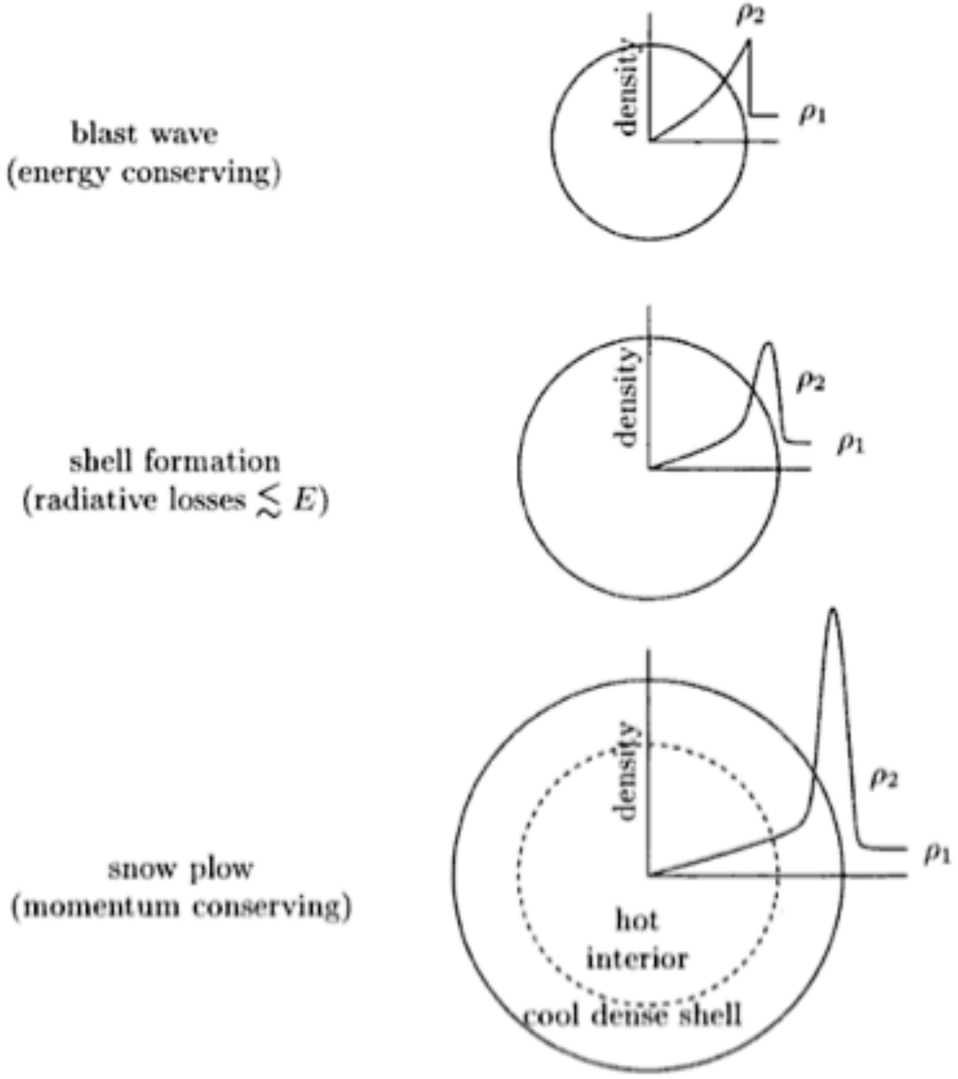

Figure 2.16: energy conserving blast wave phase & momentum conserving snowplow phase: F. Shu (1992)

Chapter 3

Disks

3.1 Why Disks?

- disks form when energy is lost while angular momentum is conserved
  - radiation from a body spinning with linear velocity $\beta \equiv v/c$ causes

$$\frac{1}{H}\frac{dH}{dt} \approx \frac{\beta^2}{E}\frac{dE}{dt} \tag{3.1}$$

- example: Poynting-Robertson drag on dust grain orbiting a star causes its orbit to decay
  - decay timescale is that at which intercepted radiation equals particle's rest mass energy

3.2 Mechanisms of Angular Momentum Transport

3.2.1 Collisional Stresses

- application to planetary rings

  - collisions yield kinematic viscosity

$$\nu \sim \frac{v^2}{\Omega}\frac{\tau}{1+\tau^2} \tag{3.2}$$

  - v is random velocity and τ is optical depth

- an unconfined ring of width Δa spreads on timescale $t_\nu \sim (\Delta a)^2/\nu$
  - spreading time for narrow rings is much shorter than age of SS
  - narrow rings are confined by shepherd satellites

3.2.2 Turbulent And Magnetic Stresses

- stresses are difficult to evaluate
  - commonly parameterized by $\sigma_{r,\phi} \sim \alpha p$
- applications
  - accretion disks due to mass transfer from a binary companion
    - around white dwarfs, neutron stars, black holes
  - feeding central black holes in AGN
  - proptostellar disks

magneto-rotational instability (MRI)

- weak magnetic fields are subject to instability
  - may promote disk dynamo
- analogy with elastic tether, $\omega^2 = k/m$

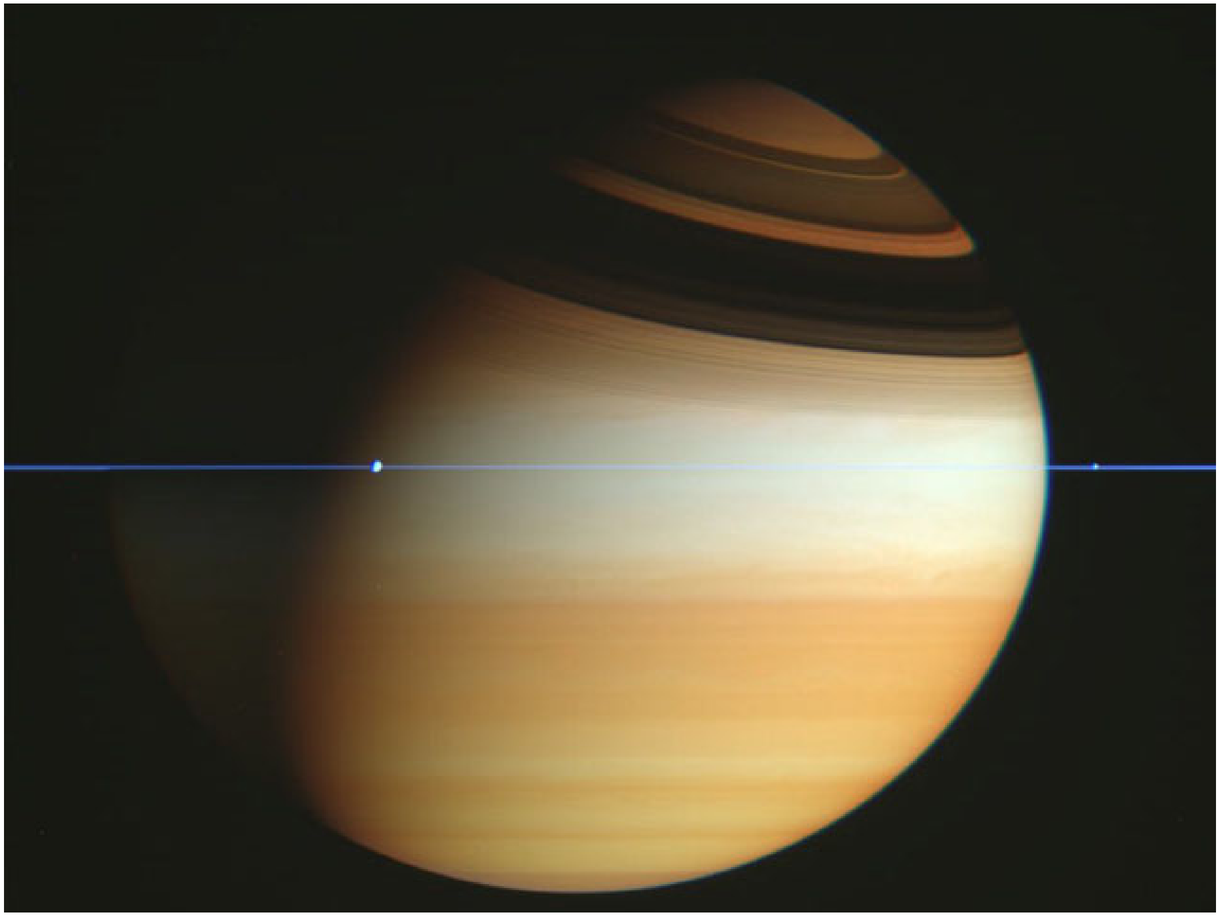

Figure 3.1: Saturn's rings are confined to a plane many times thinner, in proportion, than a razor blade. A series of plane crossing images from late February was dug out of the vast online Cassini raw image archive by interested Spanish amateur Fernando Garcia Navarro. Pictured above, digitally cropped and set in representative colors, is the striking result. Saturn's thin ring plane appears in blue, bands and clouds in Saturn's upper atmosphere appear in gold, and dark shadows of the rings curve across the top of the gas giant planet. Moons appear as bumps in the rings. Credit: Cassini Imaging Team, SSI, JPL, ESA, NASA

- equation of motion for tether in Keplerian disk

$$\frac{d^2\mathbf{r}}{dt^2} = \Omega^2(\mathbf{a}+\mathbf{r})\left(1 - \frac{a^3}{|\mathbf{a}+\mathbf{r}|^3}\right) + 2\mathbf{\Omega}\times\dot{\mathbf{r}} - \omega^2\mathbf{r} \tag{3.3}$$

  - expand for $r/a \ll 1$ and form scalar equations for $\hat{\mathbf{a}}\cdot\mathbf{r}$ and $\hat{\mathbf{\Omega}}\cdot(\hat{\mathbf{a}}\times\mathbf{r})$

- solve linear equations for dispersion relation with $\partial/\partial t = \sigma$

$$\sigma^4 + (\Omega^2 + 2\omega^2)\sigma^2 - (3\Omega^2 - \omega^2)\omega^2 = 0 \tag{3.4}$$

  - unstable mode: $\sigma > 0$, exists for $0 < \omega < \sqrt{3}\Omega$
  - maximum growth rate of $3\Omega/4$ achieved at $\omega = \sqrt{15}\Omega/4$

- incompressible MHD with initial vertical field yields same DR as tether
  - $\omega^2 = (k_z V_{\rm A})^2$ with the Alfven velocity given by $V_{\rm A}^2 = B_0^2/(4\pi\rho)$
  - in disk of finite thickness, H, minimum $k_z \sim H^{-1} \sim c_s/\Omega$
  - maximum B_0 at which instability occurs is $B_0^2/(8\pi) \sim \rho c_s^2$; equipartition
  - effective $\alpha < 1$

3.2.3 Spiral Density Waves

free waves

- density waves in a 2D isothermal, differentially rotating disk
  - solution of linearized equations of mass & momentum conservation
  - augmented by Poisson's equation if self-gravity is important

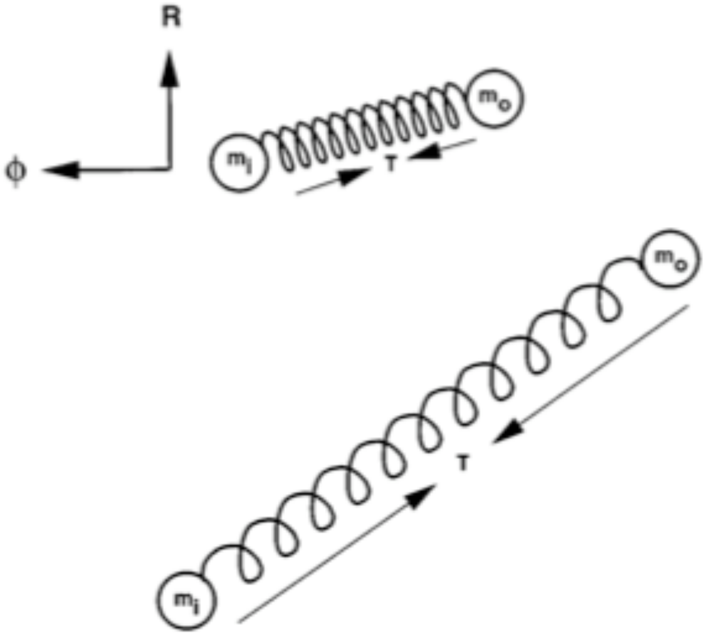

FIG. 16. Two masses in orbit connected by a weak spring. The spring exerts tension force T resulting in a transfer of angular momentum from the inner mass m_i to the outer mass m_o. If the spring is weak, the transfer results in an instability as m_i loses angular momentum, drops through more rapidly rotating inner orbits, and moves further ahead. The outer mass m_o gains angular momentum, moves through slower outer orbits, and drops further behind. The spring tension increases and the process runs away.

Figure 3.2: Balbus & Hawley: Rev. Mod. Phys. 70, 1 - 53 (1998)

- WKB solutions of form $\exp(i\Phi)$ with phase $\Phi = \int^r dr' k(r') + m\phi - \omega t$
  - axisymmetric disturbances, $m = 0$, trailing spirals, $k > 0$, leading spirals, $k < 0$
- parameters of unperturbed disk
  - surface mass density, Σ, isothermal sound speed, c_s
  - angular velocity, Ω, epicyclic frequency, $\kappa^2 = r^{-3}\partial(r^2\Omega)^2/\partial r$
- WKB dispersion relation:
$$(\omega - m\Omega)^2 = k^2c_s^2 - 2\pi G\Sigma|k| + \kappa^2 \tag{3.5}$$
  - axisymmetric disturbances are stable provided $Q \equiv \kappa c_s/(\pi G\Sigma) > 1$
  - $\partial\omega/\partial k = 0$ at $|k_c| = \pi G\Sigma/c_s^2$
  - $\omega = m\Omega_p$ where Ω_p is the pattern speed
  - group velocity:
$$v_g = \frac{\partial\omega}{\partial k} = sign(k)\left(\frac{\pi G\Sigma - |k|c_s^2}{m(\Omega - \Omega_p}\right) \tag{3.6}$$
- dependence of $|k|$ on position, $D = \kappa^2 - m^2(\Omega - \Omega_p)^2$, $\epsilon = \pm 1$
$$|k| = k_c + \epsilon\left[k_c^2 - D/c_s^2\right]^{1/2} \tag{3.7}$$
  - short waves for $\epsilon = +1$, long waves for $\epsilon = -1$
- corotation and Lindblad resonances in terms of Doppler shifted frequency, $\sigma \equiv m(\Omega_p - \Omega)$
  - $\sigma = 0$ at the corotation resonance, $\Omega = \Omega_p$
  - $\sigma = \pm\kappa$ at a Lindblad resonance, $-$ at an ILR and $+$ at an OLR
- propagation diagram: barrier around corotation for stable disk, $Q > 1$, tunneling through barrier

- spiral density waves transport angular momentum radially
  - by a combination of gravitational and advective torques
  - angular momentum luminosity is conserved
- winding problem: short leading waves to long leading waves to long trailing waves to short trailing waves
- resonant damping of short waves at Lindblad resonance in collisionless particle disk
- only short waves exist in absence of self-gravity, they do not propagate between ILR and OLR

excitation by an external potential

- external potential $\phi_m(r)\cos m(\theta - \Omega_p t)$ excites long trailing spiral density waves at ILR and OLR
- torque at these resonances is given by

$$T_m^L = -m\pi^2 \left\{ \frac{\Sigma}{dD/dr} \left[r\frac{\partial \phi_m}{\partial r} + \frac{2\Omega\phi_m}{\Omega - \Omega_p} \right]^2 \right\}_{r_L} \tag{3.8}$$

  - torque is negative at ILR and positive at OLR
  - angular momentum is transferred down angular velocity gradient
- application to planetary rings, protoplanetary disks and disk galaxies

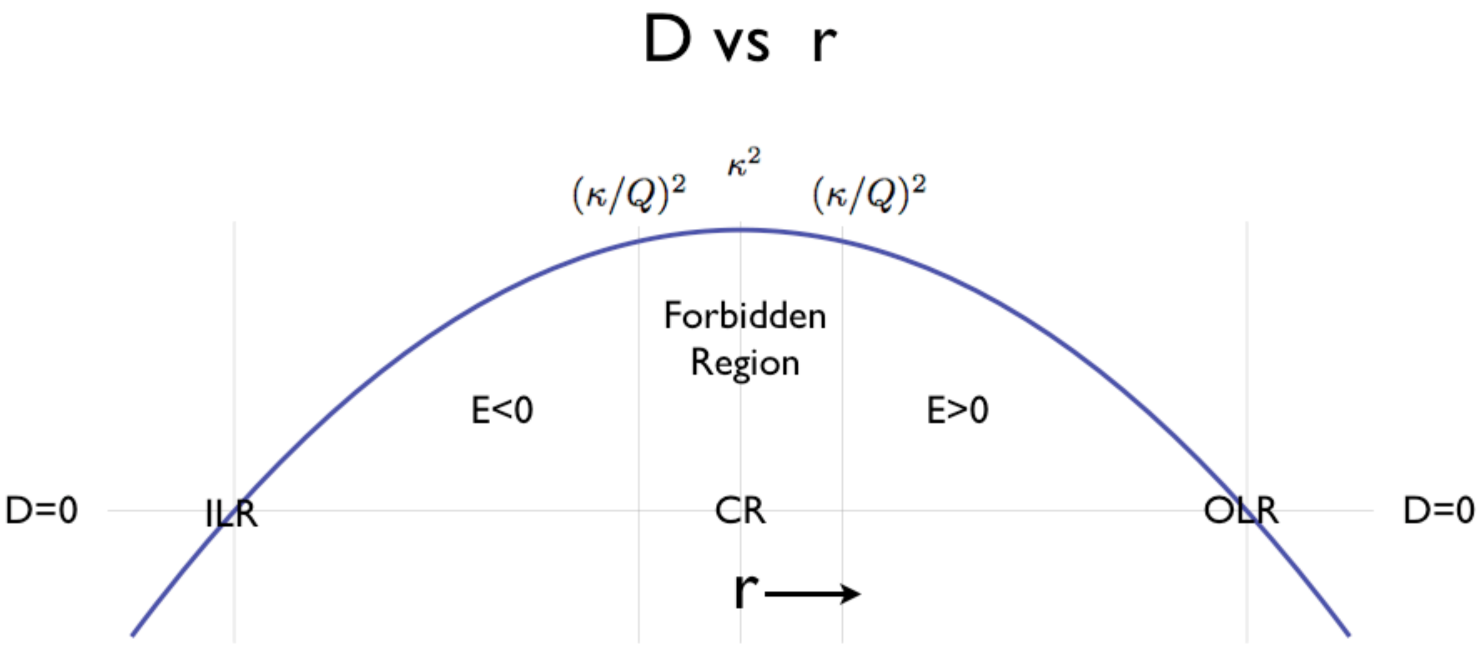

Figure 3.3: $D \equiv \kappa^2 - m^2(\Omega - \Omega_p)^2$

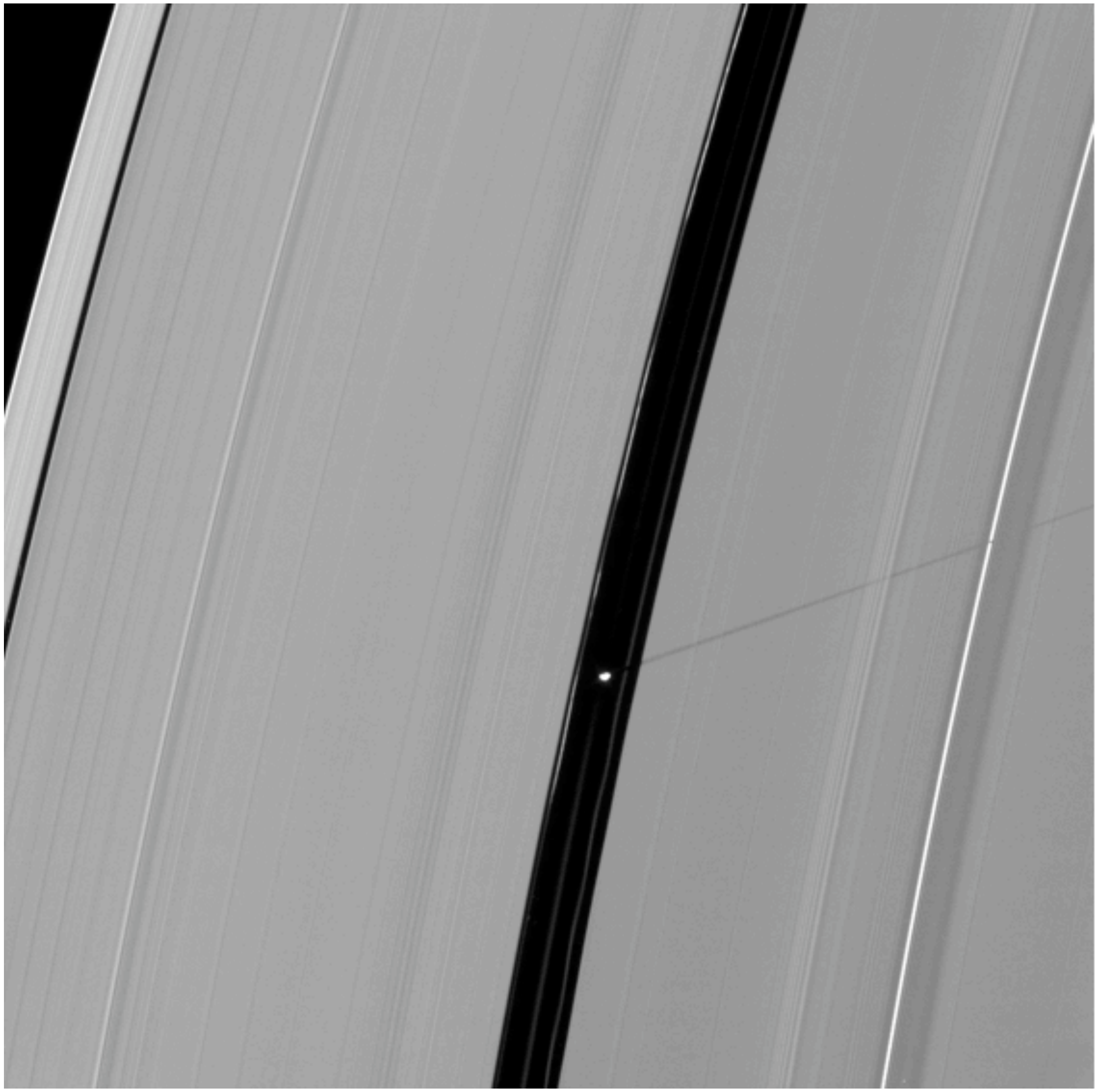

Figure 3.4: Pan, is an egg shaped body whose long axis points toward Saturn. It has a mean radius of 14 km and maintains the 325 km wide Encke Gap in Saturn's A ring. The image was taken shortly before the time of Saturn's August 2009 equinox and the low Sun angle is responsible for Pan's long shadow on the rings. Pan is named after a satyr (a creature resembling a man with the hind legs and hooves of a goat) who was a Greek god of nature and the forest. Image Credit: NASA/JPL/Space Science Institute

Figure 3.5: M51: Cosmic Whirlpool. The galaxy, has well defined spiral structure apparently excited by its companion galaxy (right). The pair are at a distance of about 10 million parsecs. Credit: S. Beckwith (STScI) Hubble Heritage Team, (STScI/AURA), ESA, NASA

viscous damping and overstability

- stresses due to particle collisions can act to damp or excite density waves in planetary rings
- analogy with stresses due to turbulent convection in stars and planets
- models of viscous stress in dense rings yield predictions of overstability
  - overstability is likely responsible for banding seen in Saturn's B-ring
  - observed modes of narrow Uranian rings with $m = 0, 1, 2$ are probably linearly overstable

global modes and swing amplifier

- corotation amplifier: coupling of negative and positive action waves across forbidden region
- an example of a negative energy wave
  - surface gravity wave propagating upstream less rapidly than water flows downstream
  - excited by air drag
- swing amplifier in marginally stable disks yields large amplification
- global modes need feedback
  - reflection from small r regenerates short leading waves from short trailing ones
  - in stellar disks, feedback must occur before short trailing waves reach absorbing ILR

3.2.4 Tides

basic mechanism

- tide raising potential of quadrupole form

  - magnitude $U \sim GmR^2/a^3$
    - primary mass M and radius R; secondary mass m; orbital radius a
  - two tidal bulges
  - tidal potential at Earth due to Moon and Sun proportional to bodies $\overline{\rho}$

- tidal height on fluid bodies $\xi \sim U/g$
  - g is gravitational acceleration at surface of primary

- ξ reduced in solid bodies by elastic restoring force
  - reduction factor for uniform incompressible body is $(1 + 19\mu/2g\rho R)^{-1}$ where μ denotes rigidity

- shallow oceans complicate tides on Earth
  - velocity of shallow water waves, $v = (gh)^{1/2}$, is comparable to speed of tidal bulge
  - possibility of resonance

- tidal torque requires dissipation of tidal energy, associated with time lag of tide
  - on Earth, most of the tidal dissipation occurs in the oceans
  - dissipation due to skin friction at bottom of shallow seas
  - perhaps also by excitation of internal gravity waves in deep ocean

- torque on satellite due to tides it raises on planet, subscripts p and s refer to planet and satellite

$$T = \frac{3}{2}\frac{kGM_s^2R_p^5}{a^6Q} \tag{3.9}$$

  - Love number, k, accounts for elasticity and self-gravity of planet
  - $k \approx 0.3$ for Earth and $k \approx 0.02$ for Moon

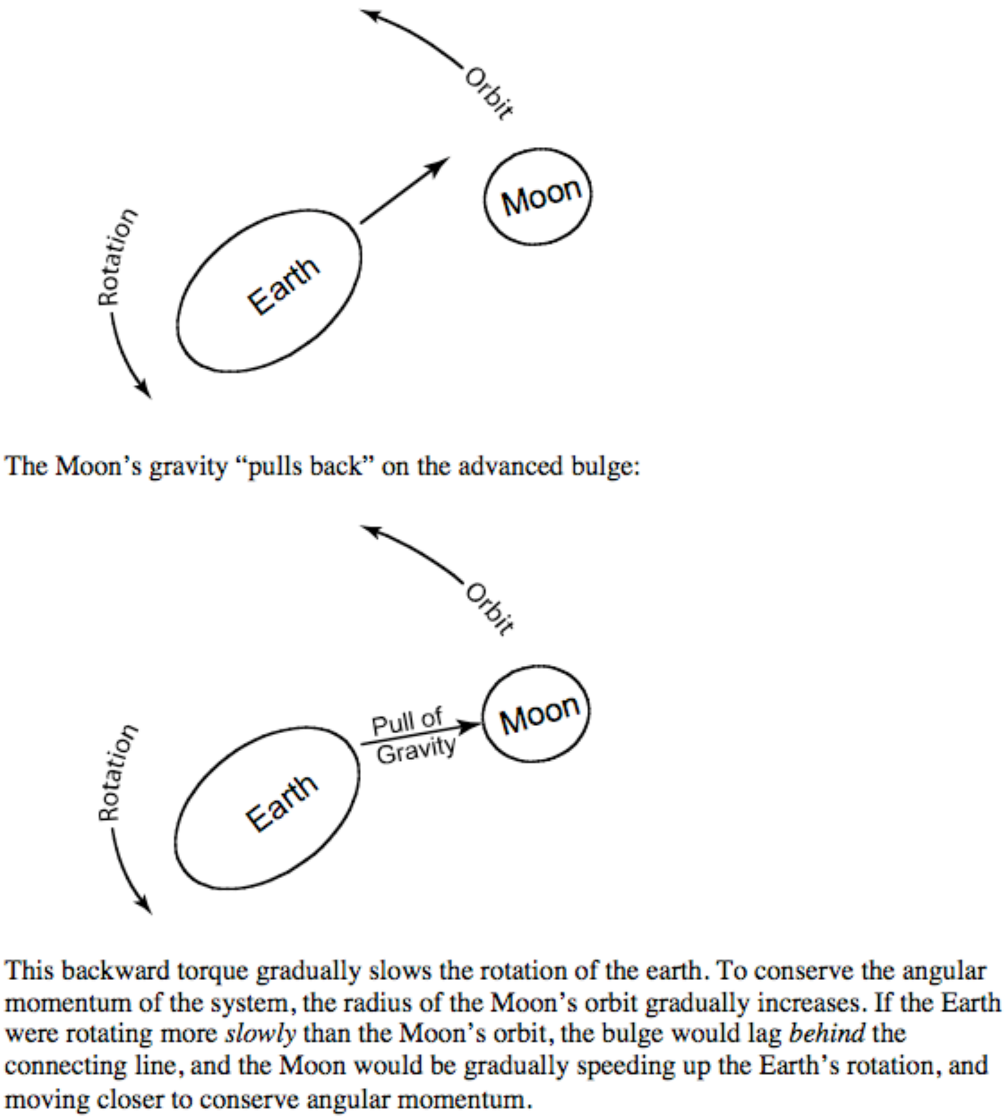

The Moon's gravity "pulls back" on the advanced bulge:

This backward torque gradually slows the rotation of the earth. To conserve the angular momentum of the system, the radius of the Moon's orbit gradually increases. If the Earth were rotating more *slowly* than the Moon's orbit, the bulge would lag *behind* the connecting line, and the Moon would be gradually speeding up the Earth's rotation, and moving closer to conserve angular momentum.

Figure 3.6:

  - quality factor, Q, describes dissipation, tidal lag angle, δ, related to Q by $\delta \approx 1/2Q$

tidal evolution in solar system

- tide raised on satellite by planet
  - despins satellite toward synchronous rotation, significant for many close satellites
    - Iapetus is marginal case
  - damps satellite's orbital eccentricity, crucial for origin of Triton's circular, inclined orbit
    - likely important for circularizing orbits of close satellites around large planets
  - tidally heats satellite, especially if orbit-orbit resonances pump up eccentricity
    - important for Io and maybe for several additional satellites
- tide raised on planet by satellite
  - increases satellite's semi-major axis and decreases planet's spin rate if $\omega > n$ and $n > 0$
  - secular increase in semi-major axis directly observed for Moon
  - $n > \omega$ for Phobos, observations show $\dot{a} < 0$
  - responsible for satellite orbit-orbit resonances
  - increases satellite's orbital eccentricity if $\omega \gg n$ and $n > 0$, may be significant for Moon
- tide raised by Sun on planet
  - despins planet toward synchronous rotation
  - essential to formation of Mercury's spin-orbit resonance
  - may have been important in despinning Venus
  - less effective than lunar tide in despinning Earth

- tidal Q
  - $Q \sim 10^2$ for solid bodies, insensitive to frequency, not well understood
    - application to terrestrial planet interiors and all satellites
  - $Q \sim 10^5$ for gaseous planets, mechanism poorly understood
    - may involve excitation of inertial waves
    - application to gas and ice giant planets including exoplanets.
  - $Q \approx 13$ for Earth due to dissipation in oceans
    - probably most due to boundary layer dissipation in shallow seas
    - perhaps some due to excitation of internal waves
- Resonances Promoted By Tides
  - spin-orbit resonance of Mercury, $\omega = 3n/2$
    - crucial role of orbital e
    - stabilized by permanent bulge, $(B - A)/C$
    - tidal spin-down and capture probability
  - orbit-orbit resonance among satellites
    - Laplace relation involving Io, Europa, and Ganymede, $2n_1 - 3n_2 + n_3 = 0$
    - resonances between pairs of Saturnian satellites
    - resonances among pairs of extrasolar planets

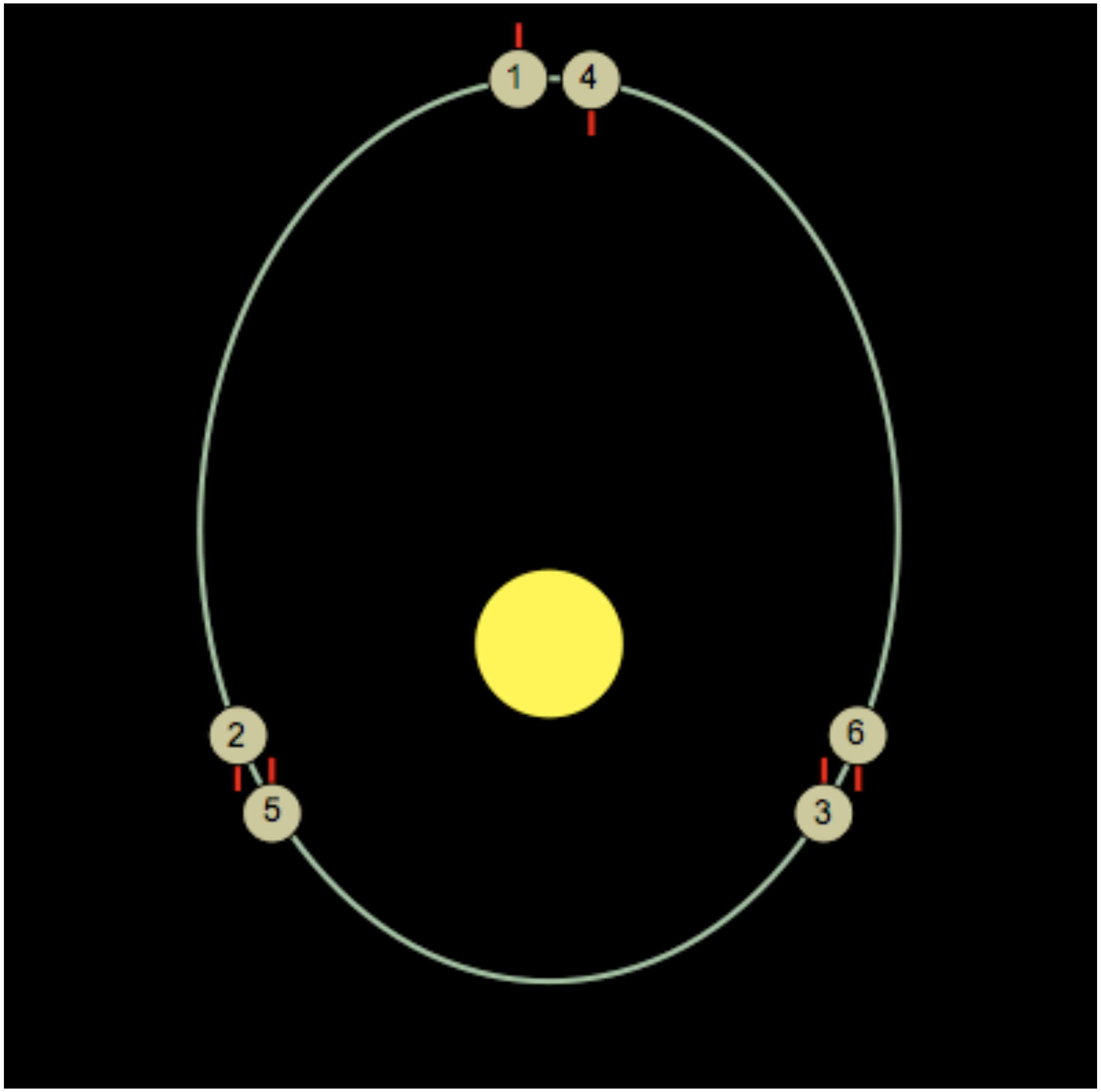

Figure 3.7: Diagram showing how Mercury's orbital period and rotational period are locked in a 3:2 resonance. Original author: Worldtraveller

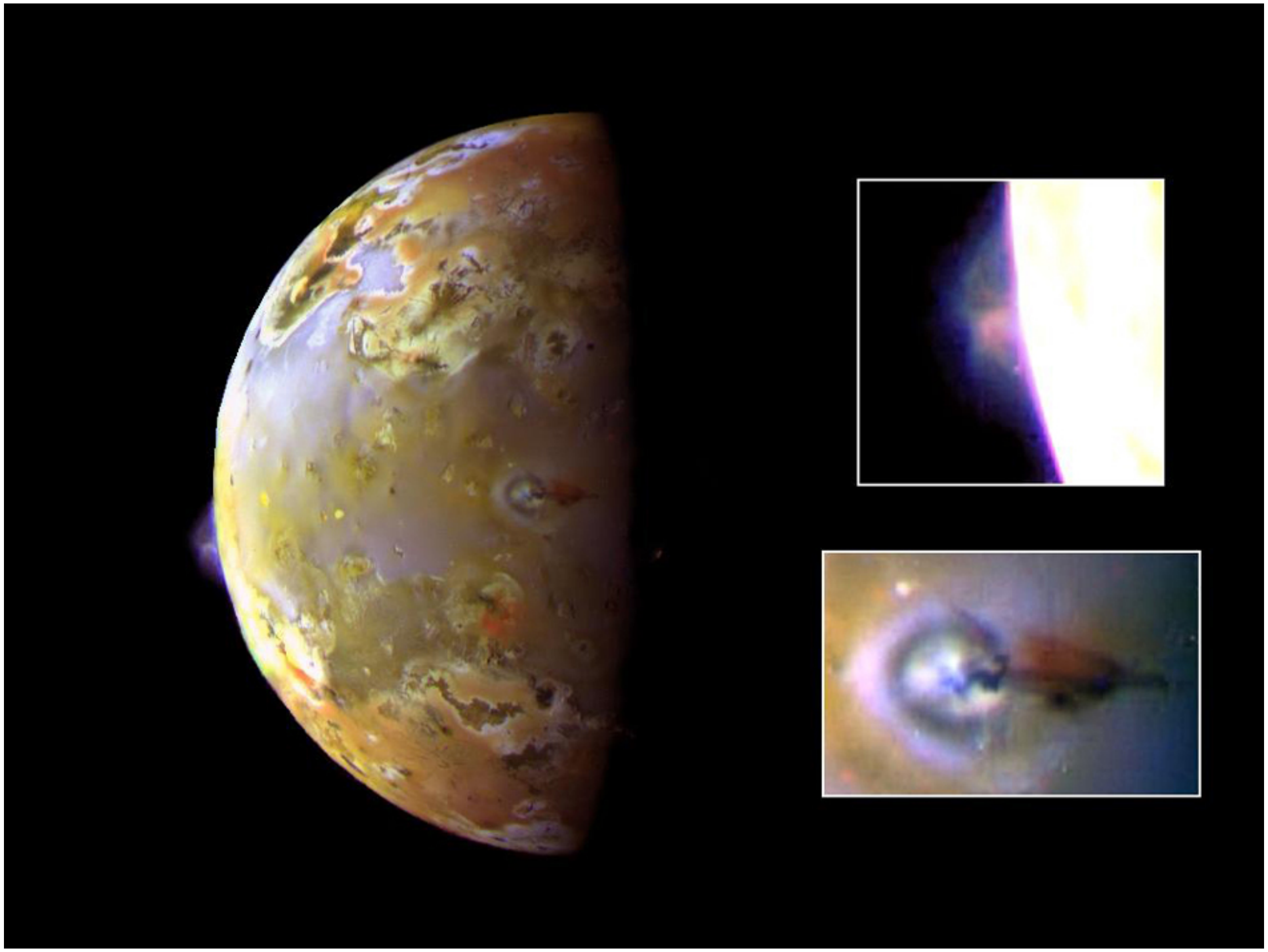

Figure 3.8: Two sulfurous eruptions are visible on Jupiter's volcanic moon Io in this color composite image from the robotic Galileo spacecraft. At the top, over Io's limb, a bluish plume rises about 140 kilometers above the surface of a volcanic caldera known as Pillan Patera. In the image middle, near the night/day shadow line, the ring shaped Prometheus plume is seen rising about 75 kilometers, or about 46 miles, above Io while casting a shadow below the volcanic vent. Credit: NASA/JPL

Chapter 4

Magnetic Fields

4.1 Dynamos

4.1.1 Observational Evidence from Solar System Bodies

- Sun
  - 22 y magnetic cycle
  - polar dipole, mean strength $1-2\,\mathrm{G}$, reverses every 11 y
  - surface field is concentrated in flux tubes, $B \approx 1.5 \times 10^3\,\mathrm{G}$
  - sunspot fields up to $3 \times 10^3\,\mathrm{G}$
- Earth
  - external field is approximately a spin aligned dipole
  - inclination $+11.3\,\mathrm{deg}$, sign convention + for Earth
  - mean equatorial field strength, $B_0 \approx 0.31\,\mathrm{G}$

  - field reverses at irregular intervals in range $10^5 - 10^7$ y

- magnetic fields have also been detected on:
  - Mercury, $B_0 \approx 4 \times 10^{-3}$ G
  - Jupiter, $B_0 \approx 4.3$ G
    - dipole axis inclined by about -9.6 deg from spin axis
  - Jupiter's satellite Ganymede, $B_0 \approx 7 \times 10^{-3}$ G
  - Saturn, $B_0 \approx 0.22$ G
    - axisymmetric to observational accuracy, inclination less than 0.5 deg
    - substantial contributions from higher axisymmetric multipoles
  - Uranus, $B_0 \approx 0.23$ G
    - dipole axis inclined by about -59 deg from spin axis
  - Neptune, $B_0 \approx 0.14$ G,
    - dipole axis inclined by about -47 deg from spin axis
- dipole magnetic fields have not been detected on:
  - Venus, $B_0 \leq 10^{-4}$ G
  - Mars, $B_0 \leq 10^{-3}$ G
  - Moon, $B_0 \leq 10^{-5}$ G

4.1.2 General Principles

- persistence of large-scale magnetic fields is due to absence of free magnetic charges
  - large-scale electric fields are shorted out

- electric currents are the sources for magnetic fields
  - ferromagnetism is a consequence of alignment of microscopic currents
    - microscopic currents do not dissipate
  - T in planetary interiors is above the Curie point of ferromagnetic materials
    - planetary magnetic fields are not due to ferromagnetism
- planetary magnetic fields are due to macroscopic currents
  - macroscopic currents decay as the result of ohmic losses
  - decay times are shorter than age of the solar system for all planets and satellites
- planetary magnetic fields require a continuous energy input
- kinetic dynamo equation is obtained by combining Maxwell's equations with Ohm's law

$$\frac{\partial \mathbf{B}}{\partial t} = \boldsymbol{\nabla} \times (\mathbf{v} \times \mathbf{B}) + \frac{c^2}{4\pi\sigma} \nabla^2 \mathbf{B} \tag{4.1}$$

- $\nabla^2 \mathbf{B}$ term describes ohmic decay
  - field lines diffuse relative to fluid with diffusivity $\lambda = c^2/(4\pi\sigma)$
  - ohmic decay time on scale L is $\tau \approx L^2/\lambda$
    - $\lambda \approx 2 \times 10^4 \, \mathrm{cm}^2 \, \mathrm{s}^{-1}$ for iron in lab or Earth's core
    - $\lambda \approx 4 \times 10^2 \, \mathrm{cm}^2 \, \mathrm{s}^{-1}$ for metallic hydrogen or copper at room T
- $\boldsymbol{\nabla} \times (\mathbf{v} \times \mathbf{B})$ term describes influence of fluid motion on field
  - $\mathbf{v}$ is specified in a kinematic dynamo
  - field lines are frozen into fluid if $\sigma = \infty$

    - magnetic flux linking any circuit of fluid particles is conserved
  - field evolution is conveniently described in terms of motion of field lines
  - velocity field can increase magnetic energy via field line stretching

4.1.3 Evidence for Dynamos

- $\tau \sim 10^{10}\,\mathrm{y}$ for the solar dipole but dipole reverses every 11 y
- $\tau \sim 3 \times 10^4\,\mathrm{y}$ for terrestrial dipole but dipole field has existed for $> 10^9\,\mathrm{y}$
- magnetic Reynolds number, $R_M \equiv vL/\lambda$ measures ratio of dynamic to dissipative terms in $\partial \mathbf{B}/\partial t$
- motions might be able maintain field against ohmic decay for $R_M > 1$
- $R_M \approx 10^4 (v/\,\mathrm{cm\,s^{-1}})$ in Earth's core
  - convective velocity in core, $v \sim 10^{-2}\,\mathrm{cm\,s^{-1}}$, adequate for dynamo
- disk dynamo: depending on topology of current loop can get dynamo or anti-dynamo
  - illustration depicts dynamo

4.1.4 Solar Dynamo

- observations
  - periodic magnetic field, 22 y cycle, weak polar dipole field reverses every 11 y
  - field dominated by active regions below 55 deg latitude
    - photospheric field concentrated in flux tubes, $B \approx 1.5 \times 10^3\,\mathrm{G}$
  - sunspots found in bipolar groups, $T_{\rm spot} \approx 4 \times 10^3\,\mathrm{K}$, $T_{\rm photo} \approx 5.6 \times 10^3\,\mathrm{K}$

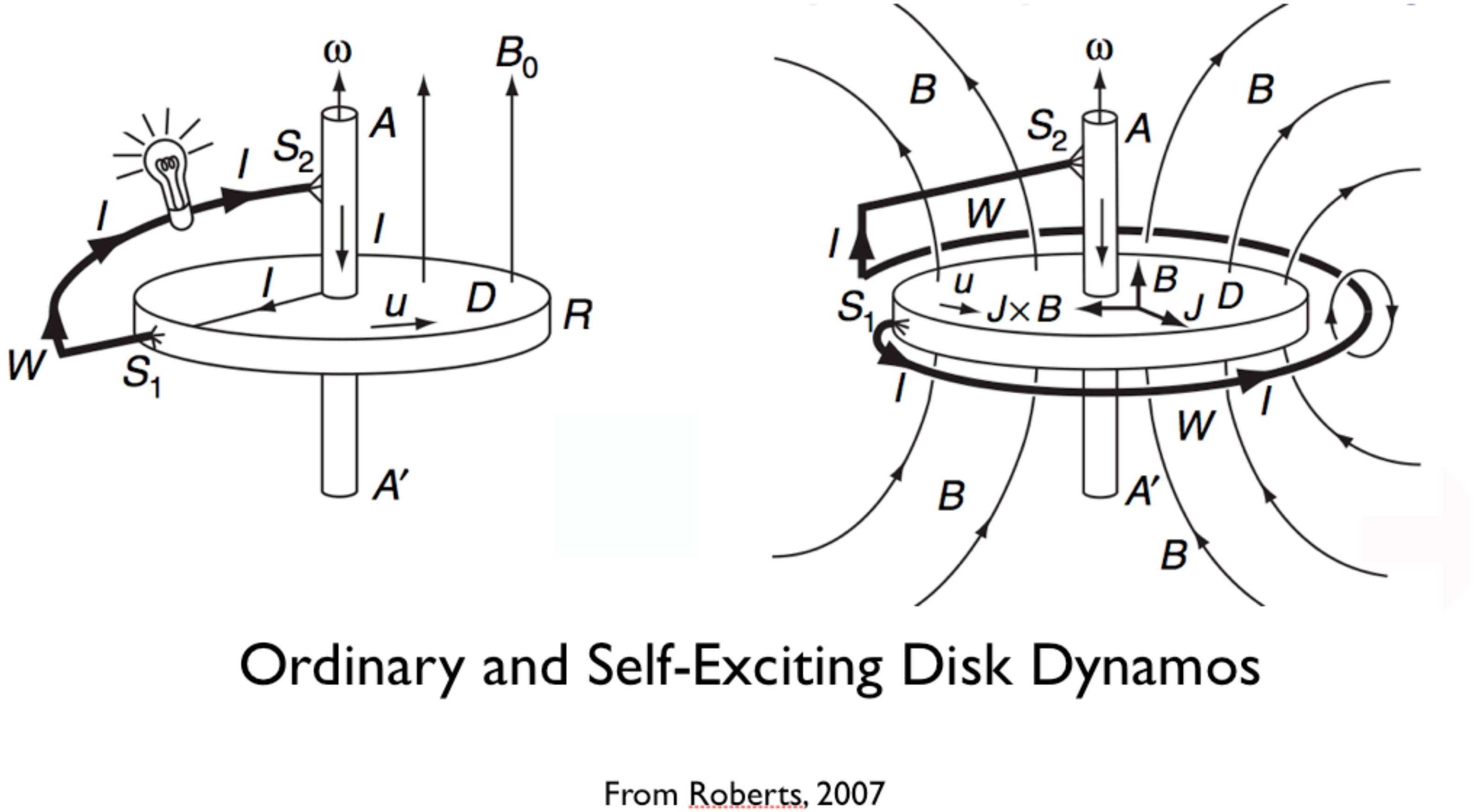

Ordinary and Self-Exciting Disk Dynamos

From Roberts, 2007

Figure 4.1:

    - $\sigma T_{\rm spot}^4 \approx 0.25 \sigma T_{\rm photo}^4$, spots appear dark
  - p-spots appear at lower latitudes than f-spots, tilt angle of axis about 5 deg

- evolution through cycle
  - sun is generally free of spots at beginning of cycle,
  - new spots appear in band centered around latitude 40 deg
  - polarity of p-spots is that of polar field at beginning of cycle
  - individual spots last several days to a few months
  - active regions move closer to equator as cycle progresses
  - polar field reverses about the time of sunspot maximum

Models

- differential rotation in the solar convection zone (CVZ) plays a crucial role
  - differential rotation arises from interaction between Coriolis acceleration and convection
    - rotation period at photosphere increases by about 30% from equator to poles
  - helioseismology has revealed rotation throughout most of sun
    - angular velocity, $\Omega(r, \theta)$, is approximately constant on radial lines in convection zone
    - Ω is constant in radiative zone (RZ) below convective envelope
- differential rotation produces B_ϕ from B_p
  - toroidal flux tubes float to surface to produce bipolar active regions
    - magnetic fields are buoyant, they have pressure but no mass
  - Ω increases along field lines toward equator

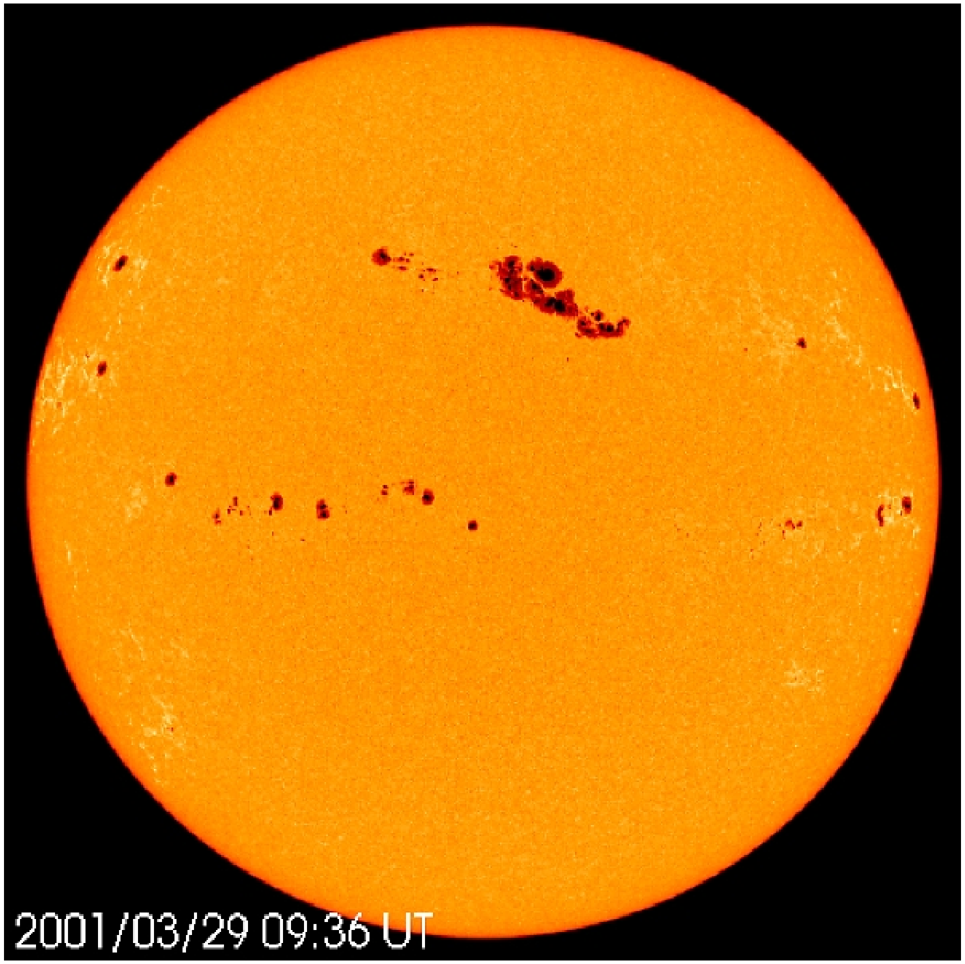

Figure 4.2: Sunspot area within the group spanned is more than 13 times the entire surface of the Earth! It was the source of numerous flares and coronal mass ejections. Caused by intense magnetic fields emerging from the interior, a sunspot appears to be dark only when contrasted against the rest of the solar surface, because it is slightly cooler than the unmarked regions. Credit: NASA/SOHO.ESA

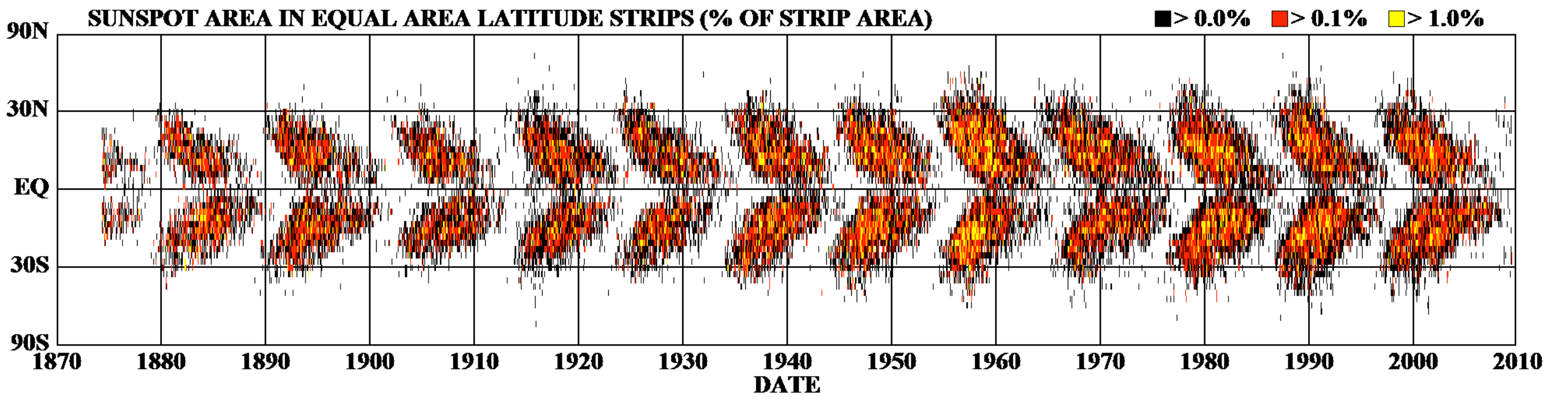

Figure 4.3: Sunspot Butterfly diagram. Credit: David Hathaway, NASA Marshall Space Flight Center

    - ∗ accounts for relation between polarity of bipolar spot groups and polar field

- helicity of turbulent convection tilts active regions as they rise
  - produces B_p from B_ϕ
  - dipole moments of bipolar regions oppose that of polar field,
    - ∗ leads to a periodic dynamo

4.1.5 Record Of Past Solar Activity

- C^{14}: half-life $5,568\,\mathrm{y}$
  - production: $\mathrm{n} + \mathrm{N}^{14} \rightarrow \mathrm{C}^{14} + \mathrm{H}$
  - peaks between $10 - 15\,\mathrm{km}$ altitude, rate about $2\,\mathrm{cm}^{-2}\,\mathrm{s}^{-1}$
  - neutrons produced by collisions of galactic cosmic rays with atmospheric molecules

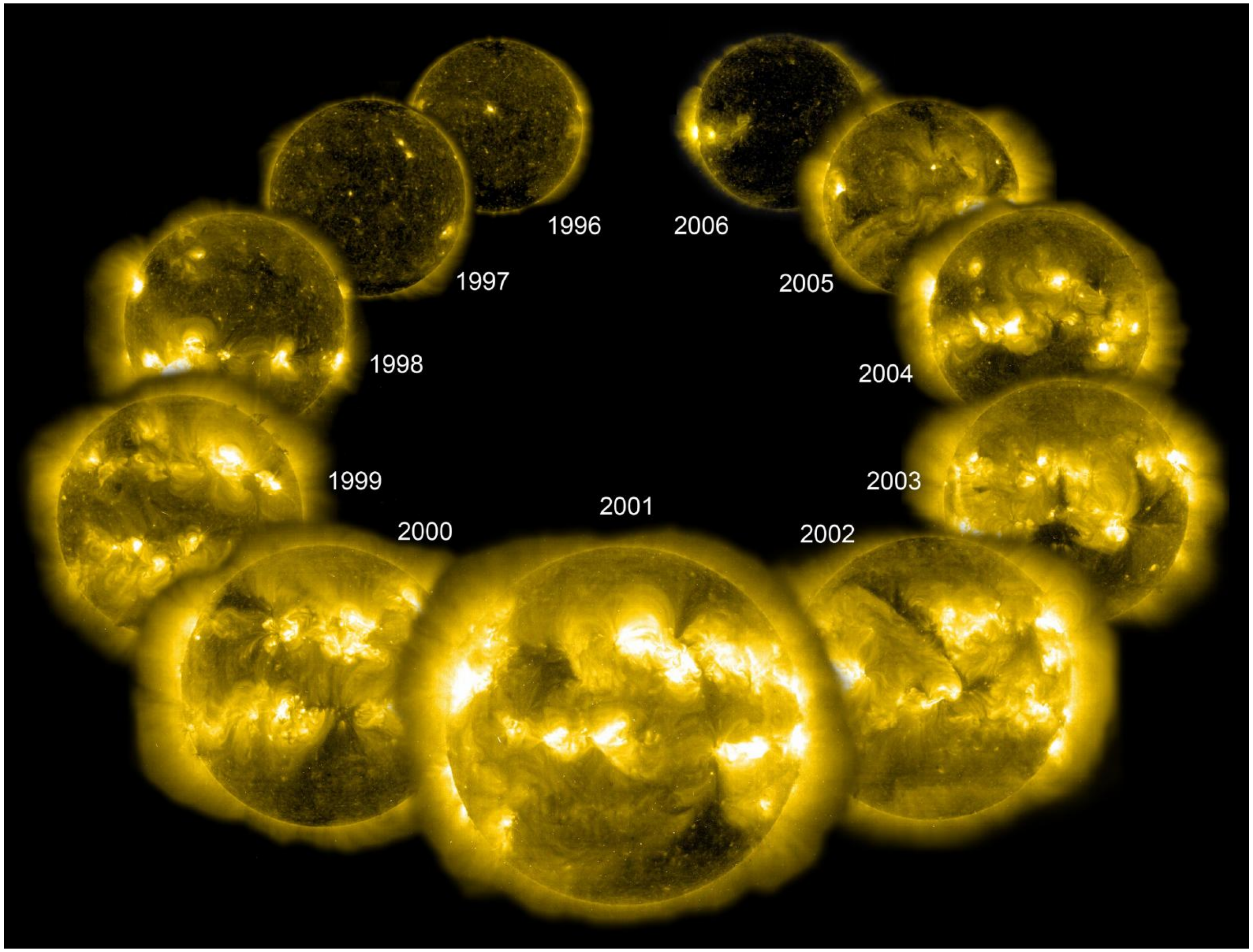

Figure 4.4: An EIT image in the Fe XV 284 Angstrom wavelength of extreme UV light from each year of nearly an entire solar cycle. Credit: NASA/SOHO.ESA

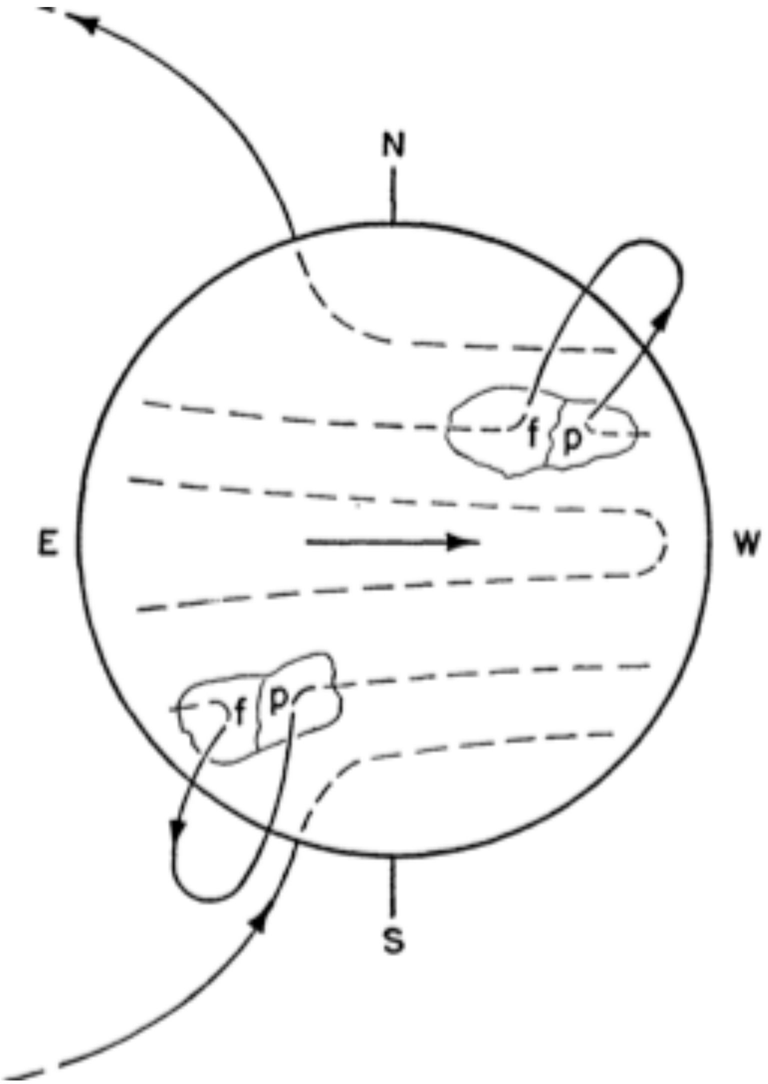

Figure 4.5: Bipolar magnetic regions (BMR's) are formed where buoyant flux loops of submerged toroidal field are brought to the surface. The BMR's continue to expand and the flux loops rise higher into the corona: credit Babcock (1961) ApJ

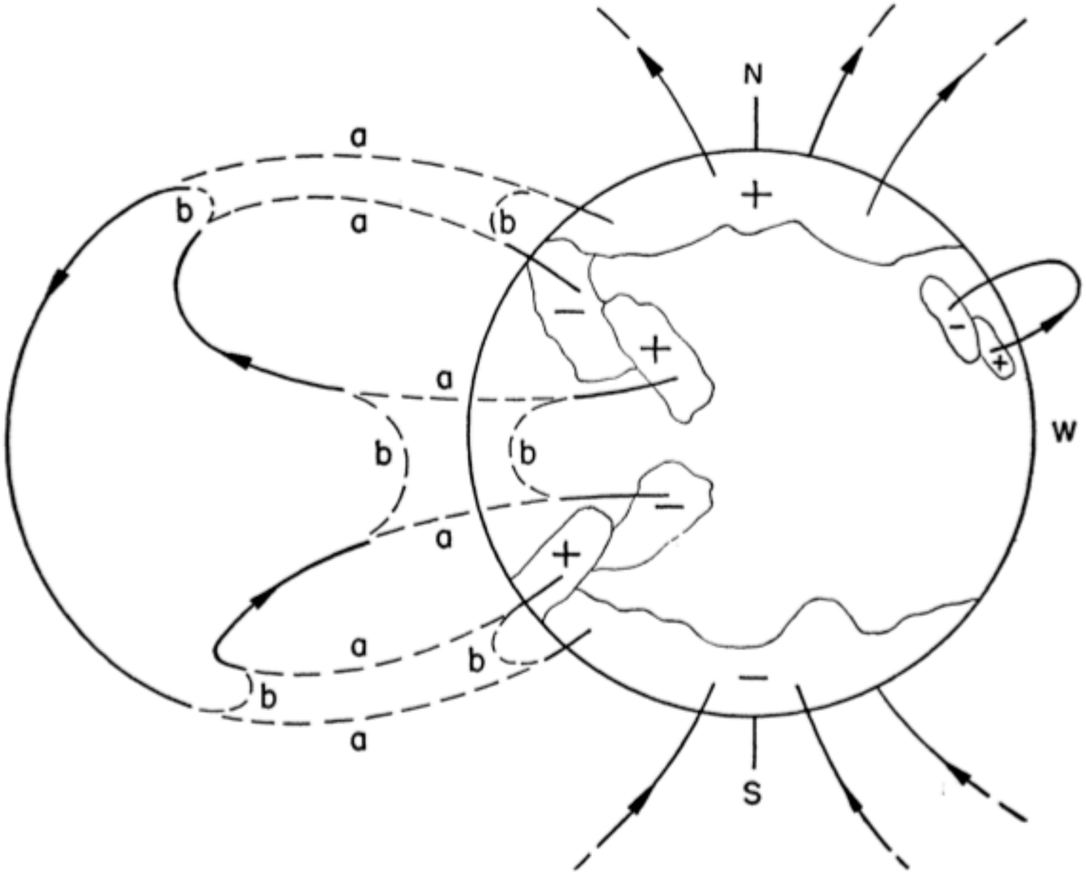

Figure 4.6: The expanding field lines above the older BMR's reconnect with those of the main dipole field liberating large loops of low intensity field. Continuation of this process results in the formation of a new main dipole field of reversed polarity. Babcock (1961) ApJ

  - C^{14} incorporated into living organisms, decays after they die
- solar wind B field shields Earth from low energy galactic cosmic rays
  - production rate of C^{14} decreases during solar maximum
  - C^{14} in tree rings records solar activity over thousands of years, resolution $10 - 20\,\mathrm{y}$
  - Maunder minimum: $1645 - 1715$, little ice age, spots very rare on sun, identified in C^{14} record

4.2 Magnetospheres

4.2.1 Definitions

- magnetosphere, region of dominance of the planetary magnetic field
  - compressed toward sun, stretched away from it
  - confined on front by solar wind bow shock, collisionless, but still real
- magnetosheath, shocked solar wind plasma streaming around magnetosphere
- magnetopause, boundary within which planetary field lines are confined
- magnetotail, planetary field lines stretched downwind
- aurora
  - precipitation of energetic charged particles
  - acceleration results from field line reconnection in magnetotail

4.2.2 Size Of Magnetosphere

- balance solar wind ram pressure and magnetic pressure of planet's field
  - ram pressure in solar wind, $p = \rho v^2 \approx 10^{-8}(\,\mathrm{AU}/a)^2\,\mathrm{dyne\,cm^{-2}}$
  - pressure of planet's magnetic field, $p = B^2/8\pi$, $B = B_0(R/r)^3$ for dipole field
  - pressure balance yields
$$\frac{r}{R} \approx 13 \left(\frac{B_0}{\mathrm{G}}\frac{a}{\mathrm{AU}}\right)^{1/3} \tag{4.2}$$
  - for Earth, $B_0 \approx 0.3\,\mathrm{G}$, $a = \,\mathrm{AU}$, $r/R \approx 9$
  - for Jupiter, $B_0 \approx 10\,\mathrm{G}$, $a \approx 5\,\mathrm{AU}$, $r/R \approx 50$

4.2.3 Particle Motion

- corotating plasma
  - ionosphere is an equipotential in frame rotating with angular velocity $\mathbf{\Omega}$
  - $\mathbf{E}\cdot\mathbf{B} = 0$ implies $\mathbf{E} + (\mathbf{\Omega}\times\mathbf{r})\times\mathbf{B} = \mathbf{0}$ in magnetosphere
  - plasma drifts at velocity $\mathbf{v}_d = c(\mathbf{E}\times\mathbf{B})/B^2 = \mathbf{\Omega}\times\mathbf{r}$
  - corotation $\mathbf{E}$ sourced by charge density $-\mathbf{\Omega}\cdot\mathbf{B}/(2\pi c)$
  - evidence for corotation of Earth, Jupiter & Saturn magnetospheres
- trapped particles
  - adiabatic invariants
- field line interchange
  - driven by mass loading in magnetosphere

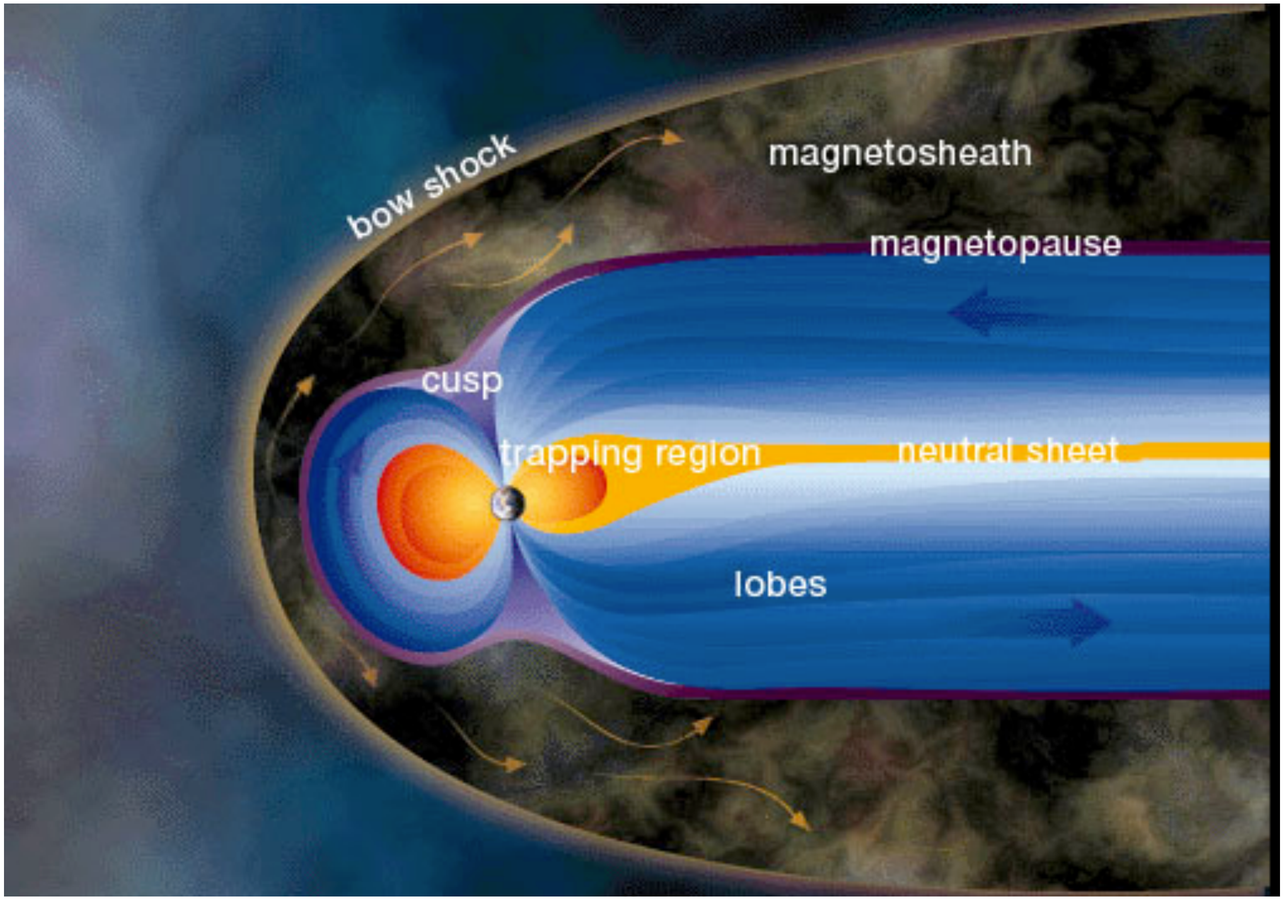

Figure 4.7: Drawing of Earth's magnetosphere. Notice that the magnetic field is much larger than the planet. credit: Windows to the Universe

  - enables plasma to move outward and escape
  - drag due to finite resistivity of ionosphere

4.2.4 Jovian Magnetosphere

- revealed by radio astronomy starting in 1950's
  - decametric bursts at cyclotron frequency yield field strength
    - Io, a Jovian unipolar inductor, Bigg's story
  - decimetric synchrotron radiation from trapped, relativistic electrons
    - rocking of linear polarization yields dipole inclination of about 10 deg
    - circular polarization shows polarity is opposite to that of Earth's field
  - mass loss associated with volcanoes on Io
    - corotating torus of plasma around Io's orbit
    - heating by pickup ions
    - centrifugally driven outward flow leading to mass loss to solar wind

4.3 Force Free Electrodynamics

4.3.1 Description

- applies where the energy density of the plasma is much smaller than that of the electromagnetic field
- **E** and **B** are the fundamental variables in FFE
- plasma velocity and charge density are obtained from **E** and **B**

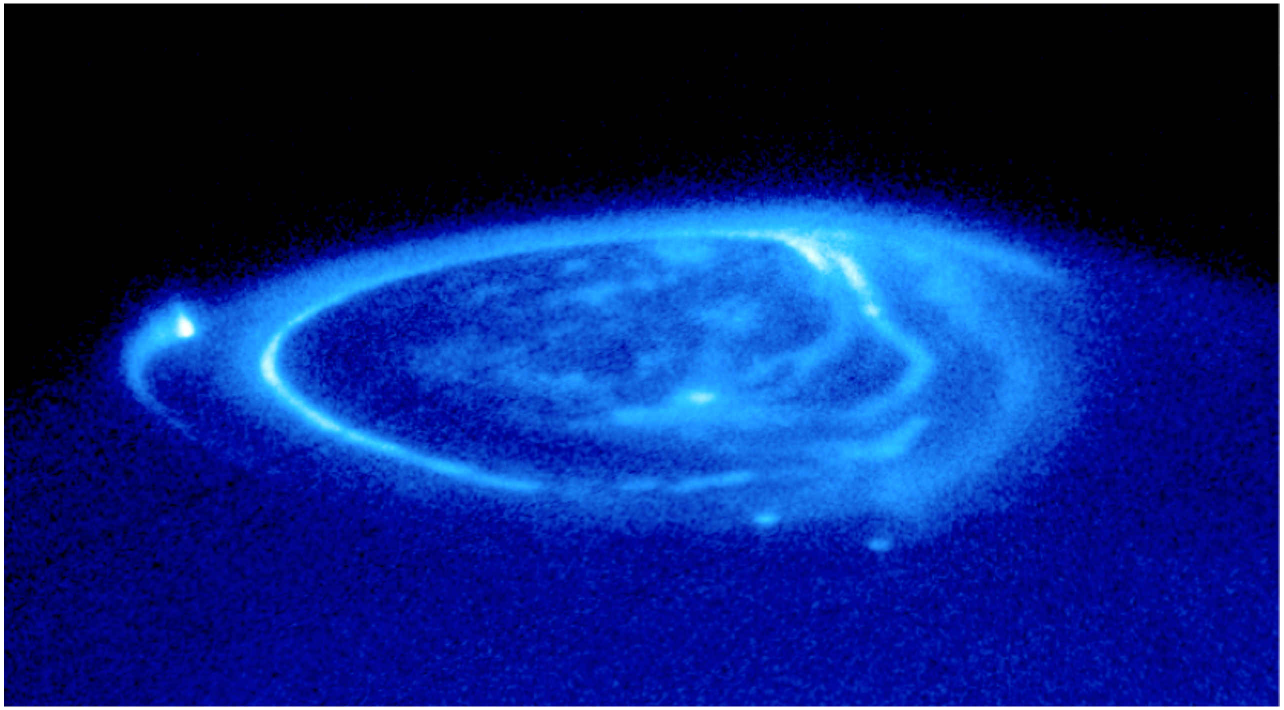

Figure 4.8: Aurora borealis on Jupiter. Three bright dots are created by magnetic flux tubes that connect to the Jovian moons Io (on the left), Ganymede (on the bottom) and Europa (also on the bottom). In addition, the very bright almost circular region, called the main oval, and the fainter polar aurora can be seen. Credit: John T. Clarke (U. Michigan), NASA image in UV, Hubble Space Telescope

4.3.2 Equations

- FFE is governed by the equations

$$\frac{1}{c}\frac{\partial \mathbf{E}}{\partial t} = \boldsymbol{\nabla} \times \mathbf{B} - \frac{4\pi \mathbf{j}}{c} \tag{4.3}$$

$$\frac{1}{c}\frac{\partial \mathbf{B}}{\partial t} = -\boldsymbol{\nabla} \times \mathbf{E} \tag{4.4}$$

- charge density ρ is obtained from

$$\rho = \frac{\boldsymbol{\nabla} \cdot \mathbf{E}}{4\pi} \tag{4.5}$$

- current density $\mathbf{j}$ is given by

$$\frac{\mathbf{j}}{c} = \frac{\left[\mathbf{B} \cdot (\boldsymbol{\nabla} \times \mathbf{B}) - \mathbf{E} \cdot (\boldsymbol{\nabla} \times \mathbf{E})\right] \mathbf{B} + (\boldsymbol{\nabla} \cdot \mathbf{E})(\mathbf{E} \times \mathbf{B})}{4\pi B^2} \tag{4.6}$$

- $\boldsymbol{\nabla} \cdot \mathbf{B} = 0$ and $\mathbf{E} \cdot \mathbf{B} = 0$ are imposed as initial conditions and maintained by equations (4.3) & (4.4)

- FFE conserves electromagnetic energy: $\mathbf{j} \cdot \mathbf{E} = 0$

- $\mathbf{j}_\perp$ is due to $\mathbf{E} \times \mathbf{B}$ drift of charge density
  - vanishing of the Lorentz force implies

$$\mathbf{E} \cdot \mathbf{B} = 0 \quad \text{and} \quad \mathbf{v}_\perp = c\frac{\mathbf{E} \times \mathbf{B}}{B^2} \tag{4.7}$$

- interpretation of $\mathbf{j}_\parallel$ is not obvious
  - it is obtained from $\mathbf{E} \cdot \partial \mathbf{B}/\partial t + \mathbf{B} \cdot \partial \mathbf{E}/\partial t$ making use of $\mathbf{E} \cdot \mathbf{B} = 0$

4.3.3 Applications

- best developed is to pulsar magnetosphere
- possible relevance to radio jets such as those of Cygnus A

4.4 Cosmic Batteries

4.4.1 need for batteries

- dynamos can enhance pre-existing magnetic fields, but they cannot create fields where none exist

4.4.2 equations

- consider a thermal plasma consisting of protons and electrons denoted by subscripts p and e
- charge neutrality, $n_p = n_e \equiv n$, is maintained on scales much larger than the Debye length λ_{De}

$$\lambda_{De} = \frac{kT}{\left(4\pi n e^2\right)^{1/2}} \tag{4.8}$$

- for $m_e \ll m_p$, $\mathbf{v} \approx \mathbf{v}_p$, equations of motion for the protons and electrons take the form

$$\frac{d\mathbf{v}}{dt} \approx \frac{e}{m_p}\mathbf{E} + \mathbf{a}_p \tag{4.9}$$

$$\frac{d\mathbf{v}_e}{dt} \approx \nu\left(\mathbf{v} - \mathbf{v}_e\right) - \frac{e}{m_e}\mathbf{E} + \mathbf{a}_e \tag{4.10}$$

  - $\mathbf{a}$ denotes an acceleration other than that due to $\mathbf{E}$

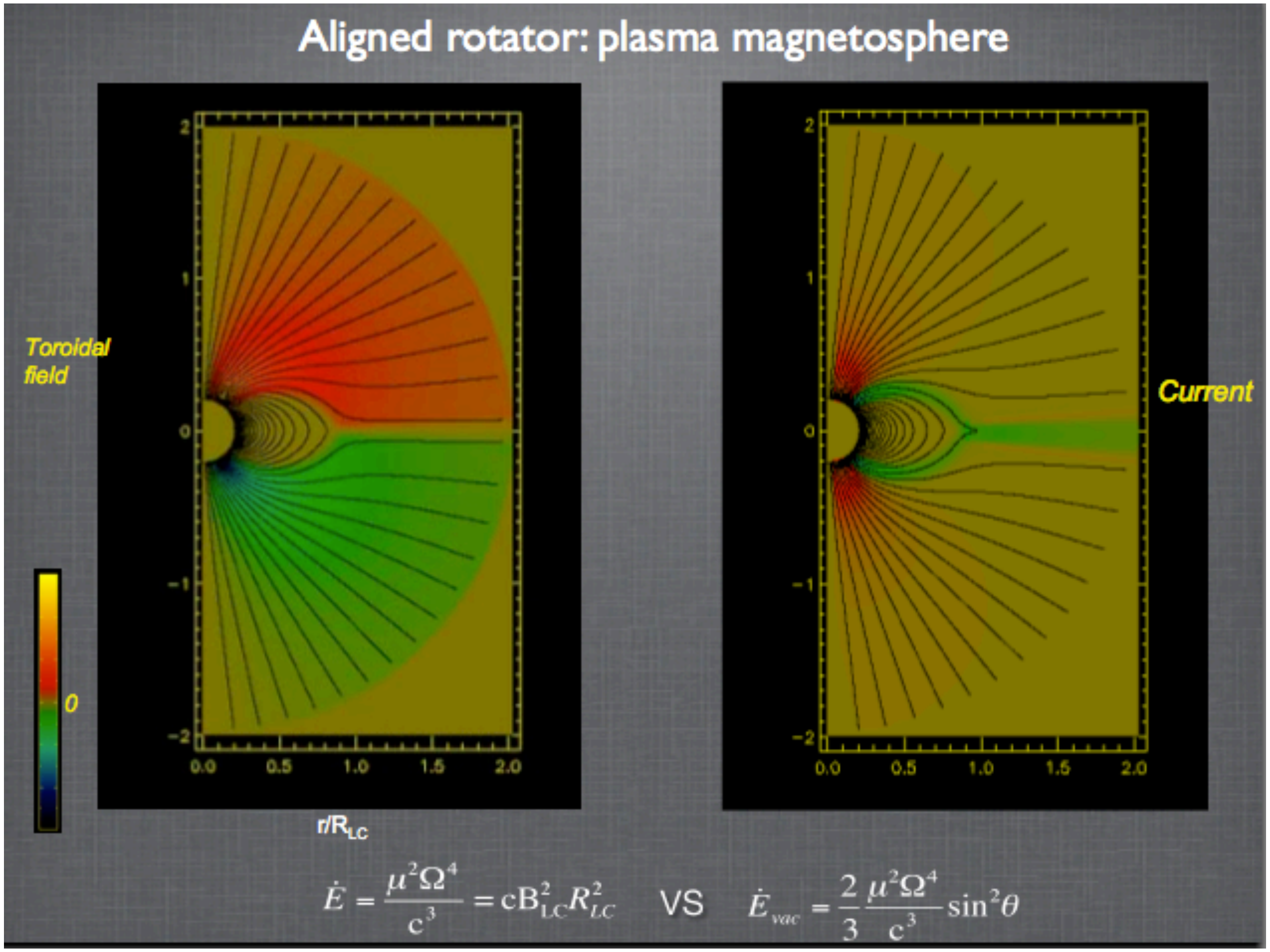

Aligned rotator: plasma magnetosphere

$$\dot{E} = \frac{\mu^2\Omega^4}{c^3} = cB_{LC}^2 R_{LC}^2 \quad \text{VS} \quad \dot{E}_{vac} = \frac{2}{3}\frac{\mu^2\Omega^4}{c^3}\sin^2\theta$$

Figure 4.9: credit: Anatoly Spitkovsky's home page

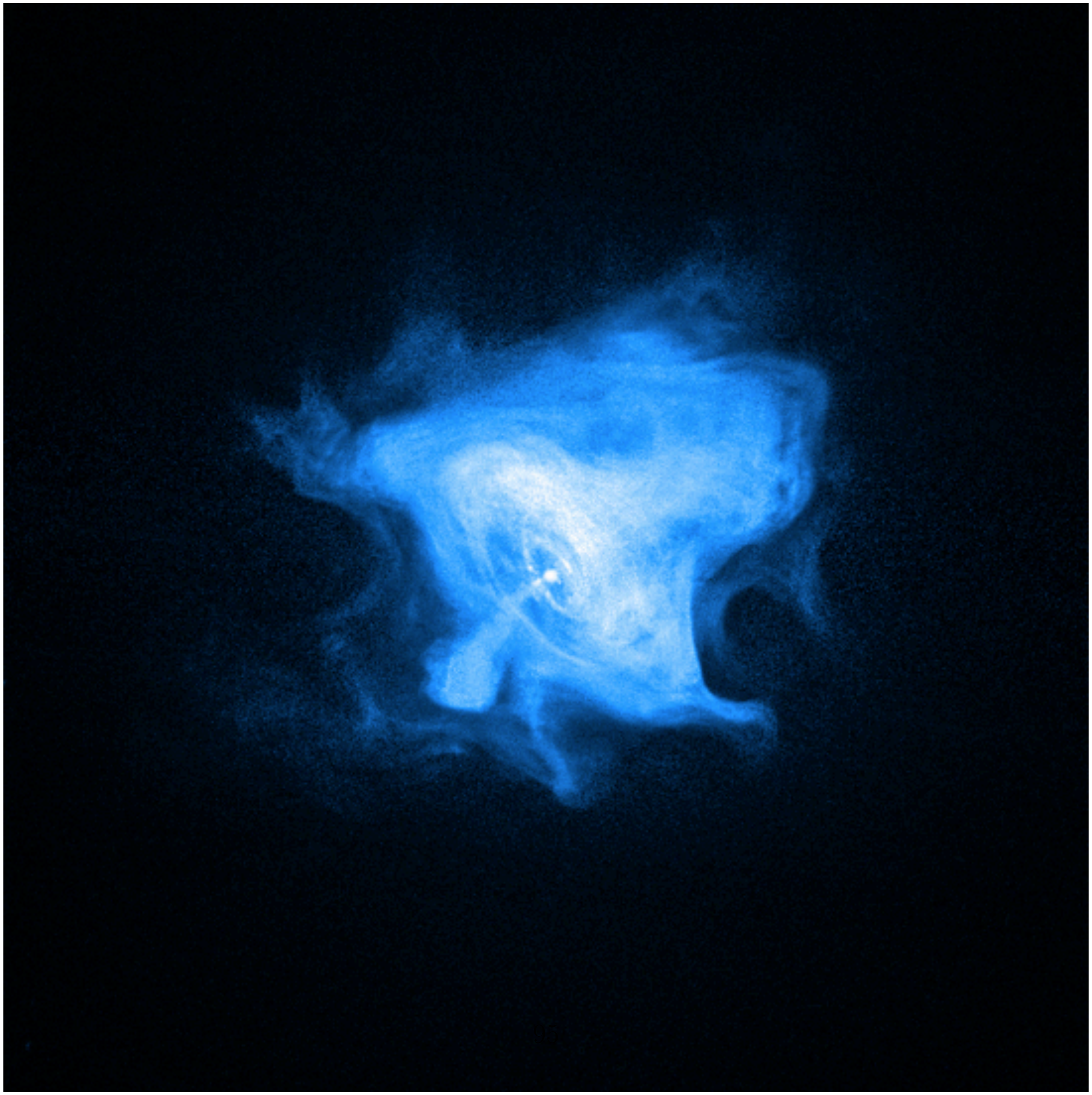

Figure 4.10: The deep x-ray image gives the first clear view of the convoluted boundaries of the Crab's pulsar wind nebula. The pulsar is the collapsed core of a massive star with more mass than the Sun and the density of an atomic nucleus. It was born in a supernova explosion that was witnessed in the year 1054. This Chandra

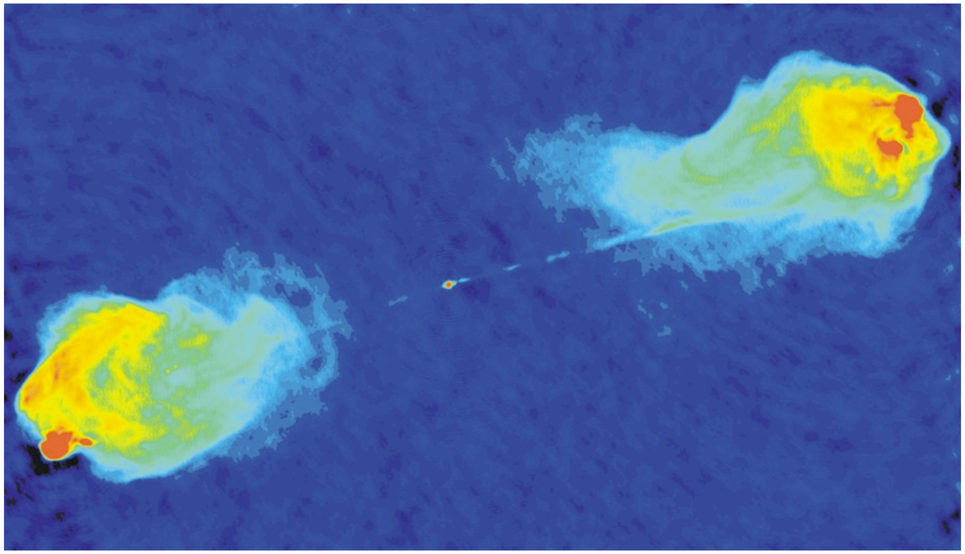

Figure 4.11: False color image of the radio jet and lobes in the hyperluminous radio galaxy Cygnus A. Red shows regions with the brightest radio emission, while blue shows regions of fainter emission. Multiconfiguration VLA observations of Cygnus A at 1.4 and 5 GHz have been used to produce detailed maps of exceptional dynamic range. A radio jet extends from the core into the northwest lobe. The broad radio lobes reveal an unexpected wealth of filamentary structure. Two new hot spots are identified. The pressure of the cluster gas in which Cyg A is embedded appears to be insufficient to confine either the jet or the filaments. From the necessarily high mechanical luminosity of the jet and the high energy densities of the hot spots, it is concluded that the jet is probably relativistic. The surface brightness of the jet is high in absolute terms, but the total radiated power of the jet is only 0.001 of that of the whole source. Investigators: R. Perley, C. Carilli & J. Dreher: Image courtesy of NRAO/AUI

  - ν is the collision frequency of electrons with protons due to thermal motions of the former

- $\mathbf{j} = en\,(\mathbf{v} - \mathbf{v}_e)$ is the current density
- combine equations (4.10) & (4.9), neglect $d\mathbf{j}/dt$ wrt $\nu\mathbf{j}$ and $m_e/m_p \ll 1$, obtain the modified Ohm's law

$$\mathbf{j} = \frac{ne^2}{m_e\nu}\mathbf{E} + \frac{ne}{\nu}(\mathbf{a}_p - \mathbf{a}_e) \tag{4.11}$$

- substitute expression for $\mathbf{E}$ in terms of $\mathbf{j}$ into induction equation and use $4\pi\mathbf{j} = c\boldsymbol{\nabla} \times \mathbf{B}$ to arrive at

$$\frac{\partial \mathbf{B}}{\partial t} = \frac{c^2}{4\pi\sigma}\nabla^2\mathbf{B} + \frac{cm_e}{e}\boldsymbol{\nabla} \times (\mathbf{a}_p - \mathbf{a}_e) \tag{4.12}$$

  - $\sigma \equiv 4\pi ne^2/(m_e\nu)$

4.4.3 Biermann Battery

- consider a thermal plasma in which $\mathbf{a} = -\boldsymbol{\nabla} p_i/\rho_i$ for $i = p \,\text{or}\, e$

$$\frac{\partial \mathbf{B}}{\partial t} = \frac{c^2}{4\pi\sigma}\nabla^2\mathbf{B} + \frac{c}{2en^2}\boldsymbol{\nabla} p \times \boldsymbol{\nabla} n \tag{4.13}$$

  - $p_p = p_e = p/2$

- analogy with circuit containing a battery maintaining voltage, V, a resister, R, and inductor, L

$$L\frac{dI}{dt} = -RI + V \tag{4.14}$$

  - $B = LI$
  - equilibrium current V/R
  - timescale to reach equilibrium L/R

- equilibrium magnetic field in plasma

$$B_{eq} \leq \frac{\sigma k T}{e c} \tag{4.15}$$

- timescale to reach equilibrium on spatial scale L

$$t_{eq} \approx \frac{4\pi\sigma L^2}{c^2} \tag{4.16}$$

Chapter 5

Odds and Ends

5.1 Growth of Structure: Newtonian Perturbation Theory

- Einstein-de Sitter model universe
  - mass dominated and marginally bound
  - scale factor $R \propto t^{2/3}$
  - $6\pi G\rho t^2 = 8\pi G\rho/(3H^2) = 1$
- evolution equation for fractional density perturbation $\delta \equiv \delta\rho/\rho$ in mass dominated universe

$$\frac{\partial^2\delta}{\partial t^2} + 2\frac{\dot{R}}{R}\frac{\partial\delta}{\partial t} - 4\pi G\rho\delta = 0 \tag{5.1}$$

  - for E-dS model equation is homogeneous in t
- solutions have form $\delta \propto t^q$ with $q = 2/3$ for growing mode and $q = -1$ for damped mode
  - contrast with Jean's instability for a uniform static medium which has exponential growth
    - Jean's swindle yields mode amplitude $\propto \exp(\sigma t)$ with $\sigma^2 = 4\pi G\rho$

5.2 Hydrodynamic Turbulence

5.2.1 Strong Turbulence

- No Long-Lived Structures, No Small Parameter, Slow Progress
  - Navier Stokes equations

$$\frac{d\mathbf{v}}{dt} \equiv \frac{\partial \mathbf{v}}{\partial t} + (\mathbf{v}\cdot\boldsymbol{\nabla})\mathbf{v} = -\frac{\boldsymbol{\nabla} p}{\rho} + \nu\nabla^2\mathbf{v} \tag{5.2}$$

    - $*$ incompressibility, $\boldsymbol{\nabla}\cdot\mathbf{v} = 0$ allows the elimination of p using $\nabla^2 p = -\rho(\boldsymbol{\nabla}\mathbf{v} : \boldsymbol{\nabla}\mathbf{v})$
  - Reynolds number

$$Re \equiv \frac{v_L L}{\nu} \tag{5.3}$$

    - $*$ ratio of inertial to viscous stresses, L is the outer scale
    - $*$ generic solutions are turbulent if $Re \gg 1$
  - vorticity equation $\boldsymbol{\omega} \equiv \boldsymbol{\nabla}\times\mathbf{v}$

$$\frac{d\boldsymbol{\omega}}{dt} \equiv \frac{\partial \boldsymbol{\omega}}{\partial t} + (\mathbf{v}\cdot\boldsymbol{\nabla})\boldsymbol{\omega} = (\boldsymbol{\omega}\cdot\boldsymbol{\nabla})\mathbf{v} + \nu\nabla^2\boldsymbol{\omega} \tag{5.4}$$

three dimensional strong turbulence

- simplest case: isotropic, homogeneous, statistically steady motion
  - energy dissipation rate per unit mass, $\epsilon \sim v_L^3/L$
- energy cascades to smaller scales $l < L$ because phase space volume is proportional to k^3
  - $k \sim 1/l$

- velocity difference across separation l satisfies $v_l^3/l \sim \epsilon$

$$v_l \sim (\epsilon l)^{1/3} \sim \left(\frac{l}{L}\right)^{1/3} v_L \tag{5.5}$$

  - critically damped eddies
  - conserved flow of energy to higher k
  - intermittency, nonuniqueness of scaling

- inner, viscous or dissipation, scale λ set by $v_\lambda \lambda \sim \nu$

$$\lambda \sim \frac{L}{Re}^{3/4} \tag{5.6}$$

- 3D Kolmogorov power spectrum of velocity fluctuations:

$$E(k) \sim \frac{\epsilon^{2/3}}{k^{11/3}} \tag{5.7}$$

  - energy per mode decreases $\propto k^{-11/3}$ in inertial range

- $E(k)$ is constant for equipartition
  - turbulent cascade is steady but far from equilibrium
  - energy sink at large $kL \sim Re^{3/4}$ prevents modes from reaching equipartition

- mixing of passive contaminants, $C_k^2 \propto k^{-11/3}$ in inertial range,

- $E(k)$ steepens and C_k^2 flattens in viscous subrange
  - applications: chemical reactions, atmospheric seeing

two dimensional strong turbulence

- each fluid column conserves its vorticity, $d\boldsymbol{\omega}/dt = (\boldsymbol{\omega} \cdot \boldsymbol{\nabla})\mathbf{v} = 0$
  - vortex lines do not stretch in 2D
- double cascade, enstrophy and energy
  - enstrophy density $|\boldsymbol{\omega}|^2$
  - energy density $|\mathbf{v}|^2/2$
- suppose fluid is stirred on scale L with $Re \sim v_L L/\nu \gg 1$
  - enstrophy cascades to smaller scales and energy cascades to larger scales
- enstrophy cascade: enstrophy dissipation rate per unit mass $\phi \sim v_L^3/L^3$ implies

$$v_l \sim \frac{v_L}{L} l \quad \text{for}\, l < L \tag{5.8}$$

- inner, viscous or dissipation, scale $\lambda \sim L/Re^{1/2}$
- energy per mode in inertial range of direct enstrophy cascade

$$E(k) \sim \frac{\epsilon^{2/3}}{L^{4/3} k^4} \tag{5.9}$$

  - enstrophy cascade has come under scrutiny in recent times
- energy cascade: similar to 3D case but inverse and 2D
  - 2D Kolmogorov, similar to 3D case but inverse cascade

$$v_l \sim (\epsilon l)^{1/3} \sim \left(\frac{l}{L}\right)^{1/3} v_L \quad \text{for}\, l > L \tag{5.10}$$

- energy per mode in inertial range of inverse energy cascade, $k < 1/L$

$$E(k) \sim \frac{\epsilon^{2/3}}{k^{8/3}} \tag{5.11}$$

  - applications: large scale motions in planetary atmospheres and oceans

5.2.2 Weak Turbulence

- Interacting Waves Which Live For Many Periods, Successful Perturbation Theory
  - examples drawn from surface waves on deep water
    - velocity field decays with depth on scale k^{-1}
    - small parameter is surface slope
  - dispersion relation

$$\omega^2 = \frac{\gamma}{\rho} k^3 + gk \tag{5.12}$$

capillary waves

- decay dispersion relation, $\omega^2 = \alpha k^3$, $\alpha \equiv \gamma/\rho$
- lowest order nonlinearities couple 3-modes
- resonance relations for interacting triplets: $\mathbf{k}_1 = \mathbf{k}_2 + \mathbf{k}_3, \quad \omega_1 = \omega_2 + \omega_3$
  - analogous to quantum mechanical conservations laws for momentum and energy
  - 3-mode interactions involve the creation and destruction of quasi-particles
  - nonlinear interaction rate from $(\mathbf{v} \cdot \boldsymbol{\nabla})\mathbf{v}$

- consider collisions of wave packets

$$\frac{1}{\omega_l t_l} \sim \left(\frac{v_l}{v_{ph}}\right)^2 \tag{5.13}$$

  - scaling for t_l assumes local interactions in k space

- energy undergoes a direct cascade
- dissipation rate per unit mass per unit surface area

$$\epsilon \sim \frac{v_l^2 l}{t_l} \sim \frac{v_l^4 l^{1/2}}{\alpha^{1/2}} \tag{5.14}$$

- scaling of v_l for $l < L$

$$v_l \sim \frac{\alpha^{1/8}\epsilon^{1/4}}{l^{1/8}} \sim \left(\frac{L}{l}\right)^{1/8} v_L \tag{5.15}$$

- nonlinearity decreases along cascade
  - $(\omega_l t_l)^{-1} \propto l^{3/4}$
  - slope of surface $\delta_l \sim v_l/\omega_l l \propto l^{3/8}$,
- energy per mode $k^2 E(k) \sim v_l^2 l$ for $k \sim 1/l$

$$E(k) \sim \frac{\alpha^{1/4}\epsilon^{1/2}}{k^{11/4}} \tag{5.16}$$

gravity waves

- non-decay dispersion relation, $\omega^2 = gk$
  - no resonant 3-mode couplings

  - if $\mathbf{k}_1 = \mathbf{k}_2 + \mathbf{k}_3$ then $\omega_1 \le (\omega_2^2 + \omega_3^2)^{1/2}$

- lowest order nonlinear interations couple 4-modes
- resonance relations for 4-mode interactions, $\mathbf{k}_1 + \mathbf{k}_2 = \mathbf{k}_3 + \mathbf{k}_4, \quad \omega_1 + \omega_2 = \omega_3 + \omega_4$
  - 4-mode interactions describe the elastic scattering of quasi-particles
  - interactions conserve quasi-particle number
  - double cascade, energy and quasi-particle number
- consider waves generated on energy input scale L
  - energy cascades to small scales and quasi-particles cascade to large scales
  - nonlinear interaction rate from $(\mathbf{v} \cdot \boldsymbol{\nabla})\mathbf{v}$ yields

$$\frac{1}{\omega_l t_l} \sim \left(\frac{v_l}{v_{ph}}\right)^4 \tag{5.17}$$

- direct energy cascade
  - scaling of v_l for $l < L$ based on energy dissipation rate per unit mass per unit surface area

$$\epsilon \sim \frac{v_l^2 l}{t_l} \sim \frac{v_l^6}{g^{3/2} l^{3/2}} \tag{5.18}$$

  - yields

$$v_l \sim g^{1/4} \epsilon^{1/6} l^{1/4} \sim \left(\frac{l}{L}\right)^{1/4} v_L \tag{5.19}$$

- nonlinearity increases along cascade
  - $(\omega_l t_l)^{-1} \propto l^{-1}$.

  - slope of surface $\delta_l \sim v_l/\omega_l l \propto l^{-1/4}$
  - energy cascade terminates by wave breaking

- energy per mode for direct energy cascade, $k > 1/L$

$$E(k) \sim \frac{g^{1/2}\epsilon^{1/3}}{k^{7/2}} \tag{5.20}$$

- inverse cascade of quasi-particles
  - scaling of v_l for $l > L$ based on the quasi-particle production rate per unit area, $q \sim \epsilon(L/g)^{1/2}$

$$q \sim \frac{v_l^2 l}{\omega_l t_l} \sim \frac{v_l^6}{g^2 l} \tag{5.21}$$

yields

$$v_l \sim g^{1/3} q^{1/6} l^{1/6} \sim \left(\frac{l}{L}\right)^{1/6} v_L \tag{5.22}$$

- nonlinearity decreases along the cascade
  - $(\omega_l t_l)^{-1} \propto l^{-4/3}$
  - slope of surface $\delta_l \propto l^{-1/3}$

- energy per mode for inverse quasi-particle cascade, $k < 1/L$

$$E(k) \sim \frac{g^{1/2} L^{1/6} \epsilon^{1/3}}{k^{10/3}} \tag{5.23}$$

- applications: aging of gravity wave spectrum, wind surfing in the Columbia river gorge

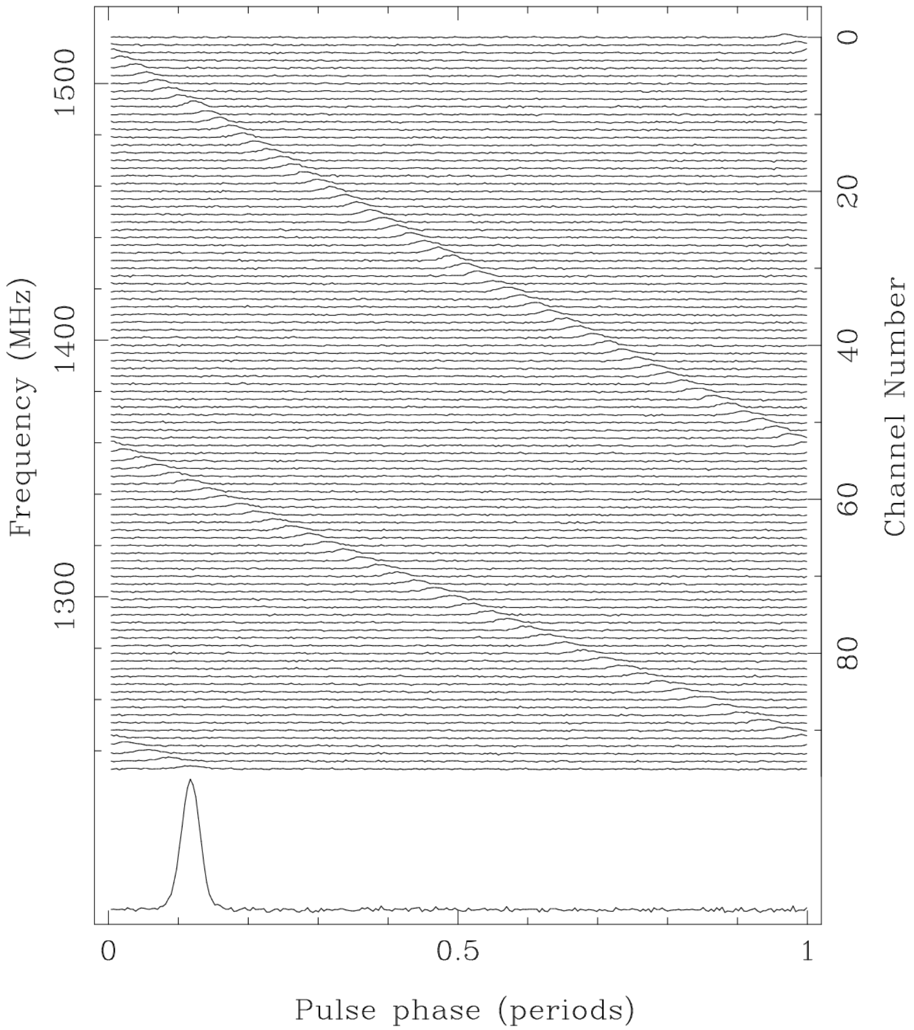

Figure 5.1: Pulsar dispersion. Uncorrected dispersive delays for a pulsar observation over a bandwidth of 288 MHz centered at 1380 MHz. The delays wrap since the data are folded (i.e. averaged) modulo the pulse period. (From the Handbook of Pulsar Astronomy, by Lorimer and Kramer)

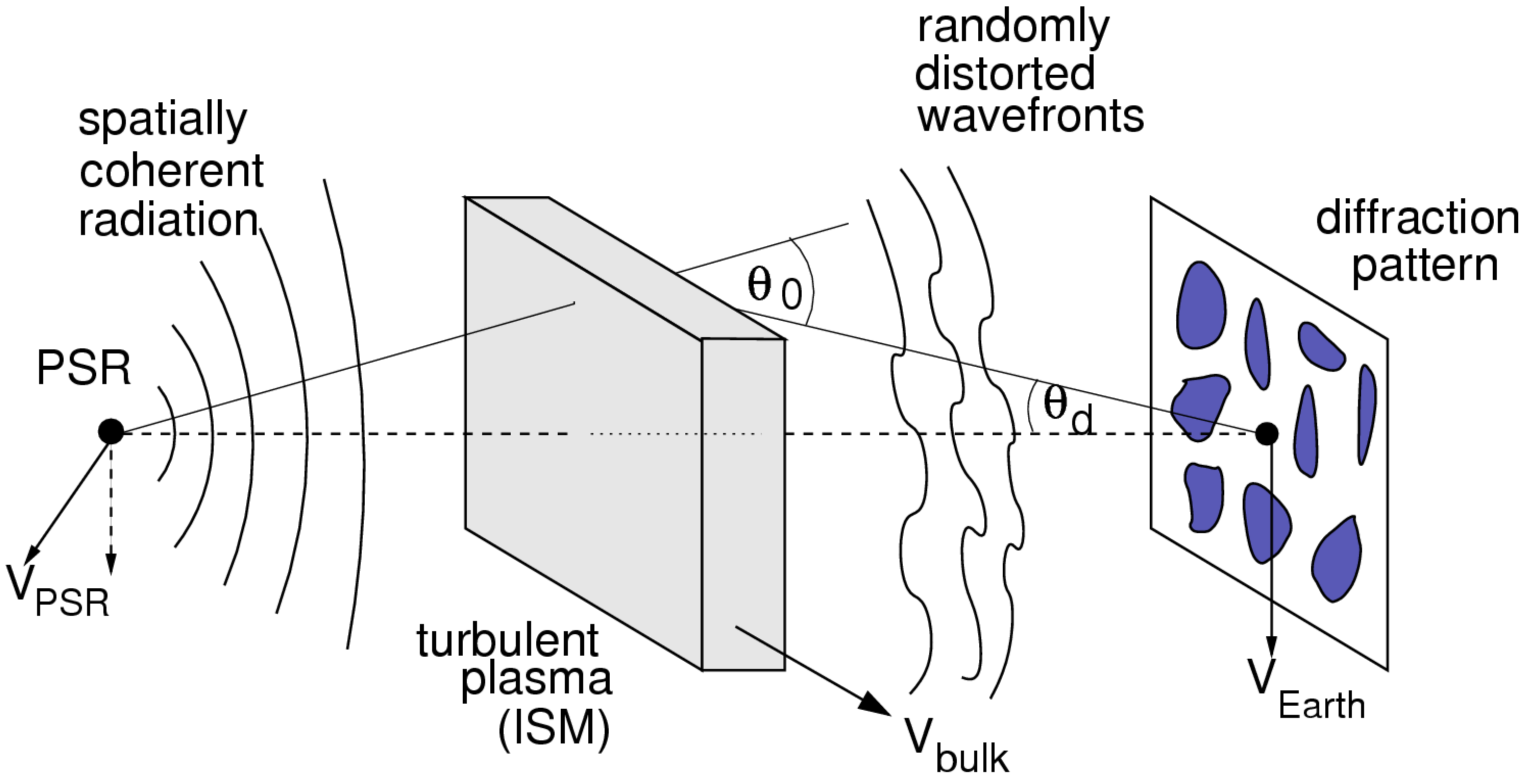

Figure 5.2: Thin Screen Diffraction/Scattering model. Inhomogeneities in the ISM cause small-angle deviations in the paths of the radio waves. These deviations result in time (and therefore phase) delays that interfere to create a diffraction pattern, broaden the pulses in time, and make a larger image of the pulsar on the sky. (From the Handbook of Pulsar Astronomy, by Lorimer and Kramer)

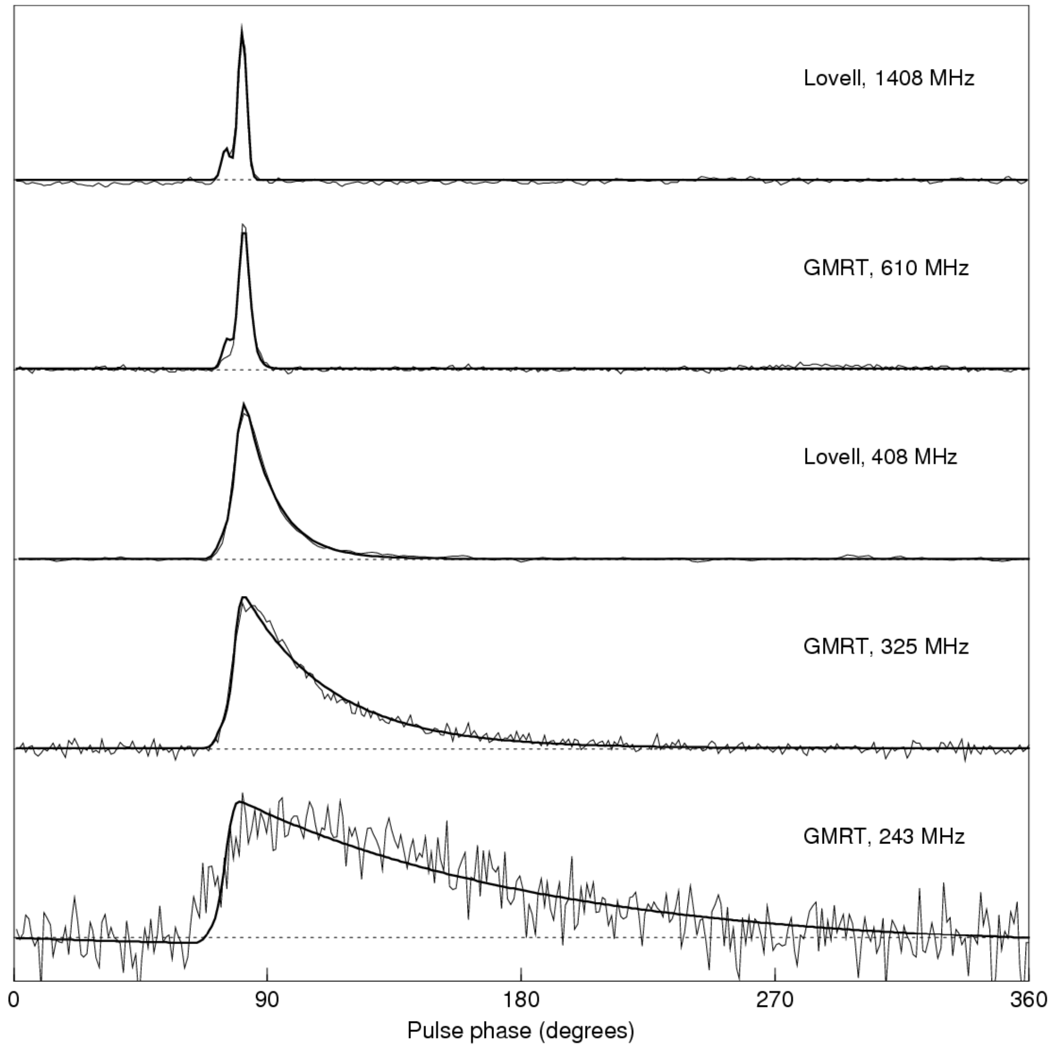

Figure 5.3: Pulse broadening caused by scattering. Scattering of the pulsed signal by ISM inhomogeneities results in delays that cause a scattering tail. (From the Handbook of Pulsar Astronomy, by Lorimer and Kramer)

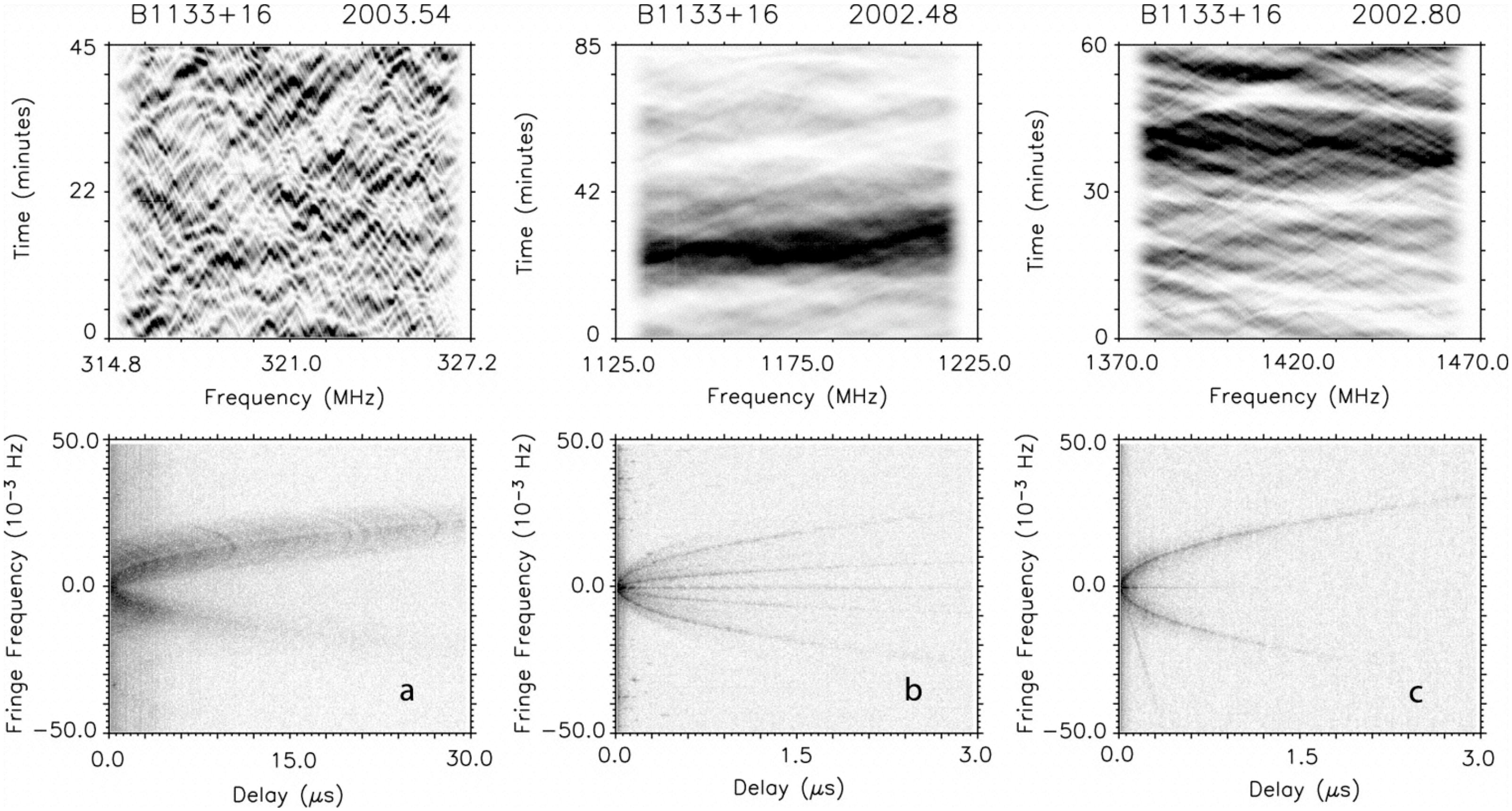

Figure 5.4: PSR B1133+16, shows multiple scintillation arcs on occasion. The broad, asymmetric power distribution in (a) has numerous arclets at 321 MHz. Panels (b) and (c) are at frequencies above 1 GHz. Panel (b) shows two clear arcs (along with a horizontal line at f_t due to narrowband radio frequency interference and the sidelobe response of power near the origin). Four months later (panel [c]), only the outer of these two arcs, widened by the $a \propto \nu^{-2}$ scaling, is visible. From Cordes et al. in the Astrophysical Journal, 637:346-365, 2006

5.3 Magnetohydrodynamical Turbulence

5.3.1 motivation from radio observations of pulsars

5.3.2 HD Turbulence

- review of Kolmogorov scalings

$$Re \sim \frac{v_L L}{\nu} \gg 1. \tag{5.24}$$

$$\frac{\partial v}{\partial t} = -(v \cdot \nabla) v - \nabla P + \nu \nabla^2 v. \tag{5.25}$$

$$\epsilon \sim \frac{v_\lambda^3}{\lambda}. \tag{5.26}$$

$$v_\lambda \sim (\epsilon \lambda)^{1/3}. \tag{5.27}$$

$$v_k^2 \sim \frac{\epsilon^{2/3}}{k^{11/3}}. \tag{5.28}$$

$$\ell_{\mathrm{vis}} \sim \frac{L}{Re^{3/4}}. \tag{5.29}$$

5.3.3 MHD Equations

$$\frac{\partial \mathbf{v}}{\partial t} + (\mathbf{V}_\mathrm{A} \cdot \boldsymbol{\nabla})\mathbf{v} = -(\mathbf{v} \cdot \boldsymbol{\nabla})\mathbf{v} + (\mathbf{b} \cdot \boldsymbol{\nabla})\mathbf{b} - \boldsymbol{\nabla} P + \nu \nabla^2 \mathbf{v}. \tag{5.30}$$

$$\frac{\partial \mathbf{b}}{\partial t} + (\mathbf{V}_\mathrm{A} \cdot \boldsymbol{\nabla})\mathbf{b} = -(\mathbf{v} \cdot \boldsymbol{\nabla})\mathbf{b} + (\mathbf{b} \cdot \boldsymbol{\nabla})\mathbf{v} - \boldsymbol{\nabla} P + \kappa \nabla^2 \mathbf{b}. \tag{5.31}$$

$$\mathbf{V}_\mathrm{A} \equiv \frac{\mathbf{B}_0}{(4\pi\rho)^{1/2}} \quad \text{and} \quad \mathbf{b} = \frac{\mathbf{B}}{(4\pi\rho)^{1/2}} - \mathbf{V}_\mathrm{A}. \tag{5.32}$$

$$\boldsymbol{\nabla} \cdot \mathbf{v} = 0 \quad \text{and} \quad \boldsymbol{\nabla} \cdot \mathbf{b} = 0. \tag{5.33}$$

Elsasser variables

$$\mathbf{u} = \mathbf{v} + \mathbf{b} \quad \text{and} \quad \mathbf{w} = \mathbf{v} - \mathbf{b}. \tag{5.34}$$

$$\boldsymbol{\nabla} \cdot \mathbf{u} = 0 \quad \text{and} \quad \boldsymbol{\nabla} \cdot \mathbf{w} = 0. \tag{5.35}$$

$$P = -\nabla^{-2}(\boldsymbol{\nabla}\mathbf{u} : \boldsymbol{\nabla}\mathbf{w}). \tag{5.36}$$

- drop diffusive terms: $\nu = 0$, $\kappa = 0$

$$\frac{\partial \mathbf{u}}{\partial t} - V_\mathrm{A} \frac{\partial \mathbf{u}}{\partial z} = -(\mathbf{w} \cdot \boldsymbol{\nabla})\mathbf{u} - \boldsymbol{\nabla} P, \tag{5.37}$$

$$\frac{\partial \mathbf{w}}{\partial t} + V_\mathrm{A} \frac{\partial \mathbf{w}}{\partial z} = -(\mathbf{u} \cdot \boldsymbol{\nabla})\mathbf{w} - \boldsymbol{\nabla} P, \tag{5.38}$$

5.3.4 Wave Packets

- arbitrary wave packets are exact solutions so only oppositely directed wave packets interact
  - $w = 0$ implies $P = 0$ so u is transported at $V_{\rm A}$
  - $u = 0$ implies $P = 0$ so w is transported at $-V_{\rm A}$
- individual wave packets conserve energy in collisions
  - conservation of energy:

$$E = \frac{1}{2}\int d^3x \left(v^2 + b^2\right) = \frac{1}{4}\int d^3x \left(u^2 + w^2\right) \tag{5.39}$$

  - conservation of cross helicity:

$$H = \frac{1}{2}\int d^3x \,(\mathbf{v}\cdot\mathbf{b}) = \frac{1}{8}\int d^3x \left(u^2 - w^2\right). \tag{5.40}$$

- two linear wave modes: shear Alfven (sA) and pseudo Alfven (pA)
  - common dispersion relation: $\omega^2 = k_z^2 V_{\rm A}^2$
  - common group velocity: $\mathbf{v}_{gp} = \pm V_{\rm A}\hat{\mathbf{z}}$
  - polarizations

$$\hat{\mathbf{e}}_{\rm sA} = \frac{\hat{\mathbf{k}}\times\hat{\mathbf{z}}}{|\hat{\mathbf{k}}\times\hat{\mathbf{z}}|} \qquad \hat{\mathbf{e}}_{\rm pA} = \frac{\hat{\mathbf{z}} - (\hat{\mathbf{k}}\cdot\hat{\mathbf{z}})\hat{\mathbf{k}})}{[1-(\hat{\mathbf{k}}\cdot\hat{\mathbf{z}})^2]^{1/2}}. \tag{5.41}$$

- wave packets follow field lines to lowest nonlinear order
  - linear waves have $\mathbf{u} = 2\mathbf{b}$ and $\mathbf{w} = -2\mathbf{b}$

5.3.5 Weak MHD Turbulence

- nonlinear interactions among waves in the limit that individual waves live many periods

Iroshnikov-Kraichnan Model

- critical assumption of isotropy
- scalings

$$\frac{\delta v_\lambda}{v_\lambda} \sim \frac{v_\lambda}{V_\mathrm{A}} \tag{5.42}$$

$$N_\lambda \sim \left(\frac{V_\mathrm{A}}{v_\lambda}\right)^2 \tag{5.43}$$

$$\epsilon \sim \frac{V_\mathrm{A}}{\lambda}\frac{v_\lambda^2}{N_\lambda} \sim \frac{v_\lambda^4}{V_\mathrm{A}\lambda} \tag{5.44}$$

$$v_\lambda \sim (\epsilon V_\mathrm{A}\lambda)^{1/4} \tag{5.45}$$

- 3D power spectrum

$$v_k^2 \sim \left(\frac{\epsilon V_\mathrm{A}}{k^7}\right)^{1/2} \tag{5.46}$$

- cascade weakens toward smaller λ

$$N_\lambda \sim \left(\frac{V_\mathrm{A}^3}{\epsilon\lambda}\right)^{1/2} \tag{5.47}$$

Three Wave Cascade

- resonance relations

$$\mathbf{k}_1 + \mathbf{k}_2 = \mathbf{k}_3 \quad \text{and} \quad \omega_1 + \omega_2 = \omega_3 \tag{5.48}$$

- consequence of resonance relations
    - $\mathbf{k}_1 \cdot \hat{\mathbf{z}} + \mathbf{k}_2 \cdot \hat{\mathbf{z}} = \mathbf{k}_3 \cdot \hat{\mathbf{z}} \quad \text{and} \quad |\mathbf{k}_1 \cdot \hat{\mathbf{z}}| + |\mathbf{k}_2 \cdot \hat{\mathbf{z}}| = |\mathbf{k}_3 \cdot \hat{\mathbf{z}} \quad \text{imply} \quad \mathbf{k}_2 \cdot \hat{\mathbf{z}} = 0$

- scalings

$$\frac{\delta v_{\lambda_\perp}}{v_{\lambda_\perp}} \sim \frac{v_{\lambda_\perp}}{V_\mathrm{A}} \frac{\lambda_\|}{\lambda_\perp}. \tag{5.49}$$

$$N_{\lambda_\perp} \sim \left(\frac{V_\mathrm{A}\lambda_\perp}{v_{\lambda_\perp}\lambda_\|}\right)^2. \tag{5.50}$$

$$\epsilon \sim \frac{V_\mathrm{A}}{\lambda_\|} \frac{v_{\lambda_\perp}^2}{N_{\lambda_\perp}} \sim \frac{v_{\lambda_\perp}^4 \lambda_\|}{V_\mathrm{A}\lambda_\perp^2}. \tag{5.51}$$

$$v_{\lambda_\perp}^2 \sim \left(\frac{\epsilon V_\mathrm{A}}{\lambda_\|}\right)^{1/2} \lambda_\perp. \tag{5.52}$$

- 3D power spectrum

$$v_{k_\perp}^2 \sim \frac{\left(\epsilon V_\mathrm{A} k_\|\right)^{1/2}}{k_\perp^3}. \tag{5.53}$$

- cascade strengthens toward smaller $\lambda_\perp$

$$N_\lambda \sim \left(\frac{V_\mathrm{A}^3}{\epsilon\lambda_\|^3}\right)^{1/2} \lambda_\perp. \tag{5.54}$$

- imbalanced cascades

5.3.6 Strong MHD Turbulence

- critical balance

$$N_{\lambda_\perp} \sim \frac{V_\mathrm{A}\lambda_\perp}{v_{\lambda_\perp}\lambda_\parallel} \sim 1. \tag{5.55}$$

  - physical motivation: frequency broadening and causality

- cascade scalings

$$\epsilon \sim \frac{V_\mathrm{A}}{\lambda_\parallel} v_{\lambda_\perp}^2 \sim v_{\lambda_\perp}^3 \lambda_\perp. \tag{5.56}$$

  - perpendicular cascade

$$v_{\lambda_\perp} \sim \left(\epsilon\lambda_{\lambda_\perp}\right)^{1/3}. \tag{5.57}$$

  - parallel cascade

$$\lambda_\parallel \sim \frac{V_\mathrm{A}\lambda_\perp^{2/3}}{\epsilon^{1/3}}. \tag{5.58}$$

- 3D power spectrum

$$v_\mathbf{k}^2 \sim \frac{\epsilon L^{2/3}}{k_\perp^{10/3}} f\left(\frac{k_\parallel L^{1/3}}{k_\perp^{2/3}}\right) \tag{5.59}$$

- intermittency

5.3.7 Common Features of Cascades

- dominant role of shear Alfven waves
- passive role of pseudo Alfven waves

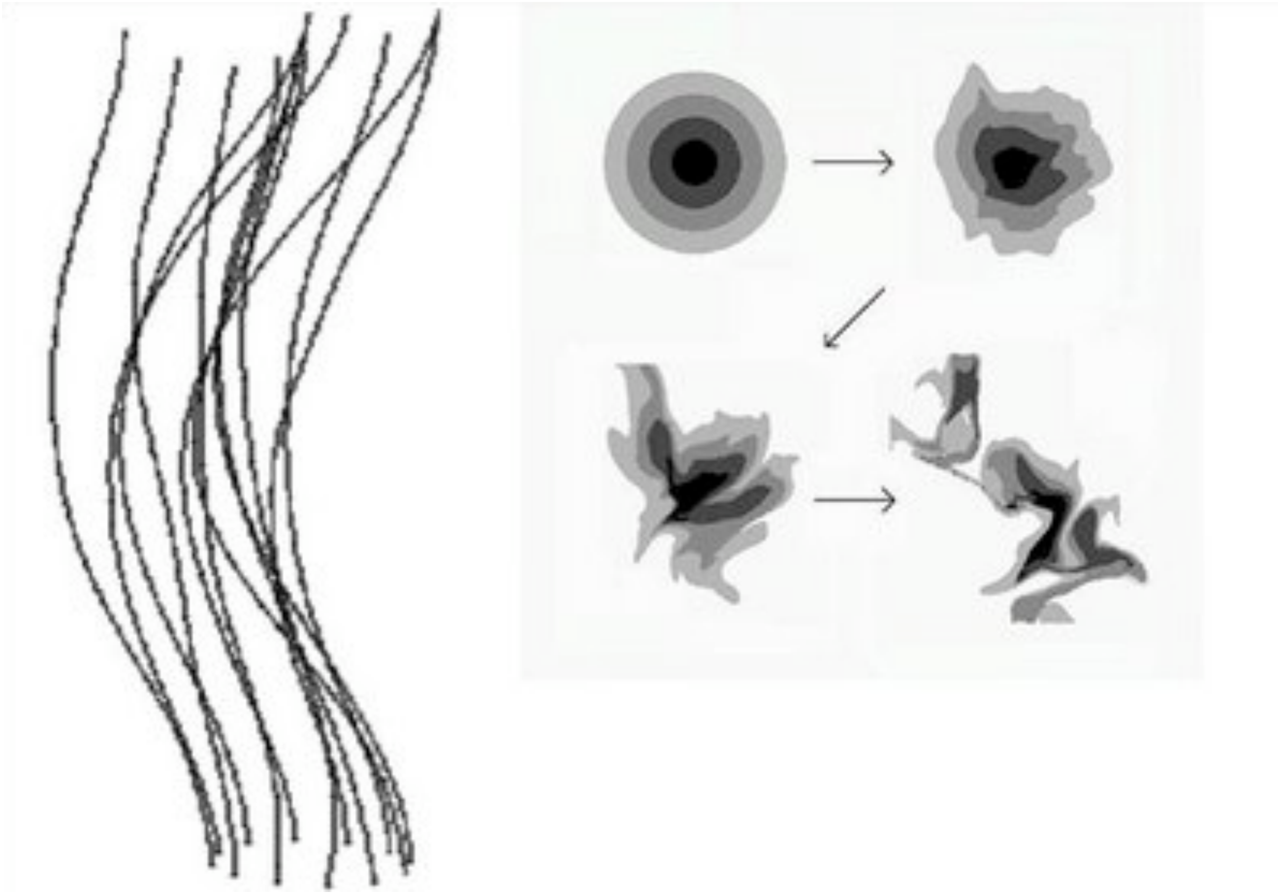

Figure 5.5: Wave packet distortion through field-line wander. Left: Sample of field lines perturbed by downward-propagating waves. Right: Distortion of an originally circular bulls-eye pattern as it moves upward following these field lines. Maron & Goldreich (2001)

.

5.3.8 Imbalanced Cascades

weak turbulence

- scalings
  - energy dissipation
$$\epsilon^{\pm} \sim \frac{\left(v_{\lambda_\perp,+} v_{\lambda_\perp,-}\right)^2}{V_{\mathrm{A}} \lambda_\parallel}. \tag{5.60}$$
  - steady-state spectra pin at dissipation scale

strong turbulence

- scalings
$$\epsilon^{\pm} \sim \frac{v_{\lambda_\perp,\mp} v^2_{\lambda_\perp,\pm}}{\lambda_\parallel} \tag{5.61}$$
- second principal remains controversial

5.4 Interaction of Sound Waves with Turbulence

5.4.1 Setup

- consider a box of volume V filled with fluid a fraction of which is turbulent
- assume that the turbulence is homogeneous and isotropic in a patch that does not touch the walls
  - picture the turbulence as composed of energy bearing eddies of linear size H and velocity v
  - eddies are critically damped, their lifetimes are of order H/v
    - turbulence dissipates

  - eddies couple most strongly to acoustic modes with frequencies $\omega \sim v/H$
  - fractional density fluctuations associated with the turbulence are $\Delta\rho/\rho \sim M^2$
    - $M = v/c$ is the Mach number

5.4.2 Emissivity

- acoustic emissivity, ϵ, is the emission rate per unit volume of acoustic energy
- ϵ can be written as the rate of dissipation of turbulent energy per unit volume times the acoustic efficiency, η

$$\epsilon = \frac{\rho v^3}{H}\eta \tag{5.62}$$

- $\eta = M^5$ for free turbulence in which quadrupoles are the lowest order acoustic multipoles
  - $\eta = M$ for processes that create and destroy fluid volume: whistles, loudspeakers
  - $\eta = M^3$ for processes that add and remove fluid momentum

5.4.3 Absorptivity

- acoustic absorptivity, α, relates the rate of absorption of acoustic energy to the acoustic energy density
- α for free turbulence can be thought of as arising from turbulent kinetic viscosity, $\nu \sim vH$

$$\alpha \sim \nu \left(\frac{\omega}{c}\right)^2 \sim \frac{v}{H}M^2 \tag{5.63}$$

5.4.4 Energy of Acoustic Modes

- equilibrium acoustic energy density in the box

$$\frac{E}{V} \sim \frac{\epsilon}{\alpha} \sim \rho v^2 M^3 \tag{5.64}$$

  - independent of the fraction of the fluid in the box that is turbulent
  - lower than the turbulent kinetic energy density by a factor M^2

- number of acoustic modes of frequency $\omega \sim v/H$ that fit in box is of order $M^3 V/H^3$

- energy per mode

$$\mathcal{E} = \rho H^3 v^2 \tag{5.65}$$

  - mode energies equilibrate with that of the eddies

5.4.5 Time to Achieve Equilibrium

- equilibration time depends inversely on the fraction of the fluid that is turbulent

$$t_{eq} \sim \frac{1}{f\alpha} \sim \frac{1}{fM^2}\frac{H}{v} \tag{5.66}$$

references

- Babcock, H. W., (1961): THE TOPOLOGY OF THE SUN'S MAGNETIC FIELD AND THE 22-YEAR CYCLE, Astrophysical Journal, 133, 572-578

- Balbus, S. A., Hawley, J. F. (1998): Instability, turbulence, and enhanced transport in accretion disks, Rev. Mod. Phys. 70, 1-53

- Cordes et al, (2006): THEORY OF PARABOLIC ARCS IN INTERSTELLAR SCINTILLATION SPECTRA, Astrophysical Journal, 637, 346-365

- Lopes, I. P., (2001): Nonradial adiabatic oscillations of stars. Mode classification of acoustic-gravity waves, Astronomy and Astrophysics, 373, 916-931g

- Lorimer, D. R., Kramer, M., (2005): Handbook of pulsar astronomy, Cambridge University Press, 277 pp.

- Maron, J., Goldreich, P., (2001): SIMULATIONS OF INCOMPRESSIBLE MAGNETOHYDRODYNAMIC TURBULENCE, THE ASTROPHYSICAL JOURNAL, 554, 1175-1196

- Roberts, H.P., (2007): Theory of the geodynamo In Treatise on Geophysics, Geomagnetism, Ed. P. Olson, 8, 67-102

- Shu, F. H., (1992) :The physics of astrophysics. Volume II: Gas dynamics, University Science Books, Mill Valley, CA (USA), 493 pp.

- Astronomy Picture of the Day,
  http://antwrp.gsfc.nasa.gov/apod/ap091025 .html

- European Southern Observatory,
  http://www.eso.org/gallery/v/ESOPIA/ illustrations/phot-23a-01-hires.jpg.html

- esa,
  http://www.esa.int/esaSC/SEM962V4QWD_index_1.html
- Further physics - Associating with swing (Source: Prof. Lai Hon-ming. Translation by Sammy Tsui),
  http://www.phy.cuhk.edu.hk/phyworld/ articles/swing/swing_e.html
- Hubble Heritage Gallery of Images,
  http://heritage.stsci.edu/gallery/ galindex.html
- HubbleSite,
  http://hubblesite.org/gallery/album/solar_system/pr2000038a/
- Images from the Solar Oscillations Investigation - Michelson Doppler Imager,
  http://soi.stanford.edu/technotes/figures/96mar_dop_sing_m_avg.sm.gif
- Kavli Institutre for Theoretical Physics,
  http://online.itp.ucsb.edu/ jet+disk _c05/spitkovsky/oh/14.html
- NASA,
  http://www.nasa.gov/
- NASA Marshall Space Flight Center,
  http://solarscience.msfc.nasa.gov/
- NASA/JPL,
  http://www.jpl.nasa.gov/wallpaper/stargal.cfm
- National Radio Astronomy Observatory,
  http://images.nrao.edu/AGN/ Radio_Galaxies/260

- Obserwatorium Astronomiczne Uniwersytetu Jagiellonskiego,
  http://www.oa. uj.edu.pl/ apod/apod/ap050504.html
- Richard W. Pogge Professor of Astronomy,
  http://www.astronomy.ohio-state.edu/ pogge/ Ast162/Unit3/extreme.html
- SOLAR AND HELIOSPHERIC OBSERVATORY,
  http://sohowww.nascom. nasa.gov/ gallery/Helioseismology/mdi005.html
- Solar and Magnetospheric MHD Theory Group,
  http://www-solar.mcs.st-and.ac.uk/ alan/ sun_course/Chapter6/node3.html
- The McDonald Network,
  http://www.themcdonalds.net/richard/astro/papers/ 602-tides-web.pdf
- Windows to the Universe,
  http://www.windows.ucar.edu/tour/link=/physical_ science/ magnetism
  /planetary_magnetospheres.html&edu=mid&back=/search/ search_navigation.html
- Wikipedia,
  http://en.wikipedia.org/wiki/Hertzsprung%E2%80%93Russell_ diagram,
  http://upload.wikimedia.org/wikipedia/commons/b/ba/Comet_Hale-Bopp_1995O1.jpg,
  http://ja.wikipedia.org/wiki/%E3%83%95%E3%82%A1%E3% 82%A4%E3%83%AB:Mercury